Universidad de Cádiz

Escuela Superior de Ingeniería

TRABAJO DE FIN DE GRADO

GRADO EN INGENIERÍA AEROESPACIAL

ANALYSIS OF ADAPTIVE MESH REFINEMENT CAPABILITY FOR THE PREDICTION OF SHOCK WAVE/BOUNDARY LAYER INTERACTIONS

AUTOR: SERGIO LINARES MÁRQUEZ

Cádiz, junio 2021

Universidad de Cádiz

Escuela Superior de Ingeniería

TRABAJO DE FIN DE GRADO

GRADO EN INGENIERÍA AEROESPACIAL

ANALYSIS OF ADAPTIVE MESH REFINEMENT CAPABILITY FOR THE PREDICTION OF SHOCK WAVE/BOUNDARY LAYER INTERACTIONS

DIRECTOR: JUAN ÁNGEL TENDERO VENTANAS
AUTOR: SERGIO LINARES MÁRQUEZ

Cádiz, junio 2021

De Cádiz para Cádiz

Yo no sé lo que es el destino,
caminando fui lo que fui.
Allá Dios que será divino,
yo me muero como viví.

A mis padres, por ser la razón de todos mis logros

Abstract

In this bachelor's thesis, the flow over a nominally two-dimensional 20° compression corner at M= 2.85 has been simulated in order to evaluate the capabilities of adaptive mesh refinement methods in flows involving shock wave/turbulent boundary layer interactions. Hence, Reynolds Averaged Navier-Stokes (RANS) simulations have been carried out using Ansys Fluent to pursue the former objective.

The initial grid convergence study using $k-\omega$ SST turbulence model showed that the optimal cell count for a structured mesh in the simulated conditions was $9.0 \cdot 10^4$. In addition, a turbulence model assessment was performed comparing Spalart-Allmaras model with different $k-\varepsilon$ and $k-\omega$ turbulence models. For the studied flow, Georgiadis and Yoder version of the $k-\omega$ SST model was the one which showed better agreement with the experimental values.

Finally, different adaptive mesh refinement configurations were tested, regarding pressure and velocity gradients. Thus, results comparable to the fine grid solution were obtained, with a reduction of more than an 80% in the overall computational cost.

Table of contents

List of Figures

List of Tables

List of Symbols

A_0	Model coefficient 1 (realizable $k-\varepsilon$)
A_s	Model coefficient 2 (realizable $k-\varepsilon$)
AMG	Algebraic multigrid
AMR	Adaptive mesh refinement
a_1	Model coefficient 1 ($k-\omega$ SST)
B	Empirical coefficient (dimensionless mean velocity profile)
C_1	Constant (Sutherland's law)
$C_{1\varepsilon}$	Model coefficient 1 ($k-\varepsilon$)
$C_{1\varepsilon*}$	Model coefficient 3 (realizable $k-\varepsilon$)
$C_{2\varepsilon}$	Model coefficient 2 ($k-\varepsilon$)
$C_{2\varepsilon*}$	Model coefficient 4 (realizable $k-\varepsilon$)
C_μ	Model coefficient 3 ($k-\varepsilon$)
CFD	Computational fluid dynamics
CPU	Central processing unit
c_{b1}	Model coefficient 1 (Spalart-Allmaras)
c_{b2}	Model coefficient 2 (Spalart-Allmaras)
c_f	Skin friction coefficient
c_p	Specific heat at constant pressure
c_{v1}	Model coefficient 3 (Spalart-Allmaras)
c_{w1}	Model coefficient 4 (Spalart-Allmaras)
D_h	Hydraulic diameter
DES	Detached Eddy Simulation
DNS	Direct numerical simulation
d	Distance from a field point to the nearest wall
e_1	User parameter used to evaluate the numerical error through the computed solution
e_2	User parameter used to evaluate the numerical error through the computed solution
e_T	Total internal energy
F_1	Blending function 1 ($k-\omega$ SST)
F_2	Blending function 2 ($k-\omega$ SST)
FDS	Flux-Difference Splitting
f_{t2}	Model coefficient 5 (Spalart-Allmaras)
f_{v2}	Model coefficient 6 (Spalart-Allmaras)
f_w	Model coefficient 7 (Spalart-Allmaras)
h_T	Total enthalpy
I	Turbulent intensity
k	Turbulent kinetic energy
LES	Large Eddy Simulation
l_sep	Extent of the separated bubble
M	Mach number
p	Static pressure
p_T	Total pressure
Pr	Prandtl number
Pr_t	Turbulent Prandtl number
q_j	Each of the components of the molecular heat flux vector
$\mathrm{R_G}$	Ideal gas constant particularized for a given gas
RANS	Reynolds Averaged Navier-Stokes
Re	Reynolds number
S	Sutherland reference temperature
S^*	Magnitude related to the gradients of the mean velocity components (realizable $k-\varepsilon$)
SWBLI	Shock wave/boundary layer interaction
s	Entropy
T	Static temperature
T_T	Total temperature
t	Time

U^*	Magnitude related with both the gradients of the mean velocity components and the mean rate-of-rotation tensor (realizable $k-\varepsilon$)
u^+	Dimensionless mean tangential velocity
u_j	Each of the components of the velocity vector
v	Velocity (module)
v_n	Normal-to-the-shock velocity component
v_t	Tangential-to-the-shock velocity component
x_j	Each of the components of the coordinate system
y^+	Dimensionless normal to the wall distance
α	Model coefficient 1 ($k-\omega$)
β	Model coefficient 2 ($k-\omega$)
β^*	Model coefficient 3 ($k-\omega$)
γ	Ratio of specific heats
δ	Boundary layer thickness
δ^*	Displacement thickness
δ_{ij}	Identity matrix
ε	Turbulent dissipation rate
ζ	Empirical coefficient (dimensionless mean velocity profile)
θ	Momentum thickness
κ	Model coefficient 8 (Spalart-Allmaras)
λ	Shock wave angle
μ	Molecular viscosity
μ_t	Turbulent eddy viscosity
ν	Kinematic viscosity
$\widetilde{\nu}$	Modified turbulence eddy viscosity
ξ	Deflection angle
ρ	Density
σ	Model coefficient 9 (Spalart-Allmaras)
σ_{ij}	Molecular viscous stress tensor
σ_k	Empirical coefficient (Boussinesq hypothesis)
σ_ε	Model coefficient 4 ($k-\varepsilon$)
σ_ω	Model coefficient 4 ($k-\omega$)
$\sigma_{\omega 2}$	Model coefficient 3 ($k-\omega$ SST)
τ_w	Shear stress at the wall
Ω	Vorticity magnitude
ω	Specific dissipation rate

1 Introduction

Shock wave/boundary layer interactions are present in almost every transonic, supersonic and hypersonic vehicle. As an example, this phenomenon determines the overall performance of transonic airfoils and high-speed inlets, potentially causing significant drag rises, pressure losses and peaks in surface thermomechanical loads, according to Gaitonde [11].

For this reason, during the past decades many efforts have been conducted in order to accurately predict the flow field in these situations. Thus, both experimental and computational fluid dynamics (CFD) studies have been focused on simple two-dimensional and axisymmetric geometries to characterise the important flow physics of the phenomenon, using various approaches [12].

In the current bachelor's thesis, CFD will be used to study the compressible flow over a nominally two-dimensional 20 degree compression corner in the supersonic regime. Hence, the Reynolds Averaged Navier-Stokes (RANS) approach[1] will be used to study the mentioned flow, where a shock wave/turbulent boundary layer interaction occurs, generating a large separation bubble.

The experimental data set that will be used to validate the simulations is extracted from Settles and Dodson [6,7], where a large number of cases involving shock wave/boundary layer interactions, both supersonic and hypersonic, can be found. Thus, the supersonic flow over a two-dimensional compression corner from the original work of Smits et al. [13], has been finally selected due to the amount and quality of available data. Another considered alternative was the data tabulated by Schülein et al. [14], where a nominally two-dimensional interaction produced by an impinging shock was studied. Both the hypersonic regime of the studied flow and the fewer amount of available measurements caused the rejection of the data base.

On the other hand, adaptive mesh refinement methods appear as an alternative to the classical manual methods for mesh refinement. In spite of the fact that the latter techniques require user knowledge of the flow, adaptive mesh refinement allows the user to drive automatic refinement once the features of the flow have been computed. In that way, these techniques, developed over the last years, could reduce both computational and user efforts in the numerical study of a given flow.

In the current project, classical manual and adaptive mesh refinement methods will be compared to assess the suitability of the latter in flows involving shock wave/boundary layer interactions, where the major gradients of fluid properties are confined in a reduced area. For this purpose, the adaptive mesh refinement tool implemented in Ansys Fluent will be used.

In order to use adaptive mesh refinement methods, the OpenFoam library recently developed by Rettenmaier et al. [15] was also considered. Although the promising results showed by this code in multiphase flows, this option was discarded due to the numerous problems that were found during the installation and testing of the software. Moreover, Ansys Fluent allows more flexibility in the refinement criteria, resulting in an overall more adequate tool for the present study. The last alternative for the usage of these methods was to employ an in-house CFD code, such as the one developed by Yao et al. in 2015 [16]. This option was rejected due to the impossibility of access to such a code for an undergraduate student, regarding the kind of flow that was intended to be simulated.

A wide range of numerical investigations have studied various features of shock wave/boundary layer interactions induced by compression ramps [17–21]. In particular, a numerical study with the same experimental data selected for this bachelor's thesis was carried out by Yang et al. [22], where different turbulence models were compared using the RANS approach. Results showed that for the compression ramp, Spalart-Allmaras model had better performance in calculating the pressure distribution, but the skin friction given by the $k-\omega$ SST model was closer to the experimental results.

[1] In fact, the physics of the problem to be resolved are given by the Favre averaging equations (instead of the classical RANS equations). Nonetheless, following the nomenclature used by the authors of the field, the used approach will be denoted as RANS. This issue will be discussed with more detail during Section 3.1.

In parallel, a series of numerical studies have evaluated the performance of adaptive mesh refinement methods applied to several aerodynamic applications [23, 24]. More specifically, a similar study to the one that will be conducted in the current document was performed by Forster [25], where a three-dimensional supersonic shock wave/boundary layer interaction produced by an incident shock was studied. Thus, Ansys Fluent was used to perform RANS simulations, showing promising results when adaptive mesh refinement was applied. Hence, results comparable to the fine mesh solution were obtained, but with reductions in the overall computational cost on the order of 80%.

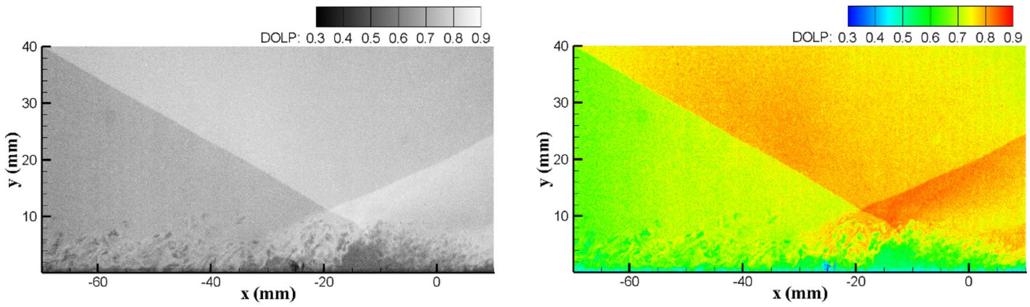

(a) Using the "GrayScale" color map **(b)** Using the "Small Rainbow" color map

Figure 1: Visualization of the interaction between an incoming turbulent boundary layer and an incident shock, strong enough to induce a separation bubble. Images captured using degree of linear polarization (DOLP) with different color maps. Extracted from He et al. [1].

To summarize, the main objective of this bachelor's thesis is to evaluate the benefits of adaptive mesh refinement methods applied to compressible flows involving shock wave/turbulent boundary layer interactions. To achieve this goal, a series of RANS simulations of the supersonic flow over a 20 degree compression corner will be performed using Ansys Fluent.

The difficulties of the simulations to be performed lie in the fact that the viscous effects must be taken into account during the characterization of this high-speed compressible flow (however they are often disregarded for the simulation of many compressible cases involving shock waves). Moreover, to ensure a proper characterization of the interaction itself, the boundary layer needs to be entirely simulated (i.e. no wall functions should be used for the studied case, despite they could lead to fewer cell count and less computational efforts).

For accomplishing with the objectives of the project, the document will be divided into several parts. First of all, Section 2 will present an outline of the physics related to the studied problem. Subsequently, the methodology followed during the numerical study will be described in Section 3; whereas the results from the performed simulations will be discussed in Section 4. Finally, the conclusions from the numerical study and some future lines of research will be presented in Section 5.

2 Theoretical background

Before presenting the methodology and the results from the numerical study, this section will describe some theoretical concepts to support the reader in the understanding of the rest of the document. Therefore, the main features of shock waves, boundary layers, and their interaction will be presented throughout the section.

2.1 Shock waves

Considering a disturbance taking place at a given point in a gas, the information related to the phenomenon is transmitted to other points in the gas by sound waves which propagate in all directions from the source of the disturbance. If the incoming flow is subsonic, the information could be transmitted to the entire flow field, allowing the upstream flow to get adapted to the disturbance.

However, if the incoming flow is supersonic, the information related to the disturbance cannot be transmitted to the entire domain, as the upstream flow is moving faster than the speed of sound. Thus, at some finite distance from the disturbance, the information waves merge, generating a shock wave.

Hence, according to Anderson [26], a shock wave is an extremely narrow region, on the order of several molecular free paths thick ($\sim 10^{-5}$ cm), across which large gradients of fluid properties occur in order to adapt the flow to the downstream disturbances. As a result of these large gradients of flow properties, dissipative mechanisms of friction and thermal conduction are important within the shock wave.

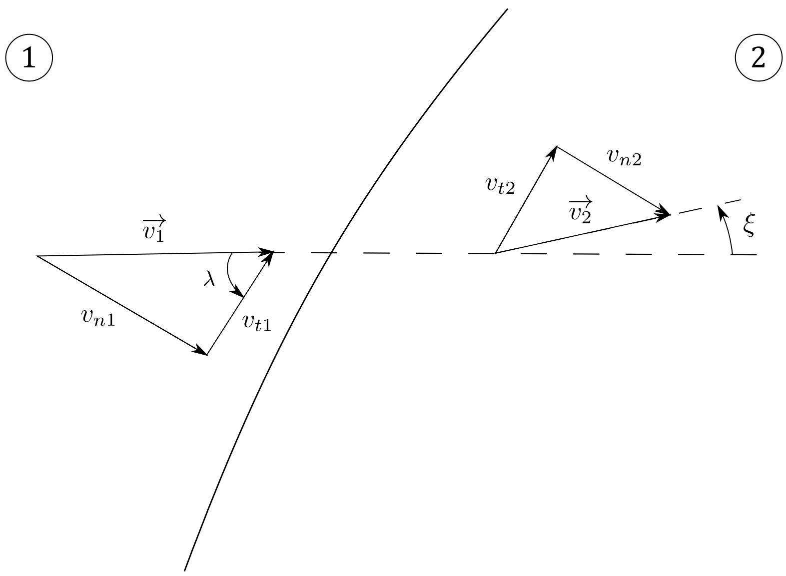

$$\begin{gathered} \mathrm{M}_2 < \mathrm{M}_1 \\ v_2 < v_1 \\ p_2 > p_1 \\ \rho_2 > \rho_1 \\ T_2 > T_1 \\ s_2 > s_1 \\ p_{\mathrm{T}2} < p_{\mathrm{T}1} \\ T_{\mathrm{T}2} = T_{\mathrm{T}1} \end{gathered}$$

Figure 2: Qualitative schematic of the variations of flow properties through a generic shock wave.

Shock waves are usually at an oblique angle to the flow (oblique shock waves), but they can also be found strictly normal to the flow (normal shock waves). A diagram of a generic shock wave and the qualitative variations of fluid properties through it can be found in Figure 2[2], where the upstream and downstream conditions are designated by the subscripts 1 and 2 respectively.

Firstly, the flow through the shock wave is adiabatic, so the total temperature must remain constant. Considering that and the mentioned dissipative effects associated to the viscosity and the thermal conduction, the entropy must increase within the shock, which is only possible if the incoming flow is supersonic [27]. As a result of the increase of the entropy, the total pressure should therefore decrease across the wave.

On the other hand and according to what it has been stated in the former paragraph, the pressure, temperature and density increase across the shock, whereas the Mach number and velocity decrease. Thus, a shock wave is a compression wave which decelerates the flow transforming part of the kinetic energy of the incoming flow into pressure, and thermal energy. Furthermore, Barrero et al. [28] and many other authors state that, for a given fluid, these variations of properties are a function of the upstream Mach number and the angle between the direction of the incoming flow and the shock wave.

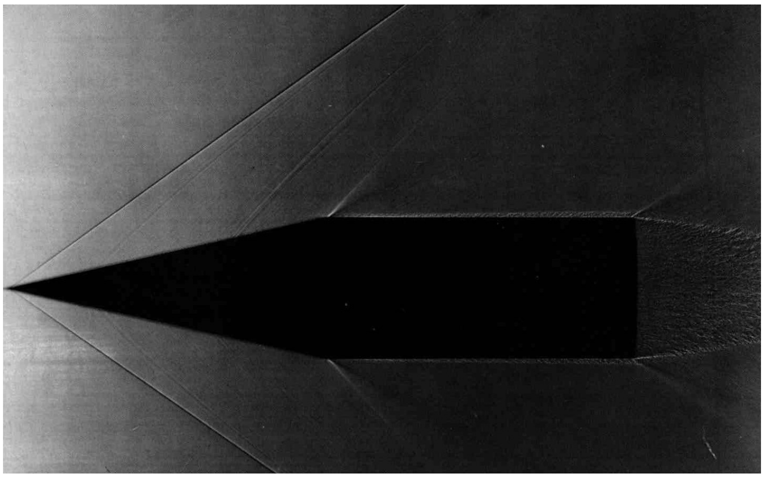

Figure 3: Shadowgraph image of the shock waves over a cone-cylinder of 12.5° semi-vertex angle through air at M= 1.84. Extracted from Van Dyke [2].

Therefore, the major difference between normal and oblique shocks is how much the properties change across the shock wave, not how properties change. As an example, the flow behind an oblique shock might be either subsonic or supersonic, whereas for a normal shock the downstream flow is always subsonic (being the compression process stronger in this latter case) [26]. In particular, the compression of the flow strictly normal to an oblique shock is identical to the one associated to a normal shock under the same conditions; although the tangential-to-the-shock velocity component remains without changes.

[2] From a quantitative point of view, the Rankine-Hugoniot conservation equations provide an inviscid description of the variation of fluid properties through the shock wave, which is strictly treated as a discontinuity.

2.2 Boundary layer

Although the influence of friction is present at the entire flow field, generally it is usually of no consequence except in the boundary region between two flows of widely different velocities (shear layer); and in the thin region adjacent to the body surface immersed in the flow, which is widely known as boundary layer.

In this layer, the velocity and temperature change from the values at the wall (zero and the wall temperature, respectively) to the values of the magnitudes in the external flow. Thus, this region is characterised by steep gradients of velocity and temperature, resulting in a big influence of viscous effects, thermal conduction and mass diffusion, as stated in Anderson [26]. In spite of the fact that this thin layer only occupies a small portion of the flow field, its influence on the overall development of the flow is immense. Moreover, the nature of the flow, laminar or turbulent, strongly determines the behaviour of the flow in this region.

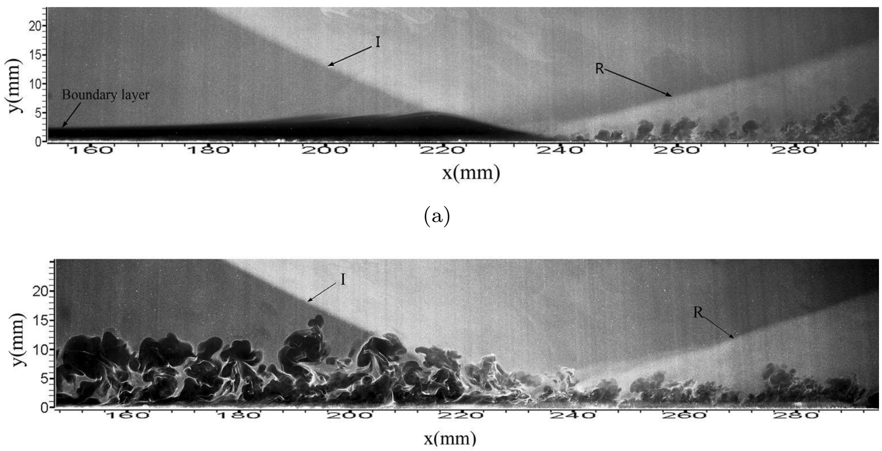

(a)

(b)

Figure 4: Planar laser scattering images of the interaction between a shock wave with an incidence angle of 30° and both laminar (a) and turbulent (b) boundary layers over a flat plate. Incident and reattachment shocks are marked as I and R respectively. Extracted from Qinghu et al. [3].

On one side, in a laminar boundary layer, the transverse exchange of momentum and energy takes place on a molecular scale according to Schlichting et al. [29]. That is, low-momentum fluid particles close to the surface try to decelerate high-momentum fluid particles near the external flow and vice versa. This momentum and energy exchange (and consequently velocity and temperature gradients) produces shear stress and heat flux at the wall of the immersed body.

As a laminar boundary layer develops in the streamwise direction, it is affected by several disturbances, which can be rather damped or amplified. In the latter case, the amplified disturbances may force the transition to a turbulent boundary layer. According to Meseguer et al. [30], the transition process where the boundary layer changes from a laminar to a turbulent state depends on many parameters such as the pressure gradient, the surface roughness and temperature, the suction or blowing at the surface, or the compressibility effects.

However, in spite of the fact that the transition process is affected by many parameters, it is widely extended to define a transition criteria based on the Reynolds number to define the point where the boundary layer changes from laminar to turbulent [30]. Nonetheless, it should be noticed that the transition process actually occurs over a finite distance rather than at a single location.

On the other side, turbulent boundary layers are predominant for most practical applications in aerodynamics. A turbulent flow is characterised by the existence of irregular fluctuations (mixing or eddying motions), that are superimposed on the mean flow [26]. These fluctuations allow not only the momentum and energy exchange on a microscopic scale that appeared in the laminar boundary layer, but a macroscopic transport of momentum and energy as a result of the transport of fluid particles due to the additional mixing motions [29]. Hence, the boundary layer thickness increases in comparison with the laminar case because the low-momentum particles close to the surface are transported far upward due to the extra mixing effect caused by the macroscopic eddies.

In a similar way, as the high-momentum fluid particles are transported closer to the wall, the fluid particles near the surface have higher velocities than in the laminar case. Thus, higher velocity and temperature gradients exist, which at the same time derives into larger shear stress and heat flux at the wall. In addition and according to Schlichting et al. [29], underlying this large scale eddying, there is an isotropic small scale turbulence which transforms the kinetic energy of the large turbulent structures into other forms of energy, including friction and heat.

In order to verify the differences between the two types of flow, Figure 5 shows the friction drag coefficient on a flat plate, for different Reynolds and Mach number flows and both laminar and turbulent regimes. Hence, given a Reynolds number, turbulent skin friction is higher than in the laminar case. Also, the slopes of the turbulent curves are smaller than the laminar ones; that is, the turbulent case has smaller dependence on purely viscous effects (the additional mixing effects are more important).

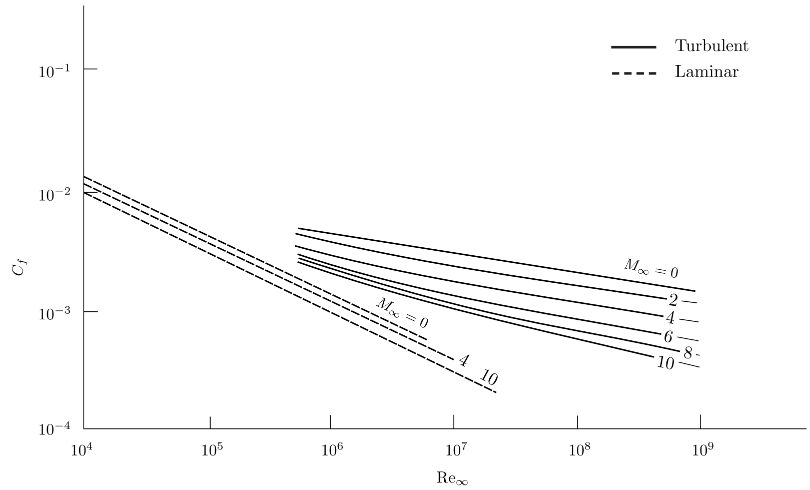

Figure 5: Friction drag coefficient on a flat plate as a function of Reynolds and Mach numbers, for both laminar and turbulent cases. Adiabatic wall, Pr $= 0,75$. Extracted from Van Driest [4].

Additionally, some of the effects of compressibility on the boundary layer could be observed as a result of the former figure. Thus, as the Mach increases, the boundary layer thickness increases, resulting in a decrease in the shear stress at the wall (smaller velocity gradients). Nonetheless, as the Mach number increases, the resulting work of compression and viscous energy dissipation produces larger heat flux at the wall [26]. These compressibility effects are more pronounced in the turbulent case, decreasing the friction drag coefficient by almost an order of magnitude at the higher values of Re_∞ when M_∞ is increased from 0 to 10.

To end with the comparison between the two kinds of boundary layers, when the boundary layer encounters a relatively large adverse pressure gradient, the fluid particles in the viscous layer could be slowed to the point that they cannot overcome the adverse external pressure gradient, causing the boundary layer to separate. Thus, the increased kinetic energy provided by the extra phenomena of mixing allows the turbulent boundary layers to withstand bigger adverse pressure gradients than the laminar boundary layer before separating, as stated in Anderson [26].

On the other hand, if a fully turbulent boundary layer is studied carefully, high-frequency fluctuations of flow properties could be observed. In order to describe the flow field, the fluid magnitudes are usually expressed as the sum of an average value and a fluctuating component. If the resulting average tangential-to-the-wall velocity profile is compared with the laminar velocity profile under the same conditions, it could be stated that the additional mixing effects have produced significant alterations to the former.

Moreover, the former mean velocity profile could be expressed in dimensionless or wall units, given by the dimensionless normal to the wall distance, defined as:

$$y^+ = \frac{y}{\nu}\sqrt{\frac{\tau_w}{\rho}} \tag{1}$$

Where y is the normal distance to the wall, ν is the kinematic viscosity, τ_w is the shear stress at the wall and ρ is the density of the fluid. And, on the other hand, the dimensionless mean tangential velocity, defined as:

$$u^+ = \frac{\overline{u}}{\sqrt{\tau_w/\rho}} \tag{2}$$

Where $\overline{u}$ is the mean tangential velocity. Both experimental and direct numerical simulations (DNS) have showed that these mean dimensionless velocity profiles present a common structure in a wide range of geometries and flows. Thus, according to Schlichting et al. [29], the dimensionless mean velocity profile in a turbulent boundary layer could be divided into the following regions:

- Viscous sub-layer ($y^+ < 5$). In this region, the velocities are very small, resulting in a dominant viscous shear. Thus, the observed behaviour in this layer is on a practical basis laminar, with no effects associated to turbulence. As a result, the observed behaviour matches very well with a linear profile, that is:

  $$u^+ = y^+ \tag{3}$$

  A comparison between the empirical function given by Equation 3 and direct numerical simulation data from a fully developed turbulent boundary layer could be found in Figure 6.

- Log-law region ($y^+ > 30$). In this layer, the flow is fully turbulent and the additional mixing effects are predominant in comparison with the purely viscous phenomena. Thus, the empirical function which fits the observed experimental behaviour has the form of a logarithmic law:

  $$u^+ = \frac{1}{\zeta}\ln y^+ + B \tag{4}$$

  Where ζ and B are empirical coefficients. A comparison between this function and direct numerical simulation data from a fully developed turbulent boundary layer could be found in Figure 6.

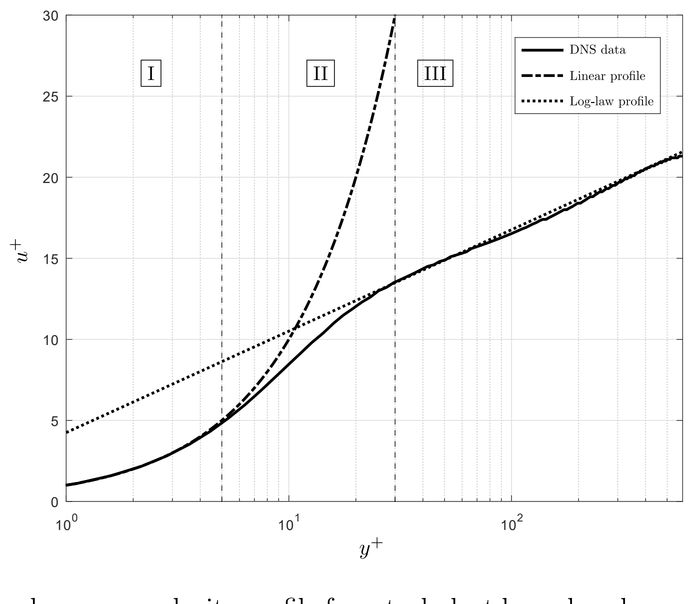

Figure 6: Dimensionless mean velocity profile for a turbulent boundary layer. Regions I, II and III correspond to the viscous sub layer, buffer layer and log-law region respectively. Direct numerical simulation (DNS) data extracted from Moser et al. [5], from a fully developed turbulent channel flow at $\mathrm{Re}_\tau = 590$.

- Buffer layer ($5 < y^+ < 30$). Transition region between the viscous sub-layer and the log-law region. As it could be observed in Figure 6, none of the presented empirical functions fit with the observed behaviour in this region.

To finish with, it should be outlined that the presented dimensionless profile and its regions are of special relevance in computational simulations of turbulent flows. With this, the main features of both laminar and turbulent boundary layers have been described, as well as the compressibility effects on them. Thus, the main characteristics of both shock waves and boundary layers have already been discussed; so that their interaction could be now assessed in the next subsection.

2.3 Shock wave/boundary layer interactions

Shock wave/boundary layer interaction (SWBLI) is a fundamental phenomenon in gas dynamics, that needs to be accounted to evaluate the performance in most of transonic, supersonic and hypersonic vehicles. Moreover, this fluid feature can be critical, or even design limiting, for some aerospace applications, especially in the hypersonic regime [12]. SWBLIs occur in both external and internal flows, being the most outstanding cases the ones sketched in Figure 7, as stated by Gaitonde [11]:

- Overexpanded Nozzles. In a convergent-divergent nozzle where the exit-to-reservoir pressure ratio is such that a shock wave is produced into the divergent part of the device, a shock wave/boundary layer interaction occurs, possibly causing major pressure losses.
- Supersonic Inlets. In this case, important pressure losses associated to either the reduction of the intake efficiency or the flow disruption are present in external, internal and mixed compression inlets as a result of SWBLIs. To minimize these effects, complicated control systems must be installed, adding weight and energy consumption, resulting in an important factor to be accounted in order to improve the vehicle's performance [12].
- Transonic Wings. As a result of the flight Mach number in this kind of vehicles, a SWBLI can be found on the suction surface of their wings, which may cause a substancial rise on the drag and flow unsteadiness (such as buffet).
- Turbomachinery Cascades. According to the operating velocities and temperatures of the gases in these devices, again shock wave/boundary interactions may be found in the suction surfaces of both compressor and turbine blades, causing significant efficiency drops due to the increase of the blade losses.

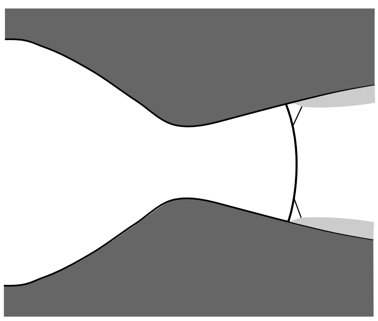

(a) Overexpanded Nozzles.

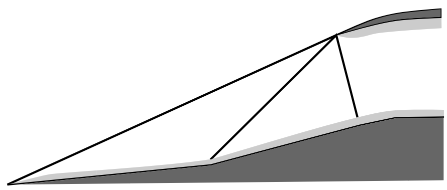

(b) Supersonic Inlets.

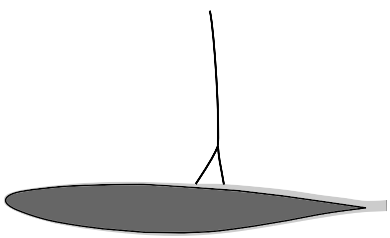

(c) Transonic Wings.

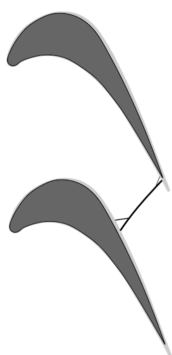

(d) Turbomachiney Cascades.

Figure 7: Sketches of the most outstanding SWBLI applications.

The phenomenon itself is produced from the convergence of a shock wave and a boundary layer, where the former imposes an intense pressure gradient to the latter. Thus according to Babinsky and Harvey [31], this pressure gradient causes the boundary layer to thicken, and consequently to increase its displacement effect, influencing the outer supersonic flow by producing complex shock wave patterns. On the other hand, the adverse pressure gradient imposed to the boundary layer enhances the viscous dissipation effects and, if the flow does not remain strictly laminar throughout the interaction, the production of turbulence.

As it has been stated, this interaction significantly affects the performance of a wide range of devices, but these effects are even more increased when the shock is strong enough to separate the boundary layer. When separation occurs, intense vortexes and even more complex shock patterns are found in the flow field, additionally causing large-scale unsteadiness, leading to buffeting (on transonic wings), buzz (on supersonic inlets), or unsteady side loads; which may result in critical structural damages [31].

Nonetheless, SWBLIs have not entirely negative consequences. That is, the features accounted during the interaction can be used to enhance fuel-air mixing in scramjet combustion chambers, to accelerate the disorganization of hazardous flows (such as wing-trailing vortexes), or even to decrease the wave drag in a vehicle as a result of the splitting of the invicid shock system [12].

Figure 8: Shock wave/laminar boundary layer interaction over an airfoil with an incoming airflow with M= 0.9. Extracted from Van Dyke [2].

Shock wave/boundary layer interactions can be studied distinguishing between laminar and turbulent interactions according to the nature of the incoming boundary layer. However, as stated by Babinski and Harvey [31], considering an averaged flow (which filters out the fluctuating components associated to the turbulent regime), the topology and the overall physics of the two kinds of flow (laminar and turbulent) are essentially the same.

For this reason, both types of interactions will be analyzed globally, taking the most common turbulent interaction to illustrate the flow fields. In spite of this fact, it should be noted that from a quantitative point of view, there are major contrasts between the two kinds of flows. The main difference is the larger extent of the interaction domain appearing in the laminar regime, as a result of the variations in the velocity profiles between the two kinds of flow [26].

Moreover, the analysis will be divided into interactions with (strong interactions) and without separation (weak interactions). In each case, three different situations will be studied (incident shock, ramp-induced and normal shock interactions), which can be then extrapolated so that most of the aerodynamic applications involving SWBLIs can be analyzed.

2.3.1 Weak interactions

A shock wave/boundary layer interaction is termed as weak if it the associated adverse pressure gradient does not produce boundary layer separation. Moreover, the interaction is also said to be weak in the sense that the flow behaviour is not far from the purely inviscid solution.

That is, the main effect caused by this type of interactions is the upstream transmission of the pressure rise caused by the shock through the subsonic part of the boundary layer. This leads to a spreading of the wall pressure distribution over a distance on the order of the boundary layer thickness [31], after which the pressure tends to the downstream inviscid solution (see Figure 10). In order to study this kind of interactions, three different cases will be analyzed (Figures 9, 11 and 12).

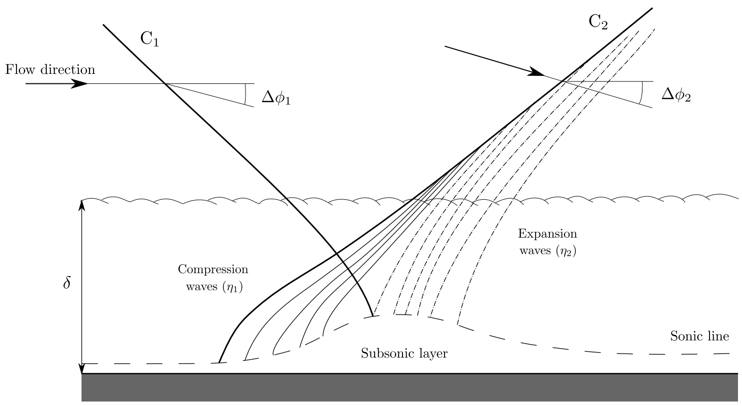

Figure 9: Schematic of the flow field in a turbulent incident shock interaction without boundary layer separation.

To start with, incident shock interactions are present inside mixed-compression supersonic inlets or at the impact of a shock wave generated by an obstacle on a nearby surface. The interaction resulting from the reflection of an oblique shock wave from a turbulent boundary layer is illustrated by the schematic of Figure 9.

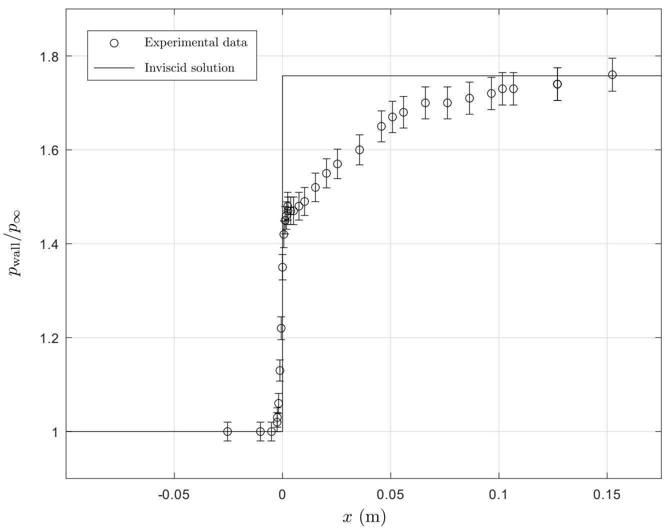

Figure 10: Comparison between experimental mean and inviscid wall pressure distributions over a 8° compression ramp, where a weak SWBLI is produced for an incoming airflow with M= 2.87. Experimental data extracted from Settles et al. [6, 7].

In this case, an incident shock (C_1) penetrates the supersonic part of the boundary layer lowering its intensity until its vanishment at the sonic line. At the same time, the shock steadily bends as it is propagated through the boundary layer due to the decrease of the local Mach number.

As a result of the adverse pressure imposed by the shock, a thickening of the subsonic part of the boundary layer is produced, transmitting part of the pressure rise produced by the incident shock upstream [31]. Thus, a series of compression waves (η_1) are formed upstream of the incident shock, spreading the shock pressure rise. This transmission is enhanced as the subsonic part of the boundary layer (or subsonic channel) is increased.

These compression waves merge at a finite distance from the wall to form the reflected shock (C_2), whose compression corresponds to the inviscid solution far from the wall. Finally, as a result of the presented flow field, a series of expansion waves (η_2) are found immediately downstream of the incident shock C_1 in order to adapt the flow to the far-from-the-wall downstream flow conditions.

To follow with, ramp-induced interactions are produced by sharp changes in the slope of a body surface, producing a change in the direction of the supersonic flow near the surface. This kind of interaction occurs at supersonic-inlet's compression ramps or at any sharp change in the direction of a vehicle's external surface [11]. The main features of the weak interaction produced by a ramp-induced shock are sketched in Figure 11.

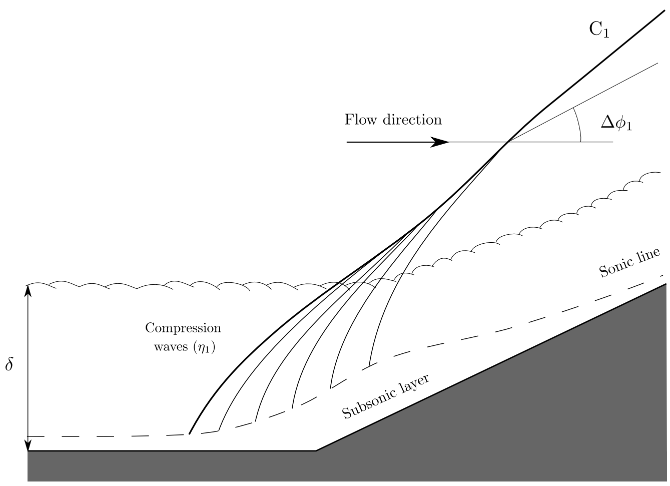

Figure 11: Schematic of the flow field in a turbulent ramp-induced interaction without boundary layer separation.

As in the incident shock case, the pressure rise associated to the ramp-induced shock C_1 is transmitted upstream of the origin of the ramp through the subsonic part of the boundary layer. This results in a thickening of the subsonic channel and the formation of a series of compression waves (η_1) which will then merge in order to form the shock C_1. In this way, the intensity of the shock C_1 increases with the distance from the surface until it reaches the value corresponding to the purely inviscid solution [31].

Finally, normal or near-normal shocks interactions are found in a wide range of situations such as overexpanded nozzles, turbomachinery cascades, transonic wings... In these cases, the compression process associated to the shock decelerates the flow to the subsonic regime without nearly imparting any change in the flow direction. As a consequence of the resulting subsonic flow, downstream disturbances can influence the interaction system, possibly leading to large-scale unsteadiness [31].

The main features of the normal-shock weak interaction are illustrated in Figure 12. Here again, a series of compression waves (η_1) are found as a result of the normal-shock pressure rise transmission through the subsonic part of the boundary layer.

Hence, these compression waves induced by the thickening of the subsonic channel merge into the near normal shock (C_1) at a distance from the wall.

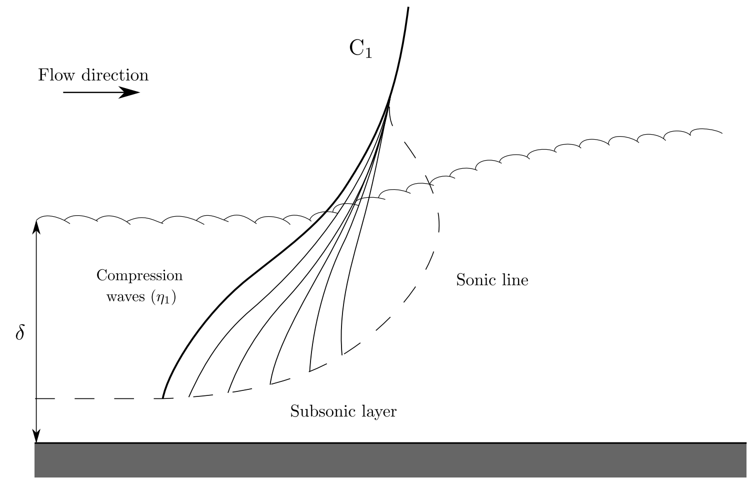

Figure 12: Schematic of the flow field in a turbulent normal shock interaction without boundary layer separation.

Given this flow structure, the compression in the upper supersonic part of the boundary layer is almost isentropic, resulting in a flow with larger stagnation pressure than in the behind-the-shock region of the outer flow. As a consequence, in this region, a supersonic pocket behind the shock exists, where the flow smoothly decelerates to the subsonic regime in order to get adapted to the outer flow.

2.3.2 Strong interactions

A shock wave/boundary layer interaction is known as strong if the associated pressure gradient produces boundary layer separation. Additionally, in this kind of interactions the flow field is markedly different from the purely inviscid solution, due to the major influence of the viscous effects.

Therefore, an upstream transmission of the pressure rise caused by the shock is again found. This subsonic propagation is characterised by an initial steep rise in the wall pressure distribution, followed by a nearly constant-pressure region typical of separated flows and a final more progressive pressure rise after the flow reattachment (see Figure 14). In order to study this kind of interactions, the same cases considered in the previous section will be analyzed (Figures 13, 16 and 17).

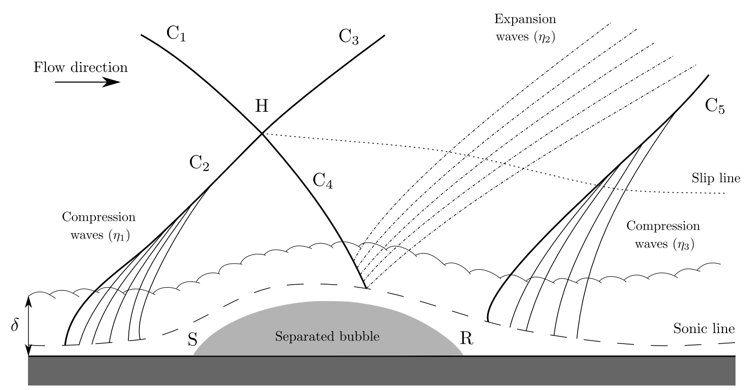

Figure 13: Schematic of the flow field in a turbulent incident shock interaction with boundary layer separation.

First of all, the main features of the flow field regarding a strong incident-shock interaction are sketched in Figure 13. Here, the incident shock (C_1) produces a large pressure rise within the boundary layer that is transmitted upstream through a series of compression waves (η_1), which merge in order to form separation shock C_2. These two shock waves C_1 and C_2 intersect at point H, where both are deflected in order to produce shocks C_4 and C_3 respectively. Once the shock C_4 vanishes at the sonic line, a series of expansion waves (η_2) appear to ensure the continuity of pressure in the outer flow [31].

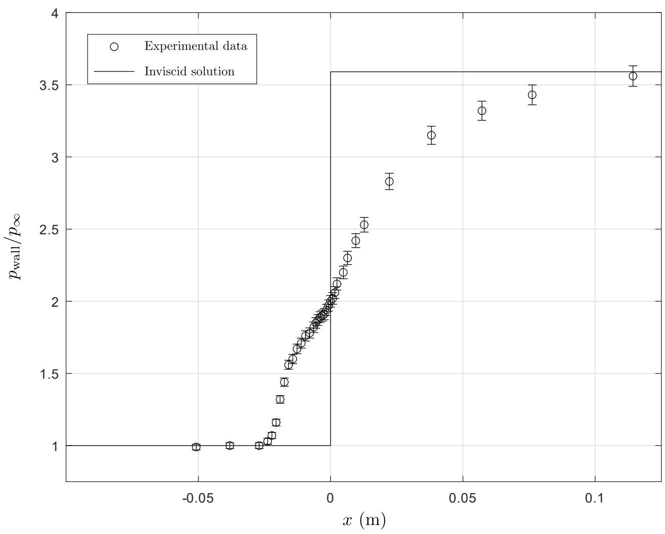

Figure 14: Comparison between experimental mean and inviscid wall pressure distributions over a 20° compression ramp, where a strong SWBLI is produced for an incoming airflow with M= 2.85. Experimental data extracted from Settles et al. [6, 7].

In parallel, a slip line (or trully a shear layer) emanates from point H to ensure a continuous variation of properties between the two flow conditions behind C_4 and C_3, which have the same static pressure and flow direction, but different stagnation pressures.

Finally, as a result of the adverse pressure gradient imposed by the incoming shock, a separated bubble appears, starting at separation point S and ending at reattachment point R, where local high heat-transfer rates are produced [26]. There, another batch of compression waves (η_3) appears, in order to reaccommodate the flow to the outer conditions, finally merging into reattachment shock C_5. Shock waves C_3 and C_5 coalesce far from the wall in order to form the reflected shock solution from the inviscid case [31]. The described flow features can be also observed in the photograph of Figure 15.

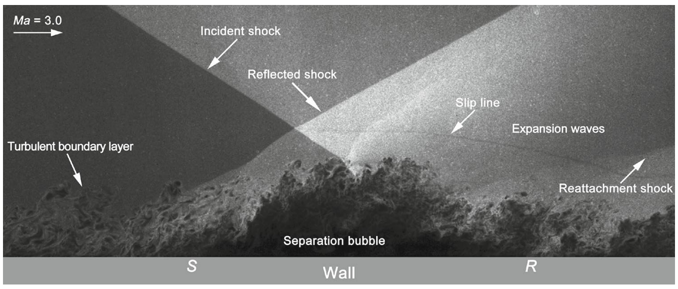

Figure 15: Nano-tracer planar laser scattering (NPLS) image of the instantaneous structure of a shock wave/turbulent boundary layer interaction. S and R indicate the separation and the reattachment points respectively. Extracted from He et al. [8].

Thus, the two-shock system from the inviscid solution (incident plus reflected shock) has been replaced by a complex five-shock pattern. According to Edney [32], this pattern (comprising shocks C_1, C_2, C_3 and C_4) is a Type I shock-shock interference regarding his classification[3]. Furthermore, as a result of the splitting of the inviscid shock pattern, this kind of configurations reduces the production of entropy associated with the shocks, producing at the same time an increase in the production of entropy associated with the boundary layer, which globally may produce a drop in the total entropy production (an consequently in the drag and pressure losses) [31]. This result has been taken into account by designers, which have exploited this effect through various control techniques.

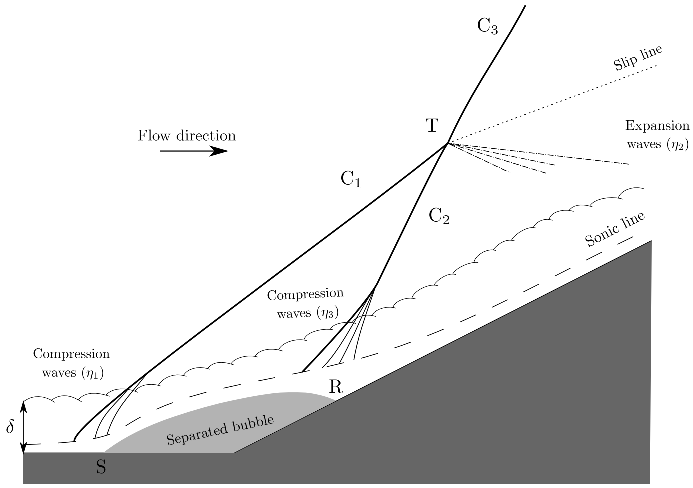

Figure 16: Schematic of the flow field in a turbulent ramp-induced interaction with boundary layer separation.

Secondly, the features of ramp-induced strong interactions are illustrated in Figure 16. In this case, the adverse pressure gradient imposed by the shock wave C_1 produces a separated bubble beginning at separation point S behind the ramp origin and finishing at reattachment point R. As in the previous cases, the pressure rise imposed by C_1 is transmitted upstream through a series of compression waves (η_1), which coalesce to form the shock C_1 itself.

At the same time, as a consequence of the reattachment of the separated bubble, another series of compression waves (η_2) are formed in the vicinity of R, merging into the reattachment shock (C_2). Thus, shocks C_1 and C_2 intersect at point T, where they merge to form shock C_3 which far from the wall will satisfy the inviscid solution of the shock induced by the ramp.

From the triple point T, a centred expansion (η_2) also appears, which propagates in the direction of the wall to adapt the incoming stream to the outer flow direction. Hence, to provide continuity between this two states, a slip line or shear layer emanates from point T. The overall outer supersonic described flow corresponds to an Edney type VI shock-shock interference[4].

Finally, the schematic of Figure 17 shows the main features of a strong normal-shock interaction. Here again, the pressure rise imposed by near-normal shock C_3 is transmitted upstream producing a series of compression waves (η_1), which will then merge in order to produce separation shock C_1. These compression waves η_1 appear in the vicinity of separation point S, which denote the beginning of the separated bubble induced by the incoming normal shock.

[3] For very high incident shock intensities, the shock pattern is replaced by an Edney Type II interference, with a near-normal shock between the two triple points marking the end of shocks C_1 and C_3. The analysis of this case has been omitted in the current document due to its minor importance, only appearing in a series of isolated cases in the hypersonic regime.

[4] There is again a special case appearing at low Mach numbers, where the compatibility at point T is instead achieved through a very weak fourth shock C_4, which emanates from point T and propagates towards the wall [31]. As in the previous case, the details of this rare interaction are not included in the current document.

This bubble is extended up to reattachment point R, from which its vicinity another near-normal shock C_2 is produced to equal both static pressure and flow direction between the two states separated by the slip line. Moreover, shocks C_1 and C_3 intersect at point T, where a slip line is again formed to separate the two mentioned compatible states. Depending on the case, the flow behind shock C_2 may be supersonic, with a Mach number close to unity. In that case, a supersonic region or tongue is formed, where a smooth nearly-isentropic compression to the subsonic regime is produced. Hence, the overall outer-supersonic flow corresponds to an Edney Type VI interference, or the so called lambda shock pattern. Figure 8 illustrates the presented flow organisation over the suction surface of an airfoil.

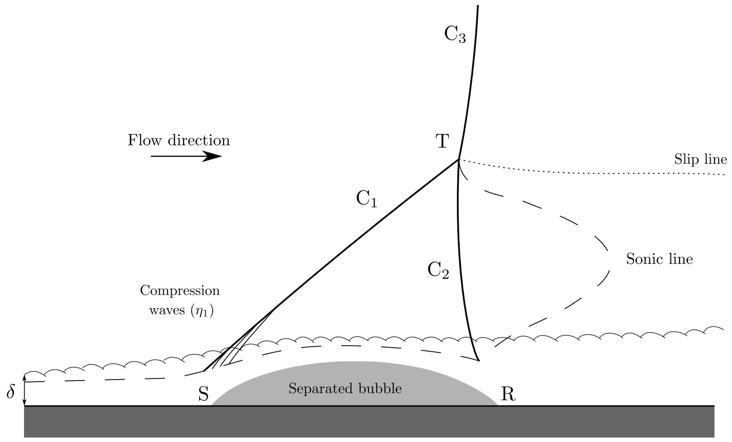

Figure 17: Schematic of the flow field in a turbulent normal shock interaction with boundary layer separation.

2.3.3 Concluding remarks

A review of the main features of shock wave/boundary layer interactions has been carried out through this section, describing the flow field within the most outstanding cases involving both weak and strong interactions. To summarize, one of the most significant consequences of the interaction is the spreading of the steep pressure gradient imposed by the shock, so that it is experienced upstream of where it would have been located in the inviscid case.

Furthermore, specially if the shock is strong enough to cause separation of the boundary layer, complex shock patterns are produced in the outer supersonic part of the flow field, whose nature depend on whether the case is. Shock wave/boundary layer interactions, specially of the strong type, may also produce large-scale flow unsteadiness, which can lead to significant negative consequences. Examples of this kind of phenomena are transonic buffeting or supersonic-inlet buzz.

Interactions in the hypersonic regime have distinctive features that are worth to be outlined. As a result of the high enthalpy level of the outer flow, disociation, chemical reactions and ionisation are produced, realising large amounts of heat that modify the thermodynamic and transport properties of the fluid, influencing the overall flow field [31]. One of the major consequences of this effect is the increase of the wall heat-transfer rate, which takes special importance in separated flows, possibly leading to design limiting thermal loads [33]. In order to mitigate this effect, one of the most extended solutions is wall cooling, which produces a contraction of the interaction domain in comparison to the adiabatic case, and an increase in the boundary layer resistance to separation [34,35].

In the current document, most of the efforts carried out have been focused on two-dimensional shock wave/boundary layer interactions. Nonetheless, it should be noticed that nearly all practical situations are three-dimensional. Although many two-dimensional flow features can be extrapolated to three-dimensional interactions, according to Babinsky and Harvey [31], a consistent topological description of the flow field organisation in three-dimensional interactions has not been yet achieved, being one of the major obstacles the definition of boundary layer separation in these flow fields.

Finally, given the difficulty to avoid shock wave/boundary layer interactions within a flow, the importance of the control techniques of these phenomena should be outlined. In order to prevent boundary layer separation and/or stabilise the interaction system, boundary layer blowing and suction, vortex generators and wall cooling have been proved to be effective [11]. However, if the aim is to decrease the overall drag or pressure loss throughout the interaction, the situation becomes more complicated due to the dual entropy production taking place on both the shock waves and the boundary layer [31].

3 Methodology

In this section, the methodology followed during the development of the numerical study will be presented. Firstly, the governing equations that characterise the physics of the problem will be described. Then, the specific case to be simulated will be discussed, so that the generated grids for simulating the flow through a finite volume method could be presented in the following subsection. Finally, the solver set up and the adaptive mesh refinement procedure will be presented in the two last subsections.

3.1 Governing equations

The physics of the problem to be resolved are given by the Favre averaging equations, which take into account both time and density fluctuations. In spite of the classical Reynolds-Averaged Navier-Stokes (RANS) equations, which are based on incompressible flow assumptions, the Favre formulation provides an adequate framework for modelling flows with significant density variations.

Thus, in order to derive the equations to be resolved in the studied case, the conservative form of the Navier-Stokes equations for an unsteady compressible flow where the volumetric forces' source term has been eliminated[5], will be taken as a starting point:

- Continuity

$$\frac{\partial \rho}{\partial t} + \frac{\partial}{\partial x_j}(\rho u_j) = 0 \tag{5}$$

- Momentum

$$\frac{\partial}{\partial t}(\rho u_i) + \frac{\partial}{\partial x_j}(\rho u_j u_i) = -\frac{\partial p}{\partial x_i} + \frac{\partial}{\partial x_j}(\sigma_{ij}) \tag{6}$$

- Energy

$$\frac{\partial}{\partial t}(\rho e_T) + \frac{\partial}{\partial x_j}(\rho u_j h_T) = -\frac{\partial q_j}{\partial x_j} + \frac{\partial}{\partial x_j}(u_i \sigma_{ij}) \tag{7}$$

  Where the total enthalpy could be expressed as $h_T = e_T + p/\rho$.

To average the former equations, classical time averaging (Reynolds averaging) will be introduced for pressure and density as:

$$\overline{\Phi} = \lim_{T\to\infty} \frac{1}{T} \int_{t_0}^{t_0+T} \Phi \; dt \tag{8}$$

Where Φ represents a generic magnitude of the fluid, $\overline{\Phi}$ its standard time averaging and t_0 an initial time condition. Additionally, density weighted time averaging (Favre averaging) will be introduced for the temperature and velocity components as:

$$\widetilde{\Phi} = \frac{\overline{\rho \Phi}}{\overline{\rho}} \tag{9}$$

Where $\widetilde{\Phi}$ represents the Favre averaging of a generic fluid magnitude. Therefore, denoting the density weighted fluctuations as $''$, the mean compressible Navier-Stokes equations could be written as:

- Continuity

$$\frac{\partial \overline{\rho}}{\partial t} + \frac{\partial}{\partial x_j}(\overline{\rho}\widetilde{u_j}) = 0 \tag{10}$$

[5] For the studied flow, volumetric forces have a minor effect on the overall flow and could be initially disregarded.

- Momentum

$$\frac{\partial}{\partial t}(\overline{\rho}\widetilde{u_i}) + \frac{\partial}{\partial x_j}(\overline{\rho}\widetilde{u_j}\widetilde{u_i}) = -\frac{\partial \overline{p}}{\partial x_i} + \frac{\partial}{\partial x_j}(\widetilde{\sigma_{ij}} - \overline{\rho u_j'' u_i''}) \tag{11}$$

- Energy

$$\begin{gathered}\frac{\partial}{\partial t}(\overline{\rho}\widetilde{e_T}) + \frac{\partial}{\partial x_j}(\overline{\rho}\widetilde{u_j}(\widetilde{e_T} + \overline{p}/\overline{\rho})) = -\frac{\partial \widetilde{q_j}}{\partial x_j} + \frac{\partial}{\partial x_j}(\widetilde{u_i}(\widetilde{\sigma_{ij}} \\ -\overline{\rho u_j'' u_i''})) + \frac{\partial}{\partial x_j}(-c_{\mathrm{p}}\overline{\rho u_j'' T''} + \overline{u_i'' \sigma_{ij}} - \overline{\rho u_j'' {}^1\!/_2 u_i'' u_i''})\end{gathered} \tag{12}$$

Where again the total mean energy could be expressed as $\widetilde{e_T} = \widetilde{e} + {}^1\!/_2\widetilde{u_i}\widetilde{u_i} + k$. On the other hand, for a newtonian fluid, the mean molecular viscous stress is:

$$\widetilde{\sigma_{ij}} = \mu\left(\frac{\partial \widetilde{u_i}}{\partial x_j} + \frac{\partial \widetilde{u_j}}{\partial x_i} - \frac{2}{3}\frac{\partial \widetilde{u_k}}{\partial x_k}\delta_{ij}\right) \tag{13}$$

And the molecular heat flux can be written as:

$$\widetilde{q_j} = -c_{\mathrm{p}}\,\frac{\mu}{\mathrm{Pr}}\,\frac{\partial \widetilde{T}}{\partial x_j} \tag{14}$$

Where the Prandtl number (Pr) is assumed to have a constant value. As a result of the introduced averaging, four extra terms depending on the mass-averaged fluctuations of the fluid magnitudes have appeared: the turbulent Reynolds stress ($-\overline{\rho u_j'' u_i''}$), the turbulent heat flux ($c_{\mathrm{p}}\overline{\rho u_j'' T''}$) and the molecular diffusion and turbulent transport terms ($\overline{u_i'' \sigma_{ij}}$ and $-\overline{\rho u_j'' {}^1\!/_2 u_i'' u_i''}$).

Hence, in order to subsequently resolve the equations via a finite volume method, these terms need to be modelled as a function of the averaged properties. For this purpose, Boussinesq approximation will be used, introducing the turbulent eddy viscosity (μ_t) and Prandtl number (Pr_t) for modelling the diffusion and heat-transfer associated to turbulence. Thus, a linear relationship between the turbulent shear stress and the mean strain-rate tensor, and the turbulent heat flux and molecular heat transfer rate will be assumed [36], expressing the mentioned terms as:

- Turbulent Reynolds stress:

$$-\overline{\rho u_j'' u_i''} = -\frac{2}{3}\overline{\rho}k\delta_{ij} + \mu_t\left[\left(\frac{\partial \widetilde{u_i}}{\partial x_j} + \frac{\partial \widetilde{u_j}}{\partial x_i}\right) - \frac{2}{3}\frac{\partial \widetilde{u_k}}{\partial x_k}\delta_{ij}\right] \tag{15}$$

- Turbulent heat flux:

$$c_{\mathrm{p}}\overline{\rho u_j'' T''} = -c_{\mathrm{p}}\,\frac{\mu_t}{\mathrm{Pr}_t}\,\frac{\partial \widetilde{T}}{\partial x_j} \tag{16}$$

  Where the turbulent Prandtl number (Pr_t) is assumed to have a constant value.

- Molecular diffusion and turbulent transport terms:

$$\overline{u_i'' \sigma_{ij}} - \overline{\rho u_j'' {}^1\!/_2 u_i'' u_i''} = \left(\mu + \frac{\mu_t}{\sigma_k}\right)\frac{\partial k}{\partial x_j} \tag{17}$$

  Where σ_k is a coefficient, whose value depends on the selected turbulence model.

Introducing the former modelling into the derived averaged equations:

- Continuity

$$\frac{\partial \overline{\rho}}{\partial t} + \frac{\partial}{\partial x_j}(\overline{\rho}\widetilde{u_j}) = 0 \tag{18}$$

- Momentum

$$\frac{\partial}{\partial t}(\overline{\rho}\widetilde{u_i}) + \frac{\partial}{\partial x_j}(\overline{\rho}\widetilde{u_j}\widetilde{u_i}) = -\frac{\partial \overline{p}}{\partial x_i} + \frac{\partial}{\partial x_j}\left[(\mu + \mu_t)\left(\frac{\partial \widetilde{u_i}}{\partial x_j} + \frac{\partial \widetilde{u_j}}{\partial x_i} - \frac{2}{3}\frac{\partial \widetilde{u_k}}{\partial x_k}\delta_{ij}\right) - \frac{2}{3}\overline{\rho}k\delta_{ij}\right] \tag{19}$$

- Energy

$$\frac{\partial}{\partial t}(\overline{\rho}(\widetilde{e}+{}^1\!/_2\widetilde{u_i}\widetilde{u_i}+\cancel{k}^{\boxed{1}}))+\frac{\partial}{\partial x_j}(\overline{\rho}\widetilde{u_j}((\widetilde{e}+{}^1\!/_2\widetilde{u_i}\widetilde{u_i}+\cancel{k}^{\boxed{1}})+\overline{p}/\overline{\rho}))=\frac{\partial}{\partial x_j}\left(\widetilde{u_i}\left[(\mu+\mu_t)\left(\frac{\partial\widetilde{u_i}}{\partial x_j}+\frac{\partial\widetilde{u_j}}{\partial x_i}-\frac{2}{3}\frac{\partial\widetilde{u_k}}{\partial x_k}\delta_{ij}\right)-\frac{2}{3}\overline{\rho}k\delta_{ij}\right]\right)+\frac{\partial}{\partial x_j}\left(\left(\frac{\mu}{\mathrm{Pr}}+\frac{\mu_t}{\mathrm{Pr}_t}\right)c_\mathrm{p}\frac{\partial\widetilde{T}}{\partial x_j}\right)+\cancel{\left(\mu+\frac{\mu_t}{\sigma_k}\right)\frac{\partial k}{\partial x_j}}^{\boxed{2}} \tag{20}$$

Where terms $\boxed{1}$ and $\boxed{2}$ are often ignored in high speed compressible flow modelling assuming $k \ll \widetilde{e_T}$, which is a valid hypothesis in most of the flows of engineering interest according to Wilcox [37].

At this point, eliminating non-stationary terms[6], as well as terms $\boxed{1}$ and $\boxed{2}$, the conservative form of the Favre equations for the current problem could be obtained. To close the system of equations, an equation of state will be also introduced, assuming ideal gas hypothesis. Hence, the resulting set of equations is given by:

- Continuity

$$\frac{\partial}{\partial x_j}(\overline{\rho}\widetilde{u_j})=0 \tag{21}$$

- Momentum

$$\frac{\partial}{\partial x_j}(\overline{\rho}\widetilde{u_j}\widetilde{u_i})=-\frac{\partial\overline{p}}{\partial x_i}+\frac{\partial}{\partial x_j}\left[(\mu+\mu_t)\left(\frac{\partial\widetilde{u_i}}{\partial x_j}+\frac{\partial\widetilde{u_j}}{\partial x_i}-\frac{2}{3}\frac{\partial\widetilde{u_k}}{\partial x_k}\delta_{ij}\right)-\frac{2}{3}\overline{\rho}k\delta_{ij}\right] \tag{22}$$

- Energy

$$\frac{\partial}{\partial x_j}(\overline{\rho}\widetilde{u_j}((\widetilde{e}+{}^1\!/_2\widetilde{u_i}\widetilde{u_i}+\overline{p}/\overline{\rho}))=\frac{\partial}{\partial x_j}\left(\widetilde{u_i}\left[(\mu+\mu_t)\left(\frac{\partial\widetilde{u_i}}{\partial x_j}+\frac{\partial\widetilde{u_j}}{\partial x_i}-\frac{2}{3}\frac{\partial\widetilde{u_k}}{\partial x_k}\delta_{ij}\right)-\frac{2}{3}\overline{\rho}k\delta_{ij}\right]\right)+\frac{\partial}{\partial x_j}\left(\left(\frac{\mu}{\mathrm{Pr}}+\frac{\mu_t}{\mathrm{Pr}_t}\right)c_\mathrm{p}\frac{\partial\widetilde{T}}{\partial x_j}\right) \tag{23}$$

- Equation of state (ideal gas assumption)

$$\frac{\overline{p}}{\overline{\rho}}=\gamma\ R_\mathrm{G}\ \widetilde{T} \tag{24}$$

Where γ and R_G represent the ratio of specific heats and the ideal gas constant particularized for the studied gas. Both coefficients will take the values corresponding to air in the studied conditions.

Finally, due to the large temperature variations taking place in the studied flow, instead of assuming a constant value, Sutherland's law will be used to calculate the dynamic viscosity (μ) at each point of the computational domain. This law is given by the following expression:

$$\mu=C_1\ \frac{\widetilde{T}^{3/2}}{\widetilde{T}+S} \tag{25}$$

Where C_1 is a constant and S is the Sutherland reference temperature.

[6] In the current analysis, non-stationary terms are eliminated since steady-state formulation will be used to numerically resolve the equations.

3.1.1 Turbulence modelling

Due to the turbulent eddy viscosity (μ_t) introduced to model the turbulent diffusion effects, the presented set of equations cannot be yet resolved. Thus, more equations should be included in the system to obtain μ_t, which will be given by turbulence models.

According to Gatski [36], these models are the result of the generalization of experimental observations and they are not unique. In fact, as stated by Wilcox [37], turbulence models are generally categorised by the number of additional partial-differential equations they introduce, being the zero, one and two-equation models the most popular ones. In particular, the turbulence models that will be used in the current numerical study will be the following:

- Spalart-Allmaras model. In 1994, Spalart and Allmaras developed this one-equation model, which introduces the modified turbulence eddy viscosity ($\widetilde{\nu}$) in order to subsequently calculate μ_t [38]. For a steady-state flow, the introduced partial-differential equation is given by:

$$u_j \frac{\partial \widetilde{\nu}}{\partial x_j} = \frac{1}{\sigma}\left(\frac{\partial}{\partial x_j}\left[(\nu+\widetilde{\nu})\frac{\partial \widetilde{\nu}}{\partial x_j}\right] + c_{b2}\frac{\partial \widetilde{\nu}}{\partial x_i}\frac{\partial \widetilde{\nu}}{\partial x_i}\right) + c_{b1}(1-f_{v2})\widetilde{S}\widetilde{\nu} - \left[c_{w1}f_w - \frac{c_{b1}}{\kappa^2}f_{t2}\right]\left(\frac{\widetilde{\nu}}{d}\right)^2 \quad (26)$$

  Where d represents the distance from the field point to the nearest wall, and f_{v2}, f_{t2}, f_w, c_{b1}, c_{b2}, c_{w1}, σ and κ are model coefficients. Once this field has been obtained, the turbulent eddy viscosity at each point of the computational domain is calculated as:

$$\mu_t = \overline{\rho}\ \widetilde{\nu}\ f_{v1} \quad (27)$$

  Where the function f_{v1} is given by:

$$f_{v1} = \frac{(\widetilde{\nu}/\nu)^3}{(\widetilde{\nu}/\nu)^3 + {c_{v1}}^3} \quad (28)$$

  Again, c_{v1} is a semiempiric coefficient given by the model. It should be noted that in this model the turbulent kinetic energy (k) is not calculated, so the terms involving this magnitude are ignored within the initial set of averaged equations.

  Finally, it should be also outlined that the presented transport equation omits an additional trip term included in the original model presented in 1994. Most users do not include this trip term, assuming the flow to be fully turbulent.

- Standard $k-\varepsilon$ model. In 1974, Launder and Spalding [39], developed this two-equation model, which introduces transport equations for the turbulent kinetic energy (k) and the turbulent dissipation rate (ε).

  Since its publication, it has been widely extended, mainly due to its great performance in predicting an important range of both internal and external flows without the need for case-by-case adjustment of the model constants. However, it should be noted that generally its performance in flows with strong adverse pressure gradients (especially involving separation) is not very accurate. For a steady-state flow, the transport equations introduced by the model are given by:

$$\frac{\partial}{\partial x_i}(\overline{\rho} k \widetilde{u_i}) = \frac{\partial}{\partial x_j}\left[\left(\mu + \frac{\mu_t}{\sigma_k}\right)\frac{\partial k}{\partial x_j}\right] + \widetilde{\sigma_{ij}}\frac{\partial \widetilde{u_i}}{\partial x_j} - \overline{\rho}\varepsilon \quad (29)$$

$$\frac{\partial}{\partial x_i}(\overline{\rho}\varepsilon \widetilde{u_i}) = \frac{\partial}{\partial x_j}\left[\left(\mu + \frac{\mu_t}{\sigma_\varepsilon}\right)\frac{\partial \epsilon}{\partial x_j}\right] + C_{1\varepsilon}\frac{\varepsilon}{k}\widetilde{\sigma_{ij}}\frac{\partial \widetilde{u_i}}{\partial x_j} - C_{2\varepsilon}\overline{\rho}\frac{\varepsilon^2}{k} \quad (30)$$

  Where $\widetilde{\sigma_{ij}}$ is given by Equation 13 and σ_k, σ_ε, $C_{1\varepsilon}$ and $C_{2\varepsilon}$ are model constants. Thus, the turbulent eddy viscosity is calculated from the kinetic energy and the turbulent dissipation rate at each point of the computational domain as:

$$\mu_t = \overline{\rho}\ C_\mu\ \frac{k^2}{\varepsilon} \quad (31)$$

  Where again C_μ is an empirical constant given by the model.

- Realizable $k-\varepsilon$ model. This model is a modification of the original $k-\varepsilon$ model previously introduced. Hence, the same transport equation to model the turbulent kinetic energy (k) is used; whereas some constraints are introduced in the turbulent dissipation rate equation, preventing non physical results [36]. Specifically, this last transport equation for ε is now given for a steady-state flow by:

$$\frac{\partial}{\partial x_j}(\overline{\rho}\varepsilon\widetilde{u_j}) = \frac{\partial}{\partial x_j}\left[\left(\mu + \frac{\mu_t}{\sigma_k}\right)\frac{\partial \varepsilon}{\partial x_j}\right] + \overline{\rho}C_{1\varepsilon*}S^*\varepsilon - \overline{\rho}C_{2\varepsilon*}\frac{\varepsilon^2}{k+\sqrt{\nu\varepsilon}} \tag{32}$$

Where $C_{1\varepsilon*}$ and $C_{2\varepsilon*}$ are empirical constants, and S^* is a magnitude related to the gradients of the mean velocity components. In this case, the turbulent eddy viscosity (μ_t) is calculated as in the standard model (Equation 31), but changing the way the parameter C_μ is calculated:

$$C_\mu = \frac{\varepsilon}{A_0\ \varepsilon + A_s\ k\ U^*} \tag{33}$$

Where A_0 and A_s are model coefficients and U^* is a magnitude related with both the gradients of the mean velocity components and the mean rate-of-rotation tensor.

- Standard $k-\omega$ model. Developed by Wilcox in 1998, this two-equation model introduces a transport equation for the specific dissipation rate (ω) instead of the turbulent dissipation rate equation used in the two previously presented models. This new magnitude is defined as:

$$\omega = \frac{\varepsilon}{C_\mu\ k} \tag{34}$$

Therefore, for a steady-state flow, the transport equations introduced by the model for both the turbulent kinetic energy and the specific dissipation rate are given by Equations 35 and 36.

$$\frac{\partial}{\partial x_j}(\overline{\rho}k\widetilde{u_j}) = \frac{\partial}{\partial x_j}\left[\left(\mu + \frac{\mu_t}{\sigma_k}\right)\frac{\partial k}{\partial x_j}\right] + \widetilde{\sigma_{ij}}\frac{\partial \widetilde{u_i}}{\partial x_j} - \beta^*\ \overline{\rho}\omega k \tag{35}$$

$$\frac{\partial}{\partial x_j}(\overline{\rho}\omega\widetilde{u_j}) = \frac{\partial}{\partial x_j}\left[\left(\mu + \frac{\mu_t}{\sigma_\omega}\right)\frac{\partial \omega}{\partial x_j}\right] + \alpha\frac{\omega}{k}\widetilde{\sigma_{ij}}\frac{\partial \widetilde{u_i}}{\partial x_j} - \beta\ \overline{\rho}\omega^2 \tag{36}$$

Where α, β, β^*, σ_ω are coefficients given by the model. Once the two magnitudes are computed at each of point of the computational domain, the turbulent eddy viscosity is then calculated as:

$$\mu_t = \frac{\overline{\rho}\ k}{\omega} \tag{37}$$

- $k-\omega$ SST model. As a result of the strong dependence on the freestream turbulence conditions that presented the original $k-\omega$ model, Menter first developed the $k-\omega$ BSL model to try to mitigate this effect. This version implements a blending between $k-\omega$ near the wall and the less freestream-dependant $k-\varepsilon$ model far from this surface, so that the benefits from both approaches could be obtained.

The $k-\omega$ SST model, developed by Menter in 1994, is a derivation of the presented $k-\omega$ BSL model. The only difference in comparison with the BSL version is the implementation of a limiter in the turbulent eddy viscosity calculation, in order to provide a better performance in flows involving adverse pressure gradients and boundary layer separation [40]. Hence, $k-\omega$ SST model uses the same transport equation for k as the standard $k-\omega$ model (Equation 35); whereas for a steady-state flow, the partial-differential equation for ω is given by:

$$\frac{\partial(\overline{\rho}\widetilde{u_j}\omega)}{\partial x_j} = \frac{\partial}{\partial x_j}\left[\left(\mu + \frac{\mu_t}{\sigma_\omega}\right)\frac{\partial \omega}{\partial x_j}\right] + \alpha\frac{\omega}{k}\widetilde{\sigma_{ij}}\frac{\partial \widetilde{u_i}}{\partial x_j} - \beta\ \overline{\rho}\omega^2 + 2(1-F_1)\frac{\overline{\rho}\sigma_{\omega 2}}{\omega}\frac{\partial k}{\partial x_j}\frac{\partial \omega}{\partial x_j} \tag{38}$$

Where $F_1 \in [0,1]$ is the blending function which transforms the calculation from the $k-\omega$ to the $k-\varepsilon$ model, according to the position of the computational cell with respect to the adjacent surfaces; and $\sigma_{\omega 2}$ is a coefficient given by the model. Finally, once k and ω fields are calculated, the turbulent eddy viscosity is obtained as:

$$\mu_t = \frac{\overline{\rho}\ a_1 k}{\max\ (a_1\omega,\ \Omega F_2)} \tag{39}$$

Where Ω is the vorticity magnitude, a_1 is a model coefficient, and F_2 is another blending function defined in the model. Thus, the turbulent eddy viscosity calculation changes depending on whether the pressure gradient is adverse or favourable.

- Modified $k-\omega$ SST model. In spite of the improvements that the $k-\omega$ SST model achieves in comparison with the standard $k-\omega$ model, SST model does not show the same good performance where large adverse pressure gradients are taking place. More specifically, according to Wilcox [37], the SST model usually performs well in flows with moderate adverse pressure gradients leading to small boundary layer separation. Nonetheless, when large pressure gradients are involved within the flow field (such as in shock wave/boundary layer interactions), the SST model often overpredicts the extent of the separated region.

  Additionally, Georgiadis and Yoder [41] noticed that the $k-\omega$ BSL underpredicted the separation region under the same flow conditions. Given that the only difference between the two models is the limiter implemented in the calculation of μ_t, Georgiadis and Yoder conducted an investigation to study the effect of varying the value of the coefficient a_1 (which was identified as one of the most influencing parameters in the prediction of the separation region). Thus, different shock wave/boundary layer interactions were simulated with this purpose, finally stating that the optimal value for accurately predict this kind of flows was $a_1 = 0.355$ (instead of the original $a_1 = 0.31$).

Introducing one of the presented turbulence models into the original set of averaged equations, the system is completely closed and could be then solved through a finite-volume method in order to calculate the fluid properties at each point of the computational domain. From now on and for the sake of simplicity, all the averaged magnitudes will be denoted without their stresses, although they will be explicitly presented as mean values. Moreover, for clearness, the presented Favre equations will be named from this point as RANS equations or RANS approach, following the tendency of the authors of the field.

3.2 Experimental data

In the early 1990s, Settles and Dodson [6] defined an experimental shock wave/turbulent boundary interaction data base, with the aim to be used for turbulence model validation. For this purpose, 105 data sets were subjected to an assessment procedure based on rigorous criteria, such as well-defined experimental boundary conditions, adequate documentation, proper data resolution... After this stage, 11 test cases were selected, including both two and three-dimensional shock wave/boundary layer interactions, with and without boundary layer separation. Furthermore, 5 of the data sets studied hypersonic flows, and 6 supersonic ones.

Three years later, Settles and Dodson published an amendment to the former report, including both additions and corrections to the original data, and new test cases that were not considered previously [7]. As a result of the quality and amount of available data, the original work of Smits et al. [13] presented in both data bases will be used to validate the simulations that will be performed.

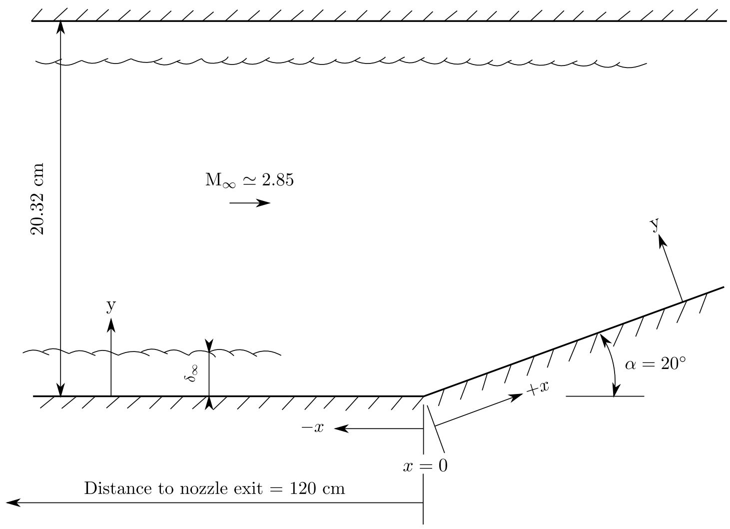

Figure 18: Schematic of Princeton's High Reynolds Number Supersonic Wind Tunnel. Facilities used for the study of the supersonic flow over a 20° compression corner.

The selected case comprised the study of nominally two-dimensional supersonic flows ($M \approx 2.9$) over compression corner angles of 8, 16, 20 and 24 degrees, resulting in SWBLIs with and without boundary layer separation. As stated by Settles and Dodson [6], oil-flow patterns studies were used to demonstrate the two-dimensional behaviour of the experiments for all but the largest compression corner angle, where significant three-dimensional perturbations were observed.

For this reason, the 20° compression corner case has been been finally selected for the numerical study, where the shock wave/boundary layer interaction produces a large separation bubble. Furthermore, the experimental facilities used in the study are illustrated by the sketch of Figure 18. Thus, the supersonic flow ($M \simeq 2.85$) over a compression ramp placed 120 centimetres downstream of the nozzle exit was established in order to study the incoming boundary layer interaction with the ramp-induced shock wave.

In parallel, the same schematic of Figure 18 shows the coordinate system that will be used in the numerical study (which is the same used for the tabulation of the experimental data). Hence, the x coordinate is defined along the wind tunnel surface from the ramp corner, with positive values in the downstream direction. On the other hand, the y coordinate is defined from each point of the wall of the wind tunnel, with its direction normal to that surface.

For the selected case, the data base [6] include mean surface pressure and skin friction distributions (Figure 22), as well as a series of mean fluid properties profiles at several locations (Figures 23 and 24). Additionally, constant-temperature hot-wire anemometers were used to make surveys of fluctuating data including mass-flux fluctuation and Reynolds shear-stress profiles at several locations. Moreover, data base [7] added the freestream flow conditions and error bounds for the case, as well as some minor corrections in the mean wall-pressure and skin friction coefficient distributions.

In order to perform computational simulations of the presented case, the computational domain defined in Figure 19 will be used. Thus, the entire upstream flat plate will be simulated to ensure that the incoming turbulent boundary layer is appropriately characterised. Nonetheless, since only the region in the vicinity of the ramp shoulder is intended to be properly described, just the lower part of the experimental facilities will be considered for the simulations, so that the overall computational cost can be partly reduced.

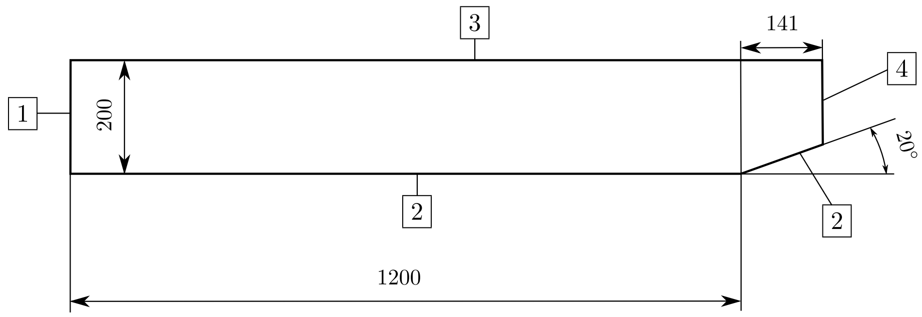

Figure 19: Test section computational domain and boundary conditions (indicated as subscripts). All non-indicated dimensions are expressed in millimetres.

Moreover, in the former figure, as well as the computational domain dimensions, a series of labels are included in order to indicate the boundary conditions that will be specified in the simulations. More information about these boundary conditions could be found at Table 2. Special emphasis should be made in the inlet boundary condition, which will be subsequently described.

3.2.1 Inlet boundary condition

As stated by Settles and Dodson [7], none of the experiments included in the selected database contains enough information to properly specify the boundary conditions of turbulent magnitudes. For this reason, assumptions must be made at the time of specifying these values, specially for the inlet boundary condition. To do this, one possibility was the one carried out by Morrison et al. [42], where flat plate computations were compared in order to obtain a profile whose boundary layer (δ), displacement (δ^*) and momentum (θ) thicknesses, and skin friction coefficient were within a 15% of the experimentally-determined values; finally introducing the former profile as inlet for the subsequent simulations.

In the present case, a very similar approach to the one performed by Morrison et al. will be used. Therefore, a three-meter flat plate has been simulated, taking the computational domain presented in Figure 20. Again, as stated by the subscripts, more information about the boundary conditions that have been specified in the simulations could be found at Table 3. Once the solution was computed, the boundary layer thicknesses (δ, δ^* and θ) as well as the non-perturbed fluid magnitudes (u_∞, p_∞ and T_∞) have been obtained at each longitudinal location of the plate, taking special attention on the former parameters (Figure 21).

Additionally, it should be noted that the boundary layer thicknesses cannot be directly calculated in Ansys Fluent. Therefore, to estimate these parameters, both the velocity and density profiles at each location have been exported from Ansys to Octave in order to estimate δ, δ^* and θ numerically. More details about this procedure could be found at Appendix A.

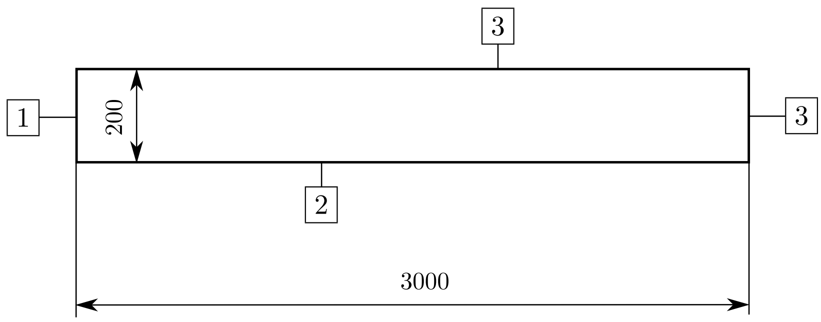

Figure 20: Not scaled schematic of the flat plate computational domain and boundary conditions (indicated as subscripts). All non-indicated dimensions are expressed in millimetres.

Once all the presented parameters were calculated at each location of the flat plate, the values have been compared with the experimental upstream conditions presented by Settles and Dodson [7] to obtain a profile where all the magnitudes were within a 10% of the experimental measurements. Once this location has been obtained, the x velocity, temperature, pressure and turbulent magnitude(s) profiles were exported, so that they could be specified as inlet conditions in the test section's simulations to correctly characterise the incoming boundary layer.

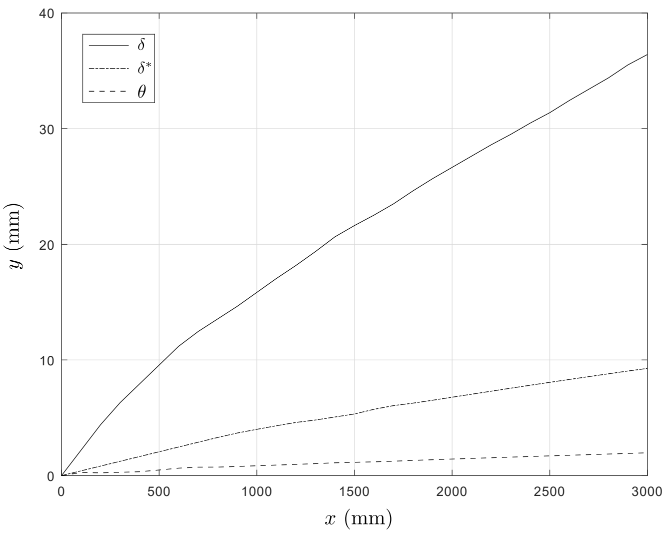

Figure 21: Boundary layer (δ), displacement (δ^*) and momentum (θ) thicknesses distribution over the simulated flat plate using the Spalart-Allmaras turbulence model.

To end with, it should be outlined that this procedure has been done twice, using both Spalart-Allmaras and $k-\varepsilon$ turbulence models. This approach needed to be taken to properly specify the inlet boundary conditions where Spalart-Allmaras, and $k-\varepsilon$ and $k-\omega$ turbulence models will be used respectively; since there are not direct relationship between $\widetilde{\nu_t}$, and k, ε and ω.

The characteristics of the selected profiles using both approaches could be found at Table 1. As it could be observed, all the parameters have less than a 10% of error in comparison with the experimental values, accomplishing with the established goal.

Table 1: Comparison between experimental and computed inlet profiles.

Magnitude	Experimental profile	Computed profile (S-A)		Computed profile ($k-\varepsilon$)	
		Computed value	Error (%)	Computed value	Error (%)
δ (mm)	25.000	25.100	0.40	23.123	7.51
δ^* (mm)	6.600	6.389	3.20	6.781	2.74
θ (mm)	1.300	1.346	3.55	1.410	8.46
u_∞ (m/s)	562.00	561.34	0.12	561.20	0.14
p_∞ (Pa)	$2.320 \cdot 10^4$	$2.334 \cdot 10^4$	0.60	$2.335 \cdot 10^4$	0.86
T_∞ (K)	98.30	98.76	0.47	98.78	0.49

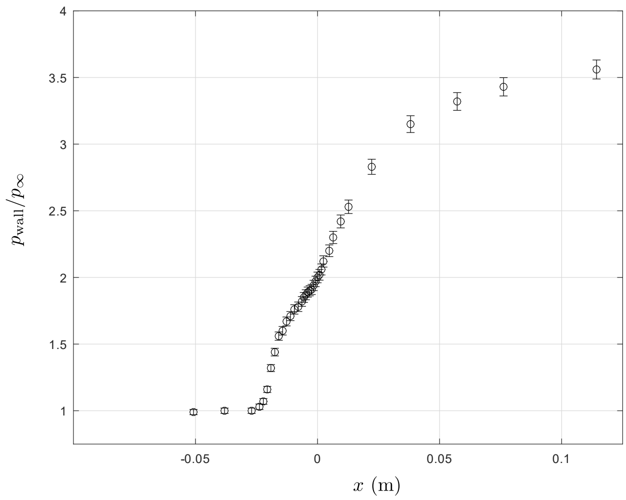

(a) Mean wall pressure distribution, $p_\infty = 2.32 \cdot 10^4$ Pa.

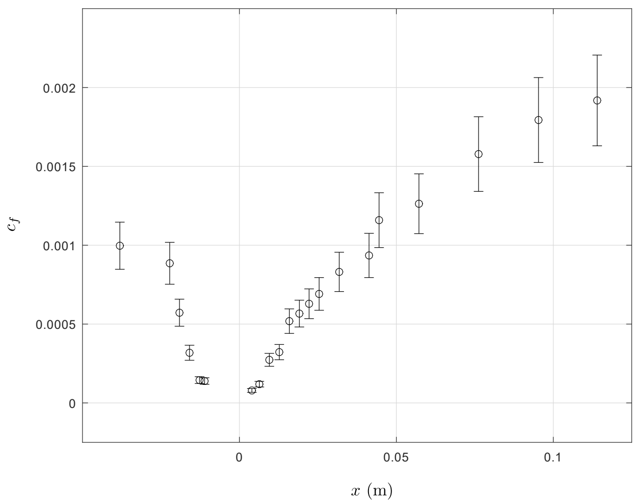

(b) Mean skin friction coefficient distribution.

Figure 22: Mean wall pressure and skin friction coefficient distributions over a 20° compression corner, for an incoming airflow with M= 2.85. Data extracted from Settles et al. [6, 7].

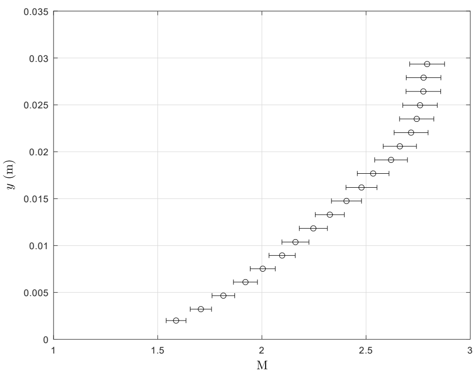

(a) $x = -0.0508$ m

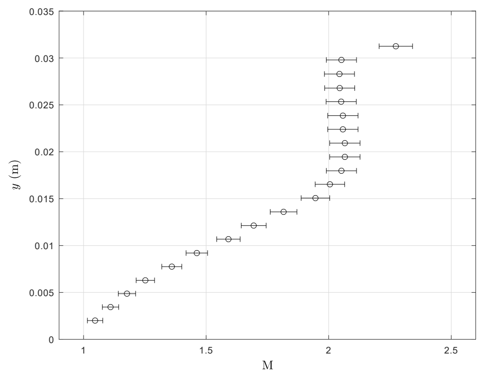

(b) $x = 0.0762$ m

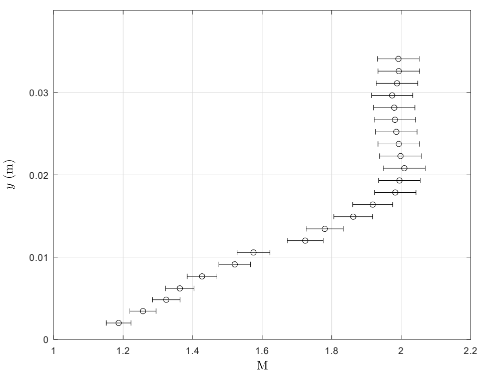

(c) $x = 0.0952$ m

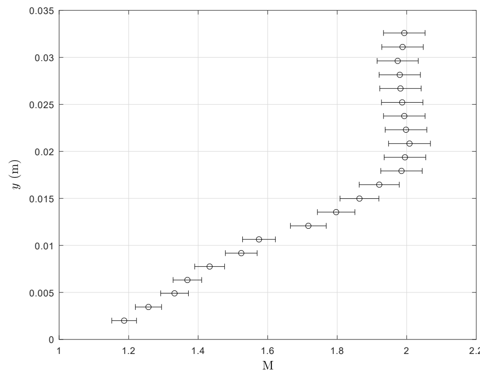

(d) $x = 0.1143$ m

Figure 23: Mean Mach number profiles at different locations. 20° compression corner, for an incoming airflow with M= 2.85. Data extracted from Settles et al. [6, 7].

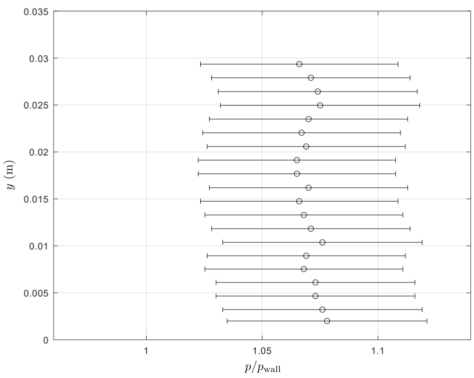

(a) $x = -0.0508$ m, $p_{\mathrm{wall}} = 0.2174 \cdot 10^5$ Pa

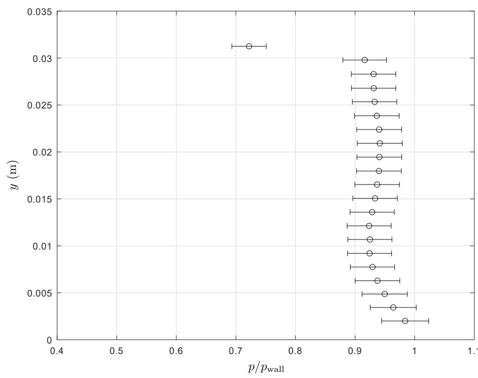

(b) $x = 0.0762$ m, $p_{\mathrm{wall}} = 0.7715 \cdot 10^5$ Pa

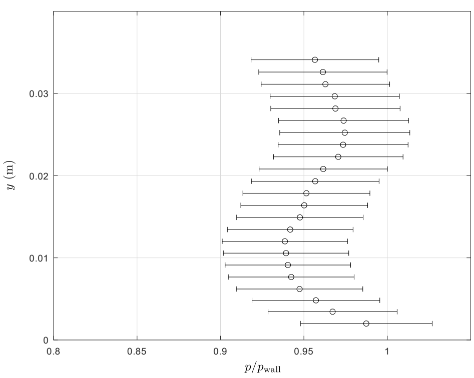

(c) $x = 0.0952$ m, $p_{\mathrm{wall}} = 0.7874 \cdot 10^5$ Pa

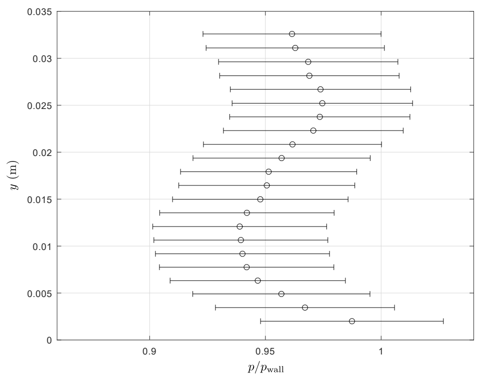

(d) $x = 0.1143$ m, $p_{\mathrm{wall}} = 0.8032 \cdot 10^5$ Pa

Figure 24: Mean pressure profiles at different locations. 20° compression corner, for an incoming airflow with M= 2.85. Data extracted from Settles et al. [6, 7].

Table 2: Test section boundary conditions.

Subscript	Nomenclature	Description
1	Inlet	Velocity-Inlet boundary condition, with: - Specified x velocity profile - x axis flow direction - Specified pressure profile - Specified temperature profile - Specified turbulent magnitude(s) profile(s)
2	Walls	Stationary wall condition, with: - No-slip condition - Adiabatic wall condition
3	Top	Pressure far field boundary condition, with: - M = 2.85 - x axis flow direction - $p = 2.32 \cdot 10^4$ Pa - $T = 98.3$ K - $D_h = 0.2032$ m, $I = 0\%$
4	Outlet	Pressure outlet boundary condition, with: - Non-reflecting behaviour - $-x$ axis backflow direction - Extrapolation of the fluid properties from the interior of the domain

Table 3: Flat plate boundary conditions.

Subscript	Nomenclature	Description
1	Inlet	Velocity-Inlet boundary condition, with: - $u_\infty = 563.25$ m/s - x axis flow direction - $p_\infty = 2.21 \cdot 10^4$ Pa - $T_\infty = 97.25$ K - $D_h = 0.2032$ m, $I = 1.25\%$
2	Wall	Stationary wall condition, with: - No-slip condition - Adiabatic wall condition
3	Outlets	Pressure far field boundary condition, with: - M = 2.85 - x axis flow direction - $p = 2.32 \cdot 10^4$ Pa - $T = 98.3$ K - $D_h = 0.2032$ m, $I = 0\%$

3.3 Grid generation

Grid generation comprises the spatial discretization of the computational domain, which significantly determines the accuracy, convergence and stability of the subsequent numerical analysis. Thus, this process represents one of the most critical steps during a computational fluid dynamics study. Moreover, this step is the source of the mesh-induced discretization errors, which can represent a significant part of the overall numerical error in regions involving large property gradients where the details of the flow may not be sufficiently captured.

For the case to be studied, due to the topology of the defined test section's computational domain (Figure 19), structured meshes based on hexaedral cells organised into rows and columns will be used. Moreover, the cells have been positioned to intend the majority of the fluxes to enter through one face of the cell, at the same time of ensuring that the boundary layers are properly characterised (Figure 25). This approach allows to reduce memory requirements and computational time in comparison with other types of meshes, as well as presenting a better convergence behaviour.

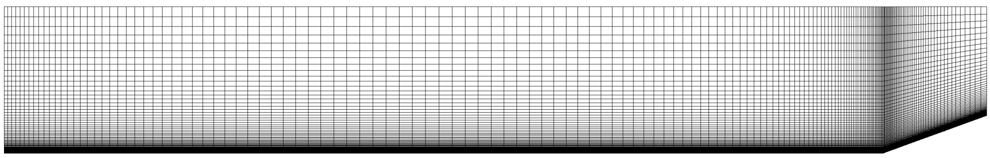

Figure 25: Generated coarse grid (test section).

Nonetheless, it should be outlined that these meshes are very difficult to be generated for complex geometries, where both hybrid and unstructured grids are normally used. These types of meshes are characterised not only by their high flexibility to be adapted to complicated topologies, but also by the reduction of man-hour requirements for their creation. On the other hand, it should be noted that the use of these kinds of grids often derive into higher memory requirements and slower simulations.

In order to properly characterise the flow field within the boundary layer, the generated meshes have been refined upon the upstream flat plate and ramp surfaces so that the first cells are contained in the viscous sub-layer (in particular, spacing constraints have been set so that the first cell centroids are located in $y^+ \simeq 1$). After placing these first cells upon the walls, 24 additional layers with growth rate 1.1 have been established in order to properly capture the steep gradients within the boundary layer. Finally, the position of the rest of the vertical layers has been defined with an hyperbolic tangent distribution.

Table 4: Details of the generated grids (test section).

Mesh	Cell count (-)	Minimum element size near the wall (m)	Minimum element size at the leading edge (m)	Minimum element size at the flat plate-ramp junction (m)
Coarse	21452	$2.5 \cdot 10^{-6}$	$5 \cdot 10^{-3}$	$1 \cdot 10^{-3}$
Medium	43152	$2.5 \cdot 10^{-6}$	$2.5 \cdot 10^{-3}$	$5 \cdot 10^{-4}$
Fine	90387	$2.5 \cdot 10^{-6}$	$1.25 \cdot 10^{-3}$	$2.5 \cdot 10^{-4}$
Very fine	182527	$2.5 \cdot 10^{-6}$	$6.25 \cdot 10^{-4}$	$1.25 \cdot 10^{-4}$

Another considered alternative, which is very common for industrial applications, was the usage of wall functions, placing the first cell within the log-law region of the boundary layer. This approach, which can reduce the overall cell count and consequently the simulation time, was rejected since the boundary layer was intended to be resolved directly instead of using a model (given the importance of the characterization of the boundary layer for the studied problem).

Hence, to perform a grid convergence study, the presented grid characteristics have been applied to generate four different meshes, whose main details can be found in Table 4. Thus, the density of cells in each mesh has been modified so that the cell count is approximately twice as the preceding coarser grid. Some of these meshes will be also used for the turbulence model assessment and the adaptive mesh refinement study, as it will be specified in future sections.

Apart from the previously described boundary layer refinement, additional streamwise constraints have been established on both the leading edge of the flat plate and the origin of the ramp using hyperbolic tangent distributions, in order to capture the gradients that may appear in those regions.

Moreover, additional parameters of the generated grids should be considered in order to assess their quality (Table 5). In the current document, special emphasis will be made on aspect ratio and skewness. On one hand, aspect ratio is defined as the relationship between the largest and the shortest cell side. On the other hand, skewness is a measure of the suitability of the created cells regarding their angles. Specifically, the equiangular skew definition will be used in the studied case.

Table 5: Quality parameters of the generated grids (test section).

Mesh	Cell Count (-)	Max. Skewness (-)	Mean Skewness (-)	Max. Aspect Ratio (-)
Coarse	21452	0.222	0.055	7227.9
Medium	43152	0.222	0.061	5675.8
Fine	90387	0.222	0.063	4324.6
Very fine	182527	0.222	0.065	3663.0

Regarding the obtained results, the values of skewness are adequate, according to the criteria presented by the Ansys Fluent User's Guide [43], which recommends a maximum value of 0.7 for structured grids. On the other hand, a relatively high maximum aspect ratio is found for the four meshes, which is associated to the cells close to the wall (regarding the boundary layer refinement that has been carried out). Nonetheless, these values are typical for these kinds of meshes, which intend to accurately capture the gradients within the boundary layer in high-speed flows. To end with, it should be noted that these aspect ratios do not generally derive into stability problems, but they can lead to slower convergence of the simulations. Additionally, these parameters do not represent a problem since the cells close to the walls have been aligned with the direction of the flow throughout these regions.

Finally, it should be outlined that, for the simulation of the flat plate used for the determination of the inlet boundary condition of the test section, a similar structured mesh has been generated (Figure 26). Initially, this grid comprised the same normal-to-wall cell distribution of the test section's coarse grid, and 301 equispaced nodes in the streamwise direction. Nonetheless, to properly characterise the initial part of the flat plate, the minimum element size near the wall was changed to $1.5 \cdot 10^{-6}$ meters and a streamwise spacing constraint of $5 \cdot 10^{-3}$ meters was imposed on the leading edge using a hyperbolic tangent distribution.

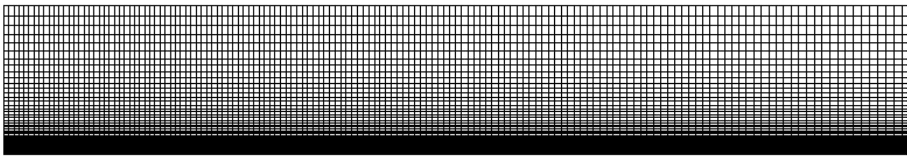

Figure 26: Detail of the beginning of the generated grid for the flat plate used for the definition of the inlet boundary condition of the test section.

3.4 Solver parameters

In order to solve the previously presented governing equations, Ansys Fluent uses a finite volume method. This method is based on the integration of the former equations on the control volumes defined by each of the computational grid cells.

Due to the coupling and non-linearity of the governing equations, the numerical procedure must be repeated several times until a converged solution for the fluid properties at each computational point is obtained. In every repetition, the solution of the former iteration is taking as the initial point. In this section, the software set up used in the numerical study will be described. For consistency, these parameters will be repeated for each of the simulations. Solver parameters:

- Two-dimensional (planar) steady-state, density-based solver with implicit formulation. Two-dimensionality is given by the chosen experimental data to validate the numerical results. Additionally, since the transient behaviour of the flow is not relevant for the analysis, steady-state formulation will be used in order to reduce the overall computational cost of the simulations.

  Moreover, density-based solvers first obtain the velocity and density fields from the momentum and continuity equations respectively, whereas the pressure and temperature fields are then determined from the equation of state and the energy equation. Due to the high-speed and compressible nature of the flow to be studied, this procedure has been selected according to the Ansys Fluent User's Guide [43].

  On the other hand, implicit formulation is based on the expression of the unknown fluid properties in a cell using relations that include both known and unknown values from neighbouring cells. This results in a coupling which imposes the resulting set of equations to be resolved at the same time. In particular, the Incomplete Lower Upper (ILU) factorization scheme will be used in conjunction with the algebraic multigrid (AMG) method to achieve this task. Again, this formulation has been selected as recommended by the Ansys Fluent User's Guide [43] for the intended flow to be resolved.

- Energy equation included in the set of equations to be solved, and proper turbulence model chosen for each simulation.

- Working fluid set as air with ideal gas behaviour, and:
  - Constant molecular weight 28,966 kg/kmol
  - Constant specific heat at constant pressure (c_p) 1002 J/(kg K)
  - Constant thermal conductivity 0,00925 W/(m K)
  - Sutherland's viscosity law, with $C_1 = 1.458 \cdot 10^{-6}$ kg/(m s K$^{1/2}$), and $S = 110,4$ K
  - Constant Prandtl number $\mathrm{Pr} = 0.72$
  - Constant turbulent Prandtl number $\mathrm{Pr}_t = 0.9$

- Operating pressure set to 0 Pa. That is, no pressure will be taken as a reference during the simulations (i.e. the solver will directly work with the static pressure), since there are significant pressure variations throughout the domain. Nonetheless, it should be noted that the usage of an operating pressure is common within the simulation of incompressible flows, where its lack could derive into significant round-off errors.

- Discretization methods. Once the governing equations are integrated in each of the computational cells, discretization schemes need to be used in order to express the resultant set of equations in terms of the fluid properties at the cell centroids. For this purpose, the following schemes will be used:
  - Second order central differencing scheme, employed for the diffusion terms (standard configuration in Ansys Fluent).

– Second order upwind scheme, for both the discretization of the terms associated to convection and turbulence. This type of formulation enhances the overall stability of the solver as well as providing second order accuracy.

  Another alternative that was initially considered was the third-order MUSCL scheme, which blends central differencing and upwind second order schemes. This alternative was rejected as recommended by the Ansys Fluent User's Guide [43], as a result of not including any gradient limiter, which allows to accurately characterize flows involving large gradient regions (e.g. shock waves).

– Least squares cell based scheme, which assumes the flow properties to vary linearly between cell centroids. Used for the discretization of terms involving gradients.

– Roe Flux-Difference Splitting (FDS) scheme, used for the discretization of the additional inviscid flux vectors that appear as a result of the selected density-based solver.

- Simulation control parameters:
  – $p_{\text{min}} = 1000$ Pa
  – $p_{\text{max}} = 150000$ Pa
  – $T_{\text{min}} = 50$ K
  – $T_{\text{max}} = 5000$ K
  – Default turbulent-magnitudes limiters.
  – Positivity rate limit set to 0.01
  – Turbulent magnitudes underrelaxation schemes set to 0.8. As stated by [43], these values can improve the convergence to steady-state when implicit formulation is used.
- Residual monitors set to $1 \cdot 10^{-4}$, which is assumed to be a good indicator of the convergence of the solution given the compressible nature of the flow that is intended to be simulated, as well as the complex shock wave system that is intended to be captured. Moreover, the same criterion was used in the similar study carried out by Forster [25].

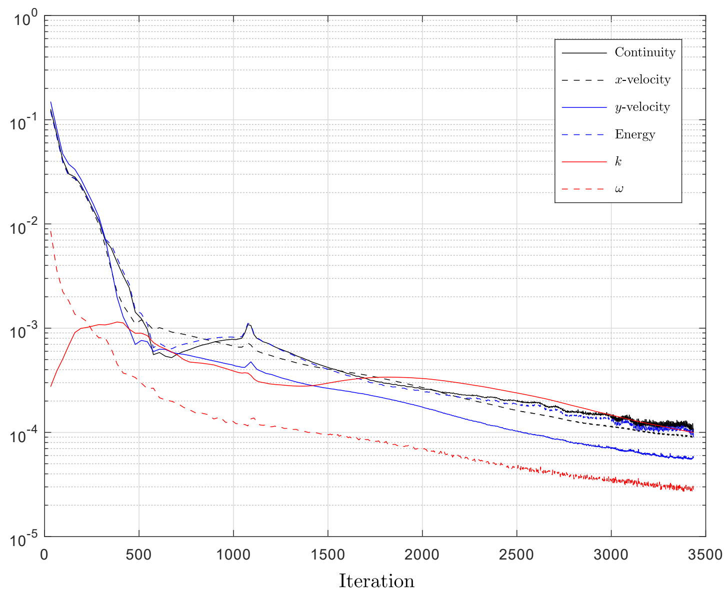

Figure 27: Evolution of the residuals at each iteration of the solver (standard k−ω SST, coarse grid).

Additionally, both the mass flow rate through the outlet section and the drag force on the wall have been monitored to assess the convergence of the solution. Thus, it has been imposed that, apart from accomplishing with the residual's criteria previously mentioned, to obtain a converged solution, these two magnitudes should not have changes of more than a 0.1% between iterations.

- Initial conditions set to uniform fields of fluid properties, with:
  - $p = 2 \cdot 10^4$ Pa
  - $u = 562$ m/s, $v = 0$ m/s
  - $T = 98.3$ K
  - Turbulence magnitudes set to their averaged values within the boundary layer ($\widetilde{\nu_t} = 0.015$ m^2/s for the Spalart-Allmaras simulations, and $k = 100$ m^2/s^2 and $\varepsilon = 3000$ m^2/s^3 for the rest of studied turbulence models)[7].

[7] With the exception of the flat plate simulations, where all the turbulence magnitudes were initially set to zero.

3.5 Adaptive mesh refinement

Adaptive mesh refinement methods intend to maximise the increase of numerical accuracy per computational cost between mesh changes by driving automatically error-based refinement and unrefinement. These widely extended techniques in computational fluid dynamics have proved to reduce CPU time, memory and man-hour requirements in comparison with classical refinement methods. In particular, for some problems, the savings in computational requirements exceed a factor of 100, allowing the simulation of previously intractable problems [44].

In these methods, locally mesh changes are performed in cells previously marked with some error-based criteria, allowing to reduce mesh-induced discretization errors while avoiding the inclusion of unnecessary cells. According to Jasak [45], the standard adaptive mesh refinement procedure consists in the following steps:

1. An initial coarse computational grid is created, that needs to be fine enough to describe the main flow features.
2. The governing equations are solved in the available mesh through a finite volume method.
3. From the available solution and the mesh characteristics, the numerical error is estimated based on some criteria.
4. If the intended level of accuracy is reached (based on the estimation of the numerical error previously done), the solution is accepted and the procedure finishes. If not, the procedure continues with the following steps.
5. The previously estimated errors are used to define a criteria of refinement (high error regions) and unrefinement (low error regions), identifying the set of cells within the computational domain to be refined/coarsen.
6. The initial grid is modified according to the criteria defined in the former step through a refinement and unrefinement algorithm.
7. Finally, the existing numerical solution is mapped into the modified mesh and used as an initial guess for the new calculation.

Thus, steps 2 to 7 are repeated until the desired level of accuracy is reached. A flow chart describing the presented procedure can be found in Figure 28. One of the biggest issues to be resolved for the implementation of these techniques is how to properly define a numerical error indicator. For this purpose, a large number of criteria could be used including variations of key magnitudes within elements, entropy levels, residuals... Nonetheless, according to Löhner [44], the most commonly used error indicators are:

- Differences between fluid properties. Being the simplest error indicator, it measures the error through the absolute difference between elements of some indicator variable (e.g. Mach number, density or entropy). Widely used for industrial applications.
- Gradients of fluid properties. In this approach, the gradients of fluid properties are used to evaluate the numerical error throughout the computational domain. Very extended for engineering applications.
- Higher-order derivatives of fluid properties. In this case, instead of evaluating the first-order derivatives (i.e. gradients), the numerical error is estimated through higher order derivatives. Not recommended for flows including regions with large property gradients.
- Output-based error estimators. In this approach, the numerical error is estimated through some output parameter which the user specifies. As an example, in the simulation of the flow over an airfoil, lift and drag coefficients could be used as output-based error estimators. This method has received increased attention in the last years.

It should be outlined that none of the presented error criteria are dimensionless. Thus, in flows involving large gradients or property jumps (such as shock waves), these regions would be the only considered for refinement in detriment of the rest of the flow features. To avoid this situation, stopping criteria or normalization of the error indicators should be introduced in flows with such characteristics [45].

In particular, Ansys Fluent allows to evaluate the numerical errors within the obtained solution through multiple criteria including derivatives of fluid properties, cell volumes, distance to boundaries... which can be then combined in order to create sophisticated criteria [43]. In the numerical study that will be performed, the 'gradient adaptation' option implemented in the software will be used.

This tool enables to select the cells to be coarsen/refined through user-specified thresholds of the values, gradients and curvatures of desired fluid magnitudes. To specify these thresholds, the scale normalisation option[8] will be used to obtain a better control of the refinement/coarsening process. Therefore, different alternatives for the definition of these error estimators will be compared in order to assess which of the presented options better performs for the studied case.

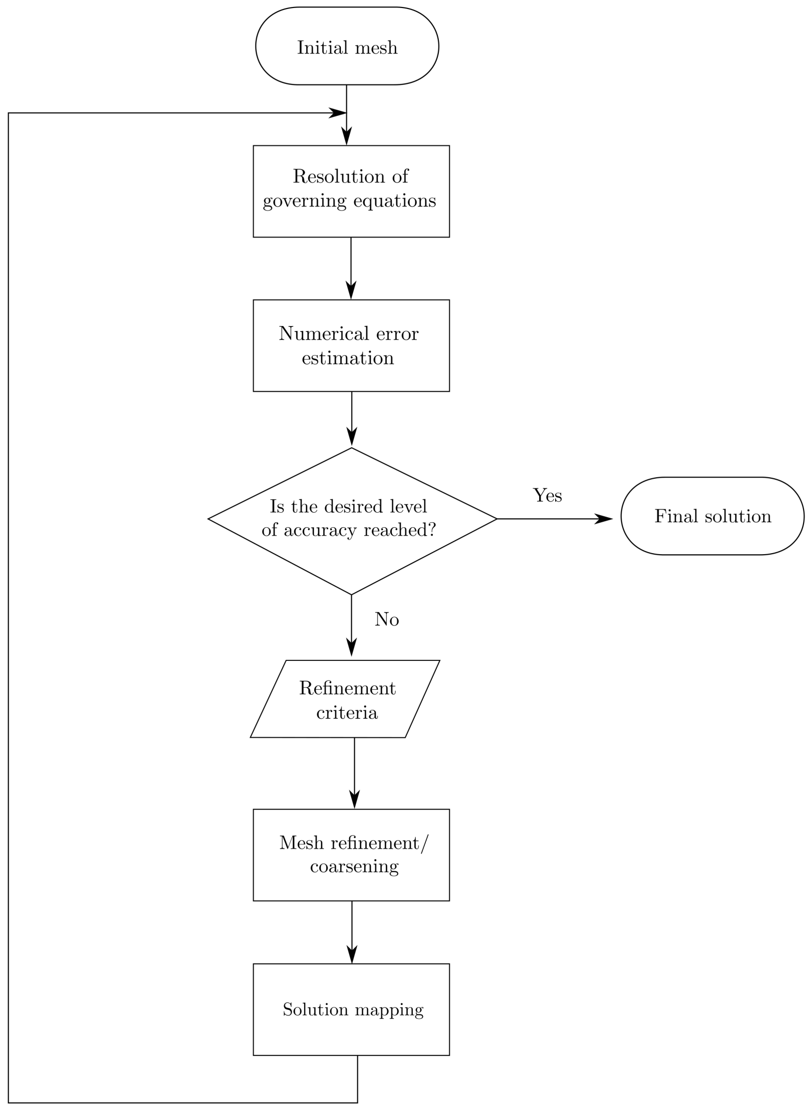

Figure 28: Flow chart of the presented adaptive mesh refinement procedure.

Moreover, this error estimation (and consequently the overall adaptive mesh refinement procedure) will be performed once the solution of the initial grid has converged (according to the convergence criteria introduced in the former section). Nonetheless, the tool enables an option to 'dynamically' adapt the mesh after a certain number of iterations of the solver, which has been rejected to follow the standard procedure presented by Jasak [45].

[8] This option normalises the thresholds by the mean value of the desired error estimator throughout the entire computational domain.

On the other hand, once the numerical errors within the obtained solution have been estimated and the cells to be coarsen/refined have been identified, an algorithm to modify the mesh topology is required. For this issue, several types of algorithms have been developed in the recent years, being the most outlining ones the so called mesh movement or repositioning methods (r-methods), and the mesh enrichment methods (h/p-methods).

According to [44], the most extended algorithm in computational fluid dynamics is the h-enrichment method. This approach is based on the subdivision and merging of cells to conduct the refinement and coarsening procedures respectively. Specifically, in order to perform adaptive mesh refinement, Ansys Fluent implements an algorithm using this approach, with the particularity that the tool cannot coarsen cells from the original grid that was loaded to the software.

4 Results

In this section, the results from the performed numerical analysis will be presented. In particular, the numerical study has been divided into three different parts. First of all, a grid convergence study will be performed using one of the presented turbulence models. Secondly, a turbulence model assessment will be conducted in order to compare the presented turbulence models, so the most adequate one can be selected to perform the final part of the study. This final part will comprise the analysis between different adaptive mesh refinement configurations, so that the possible benefits from the usage of these techniques in flows involving shock wave/boundary layer interactions could be assessed.

4.1 Grid convergence study

To start with the numerical analysis, a grid convergence study will be performed using the four generated grids previously presented, so that the most appropriate grid resolution to resolve the flow could be identified. Thus, the flow over the four grids will be simulated using the $k - \omega$ SST turbulence model (which has been selected since it is known to perform generally well where adverse pressure gradients are present) and the solver parameters introduced in Section 3.4, finally obtaining the performance parameters presented in Table 6. It should be reminded that the model used during this section will be compared during Section 4.2 against the other ones previously presented, in order to obtain the most appropriate one for the simulation of the studied flow.

Table 6: Performance parameters of the generated solutions (grid convergence study, standard $k - \omega$ SST).

Mesh	Cell Count (-)	CPU time (s)	Mean y^+ (-)	Min. y^+ (-)	Max. y^+ (-)
Coarse	21452	659.1	0.57	0.12	1.07
Medium	43152	1857.7	0.57	0.08	1.09
Fine	90387	3902.7	0.61	0.08	1.16
Very fine	182527	9900.0	0.61	0.07	1.18

Firstly, it should be noted that the computational time required for the simulation is increased as the cell count increases. On the other hand, the y^+ remains in general under 1 within all the four meshes, which indicates that the boundary layer has been correctly characterised.

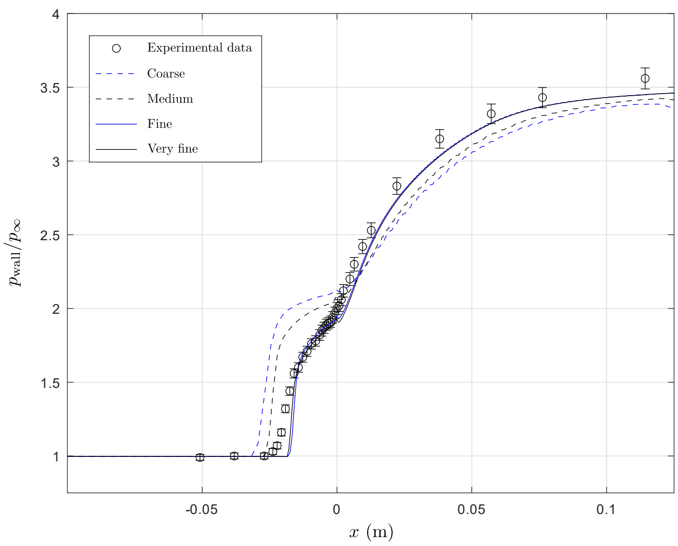

Figure 29: Mean pressure distribution over the wall of the computational domain (grid convergence study, standard $k - \omega$ SST). Experimental data extracted from Settles et al. [6,7].

Nonetheless, it should be noted that in the downstream part of the interaction, the y^+ values in the four grids are slightly higher than this threshold value (see maximum y^+ in Table 6). However, considering that the flow intended to be accurately characterised is located in the vicinity of the ramp junction and that these peaks are substantially far from the threshold value of the viscous sub-layer ($y^+ = 5$), the y^+ distribution over the four grids can be accepted as reasonable.

Once the simulations have been computed, a series of fluid magnitudes can be obtained from the four solutions in order to compare the results with the experimental data. First of all, a comparison between the computed and experimental values of the mean wall pressure distribution has been generated (Figure 29).

As it could be observed, as the grid is refined, the obtained results are closer to the experiment data, finally obtaining the desired grid independence between the 'fine' and 'very fine' results. Additionally, in these two solutions the mean pressure distribution is nearly identical to the experimental one falling under the experimental uncertainty for all the domain but the upstream region of the interaction. This last issue could be justified appealing to the behaviour associated to the turbulence model used for the simulations ($k-\omega$ SST).

To continue with, a comparison between the experimental and computed values of the module of the mean skin friction coefficient could be also obtained (Figure 30). With this magnitude, the extent of the separation bubble could be observed by accounting the places where the skin friction reaches a zero value.

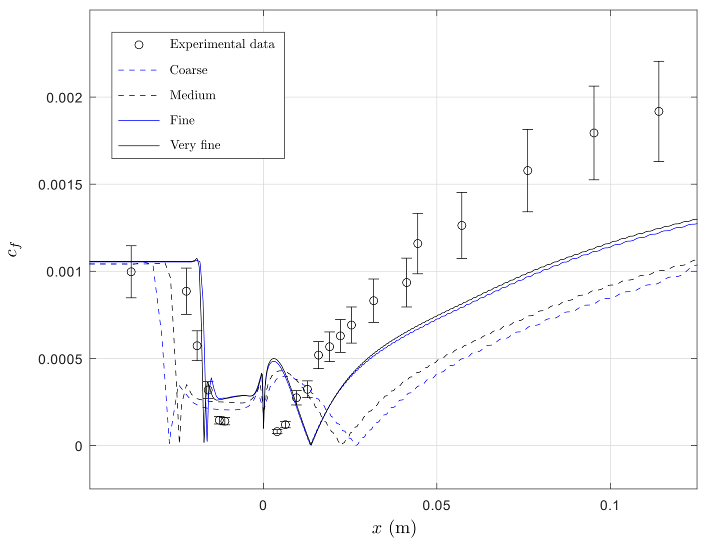

Figure 30: Mean skin friction coefficient (module) distribution over the wall of the computational domain (grid convergence study, standard $k-\omega$ SST). Experimental data extracted from Settles et al. [6, 7].

Here again, the grid independence is obtained between the 'fine' and 'very fine' solutions, being the differences between the two latter solutions negligible. It should be also outlined that in all the cases, the skin friction coefficient in the downstream part of the interaction is significantly underestimated, which can be justified appealing to the turbulence model used for the simulations. Additionally, it should be noted that in the four cases the extent of the separation region is overestimated in comparison with the experimental data.

Nonetheless, this overestimation is reduced as the grid is refined, reducing the overall error. This fact could be numerically assessed plotting not only the skin friction coefficient module, but its x component (Figure 31). Thus, this x component of the wall shear stress allows to numerically compute the extent of the separation bubble on the three cases in order to quantitatively compare the obtained solutions.

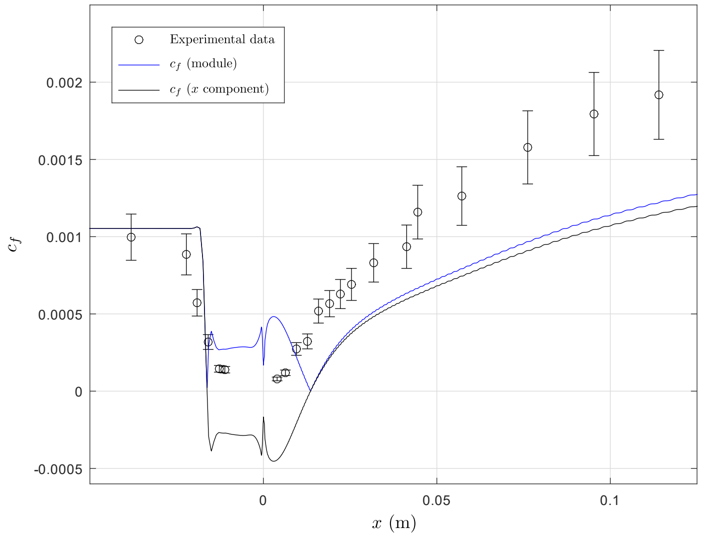

Figure 31: Mean skin friction coefficient (module and x component) over the wall of the computational domain (standard $k-\omega$ SST, fine grid). Experimental data extracted from Settles et al. [6, 7].

To follow with this comparison, two additional error parameters will be defined to assess how close are the obtained pressure and wall shear distributions to the experimental values. On one hand, to compare the obtained wall pressure distributions, an error parameter e_1 will be defined as:

$$e_1 = \sqrt{\sum_{i=1}^{n} \left((p_{\text{wall}}/p_\infty)_{\text{exp},\ i} - (p_{\text{wall}}/p_\infty)_{\text{computed},\ i} \right)^2} \tag{40}$$

Where each of the computed wall pressure values to be compared with the experimental values will be obtained numerically through linear interpolation. More details about this process could be found in Appendix B. In a similar way, to compare the skin friction coefficient distributions, an error parameter e_2 will be defined as:

$$e_2 = \sqrt{\sum_{i=1}^{n} \left((c_f)_{\text{exp},\ i} - (c_f)_{\text{computed},\ i} \right)^2} \tag{41}$$

Obtaining the computed c_f values numerically through linear interpolation as in the previous case. Hence, these two parameters, as well as the extent of the separated bubble, have been obtained for the four simulated cases (Table 7).

Table 7: Error parameters of the generated solutions (grid convergence study, standard $k-\omega$ SST).

Mesh	Cell Count (-)	CPU time (s)	l_{sep} (mm)	e_1 (-)	$e_2 \cdot 10^3$ (-)
Coarse	21452	659.1	53.50	2.065	2.552
Medium	43152	1857.7	46.71	1.470	2.408
Fine	90387	3902.7	29.85	0.715	1.751
Very fine	182527	9900.0	30.89	0.667	1.715

The observed contraction of the interaction as the grid is refined is now quantitatively characterised with the computed values of l_{sep}, also obtaining a converged value of this magnitude on both the 'fine' and 'very fine' solutions with a difference of less than a 5%.

On the other hand, as the mesh is refined, the pressure and skin friction coefficient overall error estimators are also reduced, following the behaviour previously introduced, finally obtaining a converged solution that falls very close to the available experimental data. Thus, these magnitudes have allowed to quantitatively justify the grid independence of the computed solutions, reinforcing the conclusions obtained from the presented figures.

With these conclusions, and taking the additional qualitatively comparisons given by the velocity and pressure profiles of Figures 34 and 35, the fine grid is assumed to provide sufficiently accurate results, and will be the one used in the turbulence model assessment. Moreover, the coarse grid solution will be taken as the starting point for the adaptive mesh refinement studies to be performed, as it is observed to properly characterise the main features of the flow field.

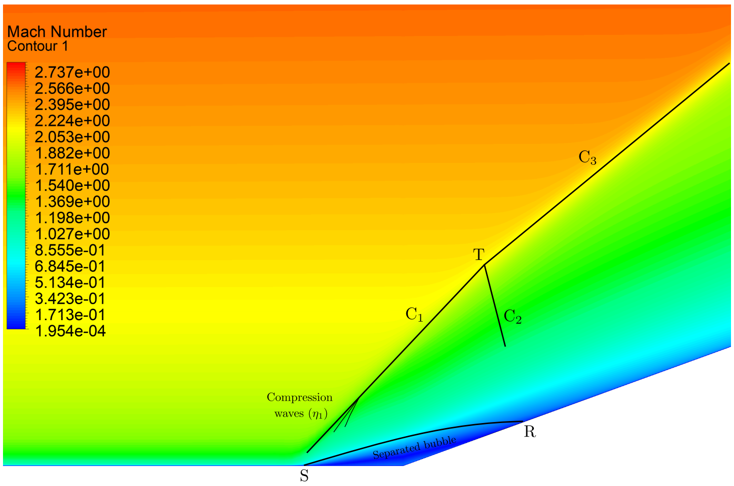

Figure 32: Mean Mach number contour in the vicinity of the ramp junction (fine grid, standard $k-\omega$ SST).

Finally, the fine grid solution could be used to obtain a mean Mach number contour in the vicinity of the ramp junction (Figure 32) and consequently compare the main flow features against the theoretical description given in Section 2.3 (Figure 16).

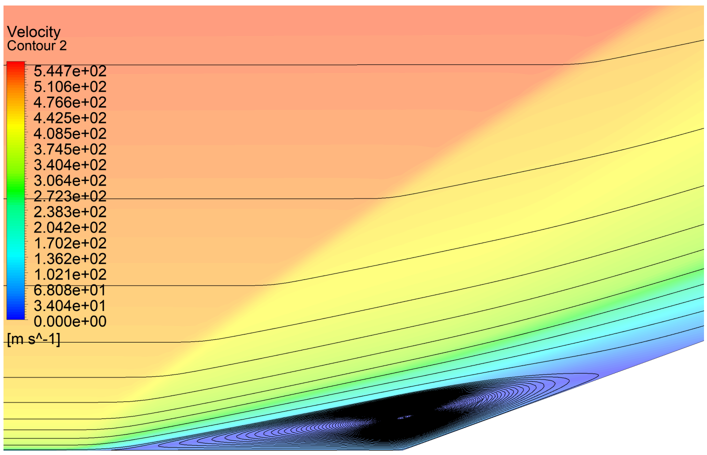

Figure 33: Mean velocity module contour in the vicinity of the ramp junction, and streamlines (fine grid, standard $k-\omega$ SST).

Hence, in the computed solution a series of compression waves (η_1) merge to form shock C_1 which at the same time joins reattachment shock C_2 (which in this case is very weak, causing a very slight deflection on the flow) at point T. At this point, shock C_3 (which corresponds to the purely inviscid solution far from the wall) is generated.

Thus, the presented flow features are very similar to the ones described on the schematic of the theoretical background, reinforcing the physical interpretation of the computed solution. The same flow features could be noticed in Figure 33, where the extent of the separation region could be better perceived by the plotted streamlines.

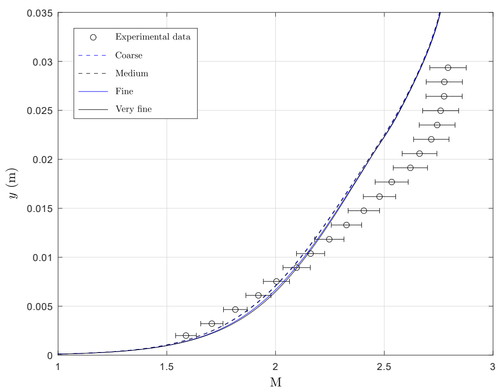

(a) $x = -0.0508$ m

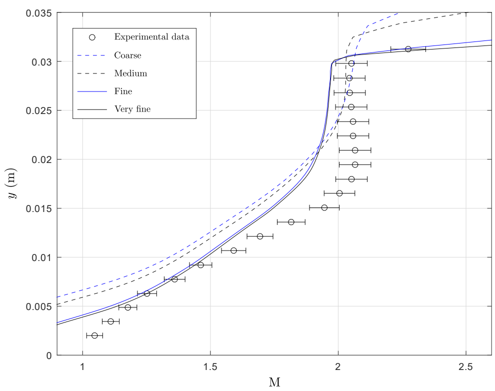

(b) $x = 0.0762$ m

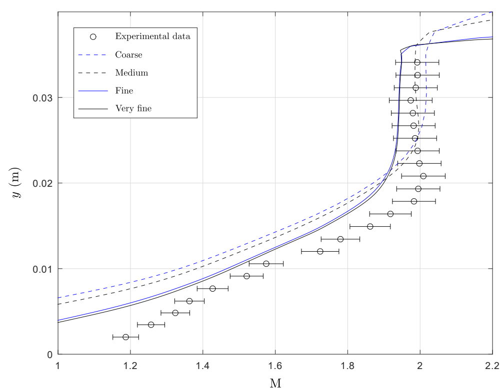

(c) $x = 0.0952$ m

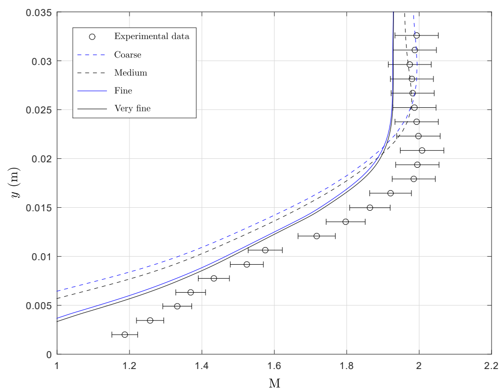

(d) $x = 0.1143$ m

Figure 34: Comparison between mean Mach number profiles at different locations (grid convergence study, standard $k-\omega$ SST). 20° compression corner, for an incoming airflow with M= 2.85. Experimental data extracted from Settles et al. [6, 7].

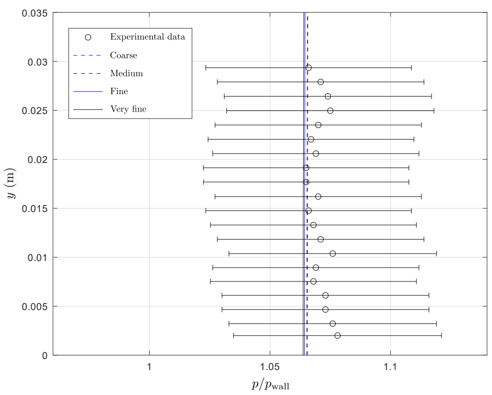

(a) $x = -0.0508$ m, $p_{\mathrm{wall}} = 0.2174 \cdot 10^5$ Pa

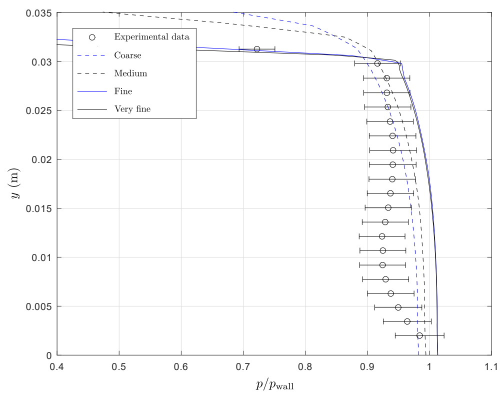

(b) $x = 0.0762$ m, $p_{\mathrm{wall}} = 0.7715 \cdot 10^5$ Pa

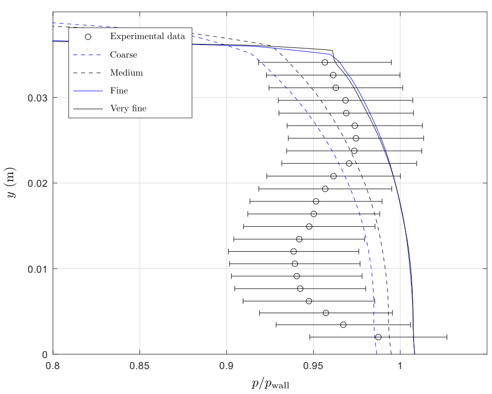

(c) $x = 0.0952$ m, $p_{\mathrm{wall}} = 0.7874 \cdot 10^5$ Pa

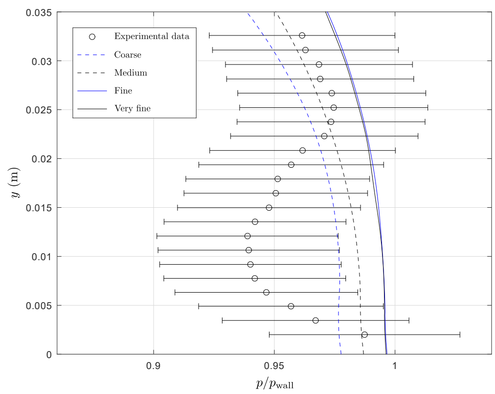

(d) $x = 0.1143$ m, $p_{\mathrm{wall}} = 0.8032 \cdot 10^5$ Pa

Figure 35: Comparison between mean pressure profiles at different locations (grid convergence study, standard $k - \omega$ SST). 20° compression corner, for an incoming airflow with M= 2.85. Experimental data extracted from Settles et al. [6, 7].

4.2 Turbulence model assessment

To follow with the numerical study, several turbulence models will be compared using the generated fine grid in order to obtain the most appropriate one to simulate the intended flow. For consistency, again the same solver parameters previously presented will be used in each of the performed simulations.

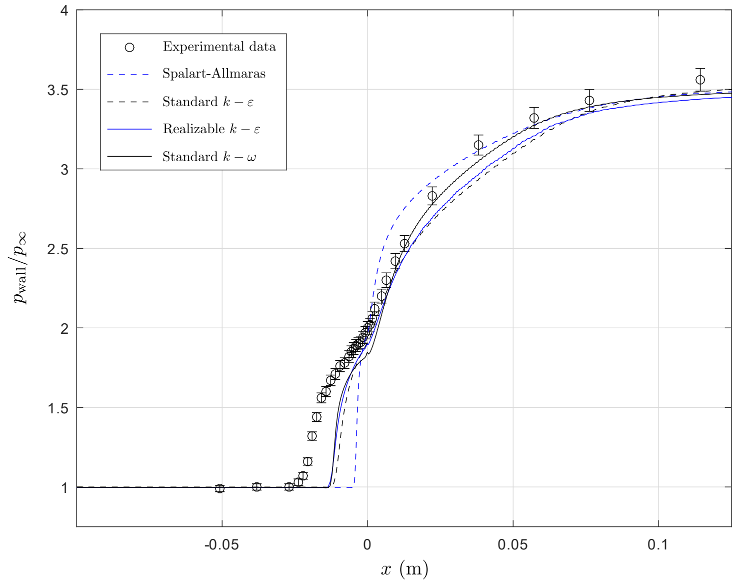

Figure 36: Comparison between mean pressure distributions over the wall of the computational domain using different turbulence models (I). Experimental data extracted from Settles et al. [6,7].

Hence, this turbulence model assessment will be divided into two parts. Firstly, the results from the Spalart-Allmaras model, standard and realizable $k-\varepsilon$ models, and the standard $k-\omega$ model will be compared.

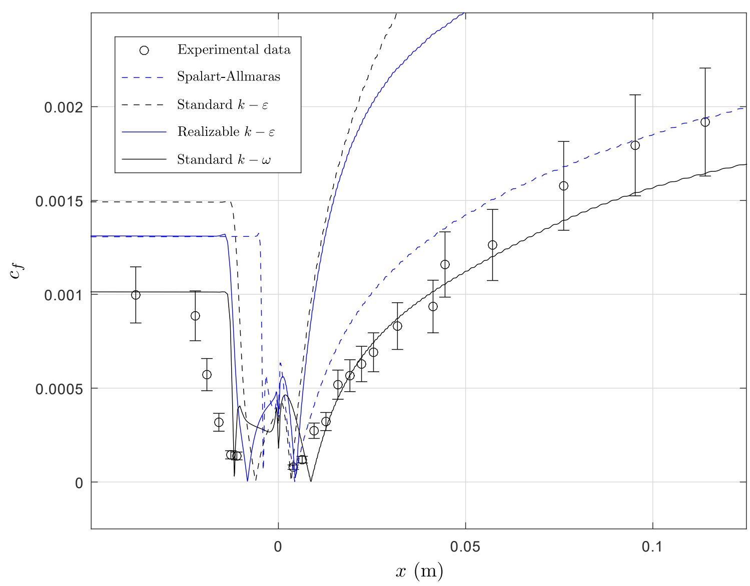

Figure 37: Comparison between mean skin friction coefficient (module) over the wall of the computational domain using different turbulence models (I). Experimental data extracted from Settles et al. [6,7].

Starting with the mean wall pressure distribution within the models (Figure 36), all models seem to partly underestimate the upstream influence of the interaction. Moreover, the downstream part of the interaction generally seems to be properly characterised according to the experimental data provided by Smits et al. [6, 7].

Particularizing for each of the studied turbulence models, both the realizable $k-\varepsilon$ and the standard $k-\omega$ show the best agreement with the experimental data. On one hand, the realizable $k-\varepsilon$ falls very close to the experimental values in the vicinity of the ramp junction whereas the pressure values downstream of the interaction are slightly underestimated.

On the other hand, the standard $k-\omega$ shows the opposite behaviour: the pressure on the vicinity of the ramp junction is partly underestimated whereas the downstream pressure is adequately characterised. Finally, it should be noted that the Spalart-Allmaras and the standard $k-\varepsilon$ show poorer agreements with the experimental distribution, which derive into larger errors in the estimation of both the upstream influence of the interaction and the downstream pressure distribution.

To follow with, the distributions of the module of the skin friction coefficient over the wall of the computational domain using the same turbulence models are presented in Figure 37. Regarding the presented data, it seems clear that both the standard and the realizable $k-\varepsilon$ models considerably overestimate the wall shear distribution, resulting in poor agreements with the experimental values.

Table 8: Error parameters of the solutions obtained using the compared turbulence models (I).

Turbulence model	CPU time (s)	l_{sep} (mm)	e_1 (-)	$e_2 \cdot 10^3$ (-)
Spalart-Allmaras	2027.2	8.37	2.483	2.297
Standard $k-\varepsilon$	2172.2	9.58	1.572	6.354
Realizable $k-\varepsilon$	2181.9	12.81	1.406	4.708
Standard $k-\omega$	2694.3	20.42	1.405	1.190

On the other side, the Spalart-Allmaras solution partly overestimates the skin friction coefficient throughout all the interaction, significantly underestimating at the same time the extent of the separation region. Finally, the standard $k-\omega$ distribution shows good agreement with the experimental data mostly matching the experimental extent of the separation bubble, with a slight overestimation of the downstream location of the reattachment point.

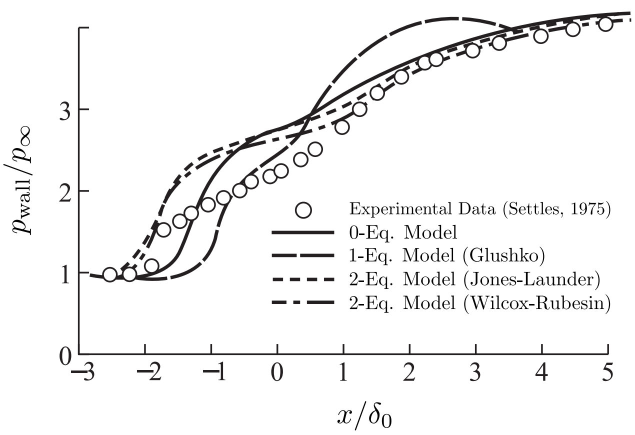

Figure 38: Comparison of wall pressure distributions of RANS computations for the flow over a 24° compression ramp with $\mathrm{M}_\infty = 2.8$, $\mathrm{Re}_{\delta_0} = 1.33 \cdot 10^6$, $T_{\text{wall}}/T_{wall,adiabatic} = 0.88$, using different turbulence models. Extracted from Viegas and Hortsman [9].

To quantitatively compare the obtained solutions, the same error parameters presented in the former section will be used (Table 8). Thus, as previously stated, although the realizable $k-\varepsilon$ seems to have less pressure global error, the standard $k-\omega$ model shows better agreement regarding the three studied parameters. Moreover, it should be noted that this latter model requires slightly more computational resources in comparison with the other studied models. The presented arguments could be also be reinforced appealing to the profiles of Figures 42 and 43, whose results follow the same tendencies.

The obtained conclusions are also supported by the calculations made by Viegas and Hortsman [9], where RANS computations over a 24° compression corner performed using zero-equation, one-equation (Glushko models) and two equation (Jones-Launder and Wilcox-Rubesin models) were compared. In particular, wall pressure distributions for the four models are presented in Figure 38. Thus, qualitative agreement with the experimental data is obtained for all the studied models, whereas likewise global quantitative agreement is found. However, it should be noted that, in general, an improvement in the overall agreement is obtained using higher-order turbulence models, as in the current study.

To continue with the comparison of turbulence models, the second part of the assessment will compare the results from the simulation of the standard $k-\omega$ (since it was the one that showed the best agreement with the experimental values from the former group of turbulence models), and both the standard and the Georgiadis and Yoder version of the $k-\omega$ SST[9]. Firstly, the wall pressure distributions within the models will be compared against the available experimental data (Figure 39).

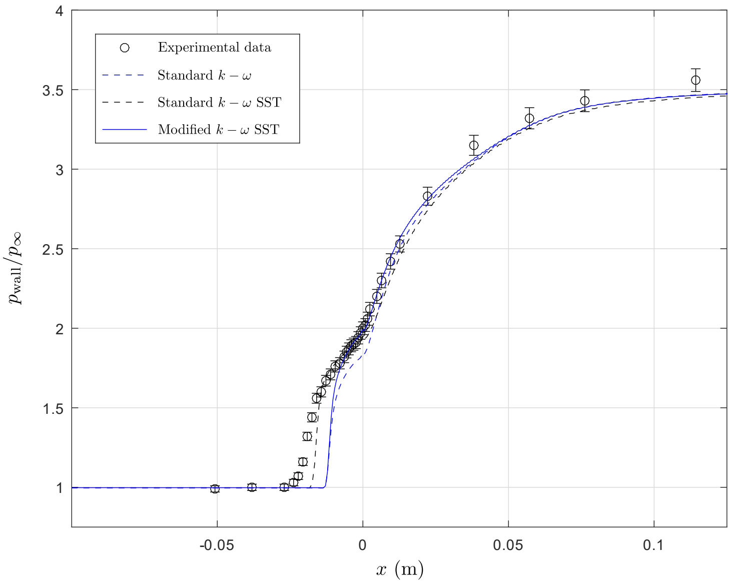

Figure 39: Comparison between pressure distributions over the wall of the computational domain using different turbulence models (II). Experimental data extracted from Settles et al. [6, 7].

Regarding the presented data, the standard $k-\omega$ SST model is the one that better characterises the upstream part of the interaction from all the considered models in the study. On the other hand, with the modification introduced in the model presented by Georgiadis and Yoder, the downstream part of the interaction is more adequately characterised, whereas the upstream shock-influence is not very far from the results of the standard $k-\omega$ SST model.

[9] From now on, the Georgiadis and Yoder version of the $k-\omega$ SST model will be denoted as 'modified $k-\omega$ SST model' for simplicity.

To follow with the analysis, the distributions of the module of the skin friction coefficient over the wall presented in Figure 40 will be used. Here again, the results show that both the modified $k-\omega$ SST model and the standard $k-\omega$ models are the ones that better predict the extent of the separation region, falling very close to the experimental values.

However, it should be noted the standard $k-\omega$ shows better agreement with the experimental data in the downstream part of the interaction in comparison with the modified $k-\omega$ SST model. Finally, as previously stated in the grid convergence study, the extent of the separated bubble seems to be significantly overestimated in the standard $k-\omega$ SST, tendency which was already identified in the numerical study performed by Georgiadis and Yoder [41].

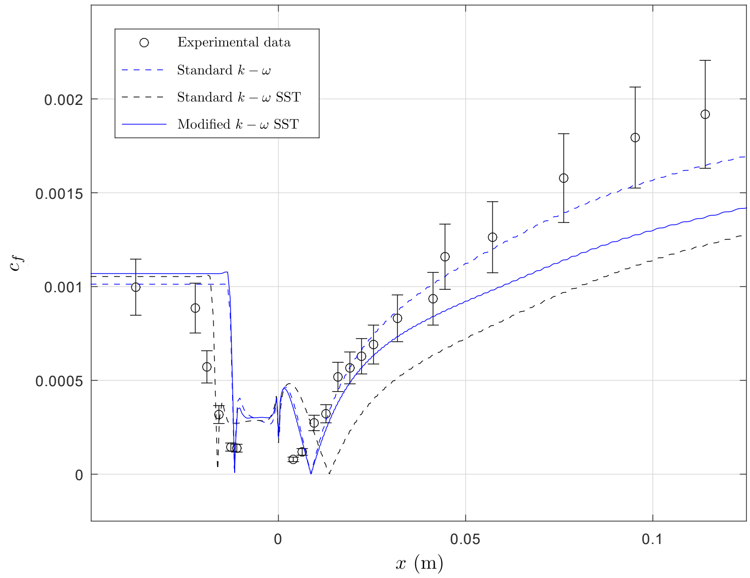

Figure 40: Comparison between skin friction coefficient (module) over the wall of the computational domain using different turbulence models (II). Experimental data extracted from Settles et al. [6,7].

Here again, in order to quantitatively compare the subsequent obtained solutions, the same error parameters presented in the grid convergence study will be used (Table 9). Thus, the results show the same tendencies previously described, with an overestimation of the separation length on the standard $k-\omega$ SST model and very similar results on both the standard $k-\omega$ and the modified $k-\omega$ SST model. Nonetheless, it should be noted that a much better agreement with the mean wall pressure distribution is found in the modified $k-\omega$ SST solution, whereas the bigger skin friction coefficient error in this solution is justified through the disagreement with the experimental values in the downstream part of the interaction.

Table 9: Error parameters of the solutions obtained using the compared turbulence models (II).

Turbulence model	CPU time (s)	l_{sep} (mm)	e_1 (-)	$e_2 \cdot 10^3$ (-)
Standard $k-\omega$	2694.3	20.42	1.405	1.190
Standard $k-\omega$ SST	3902.7	29.85	0.715	1.751
Modified $k-\omega$ SST	4064.0	20.42	1.255	1.557

On the other hand, comparing the required computational time, it should be outlined that the two versions of the $k-\omega$ SST model require very similar computational resources, whereas the standard $k-\omega$ model requires a computational effort of less than a 33% in comparison with the former.

A very similar analysis to the one that has just been done was performed by Wilcox [10], where two versions of the $k-\omega$ model (with and without stress limiter) were compared. Thus, the obtained results by Wilcox from the mean wall pressure and the skin friction coefficient distributions are presented in Figure 41.

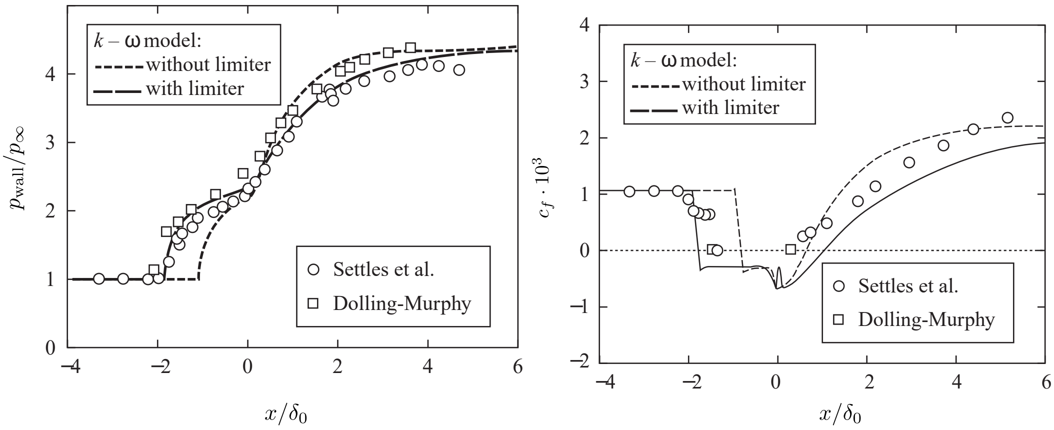

(a) Mean wall pressure distribution.

(b) Mean skin friction coefficient distribution.

Figure 41: Comparison of RANS computations for the flow over a 24° compression ramp with $\mathrm{M}_\infty = 2.8$, $\mathrm{Re}_{\delta_0} = 1.33 \cdot 10^6$, $T_{\mathrm{wall}}/T_{wall,adiabatic} = 0.88$, using a modified $k-\omega$ turbulence model. Extracted from Wilcox [10].

In this case, where a 24° compression corner was simulated, the pressure distribution from the $k-\omega$ version with stress limiter falls very close to the experimental measurements, whereas the skin friction distribution (specially on the downstream part of the interaction) is partly underestimated. On the other hand, the $k-\omega$ version without stress limiter shows in general a good agreement with the experimental measurements on both the pressure and wall shear distributions.

Regarding the presented results, it seems clear that the prediction of shock wave/turbulent boundary layer interactions using the RANS approach is a very complex problem, which is nowadays still limited, specially where the adverse pressure gradient imposed by the shock generates a significant separation bubble. This can be justified appealing to the nature of the variety of phenomena that appears in the flow field (compressibility effects, unsteadiness, major heat transfer processes...).

According to Babinsky and Harvey [31], the usage of more sophisticated turbulence models (e.g. Reynolds Stress turbulence model, which considers the full Reynolds stress tensor), or even Large Eddy Simulation (LES) and Detached Eddy Simulation (DES) modelling[10] may provide significant improvements in the characterisation of the turbulent behaviour within the interaction. The first presented option, although it still remains under the RANS approach, was considered to be beyond of the scope of the current study, which was intended to analyze only the models that use the Boussinesq assumption.

Finally, taken into account the performed analysis, the two models that show better agreement with the experimental data are the standard $k-\omega$ and the modified $k-\omega$ SST models. Although the global error parameters obtained with the former are smaller, as a result of the better agreement that the mean wall pressure distribution of the modified $k-\omega$ SST shows in the vicinity of the ramp junction, this model has been selected as the one that better performed in the studied case. Thus, this model will be the one used for the adaptive mesh refinement study that will be subsequently performed.

[10] LES is based on the capture of the unsteady travelling bid eddies through the domain, which at the same time requires much more grid resolution and computational requirements. On the other hand, DES is based on the coupling of the presented LES formulation for the majority of the domain, and the usage of RANS modelling within the boundary layer to reduce the overall computational cost.

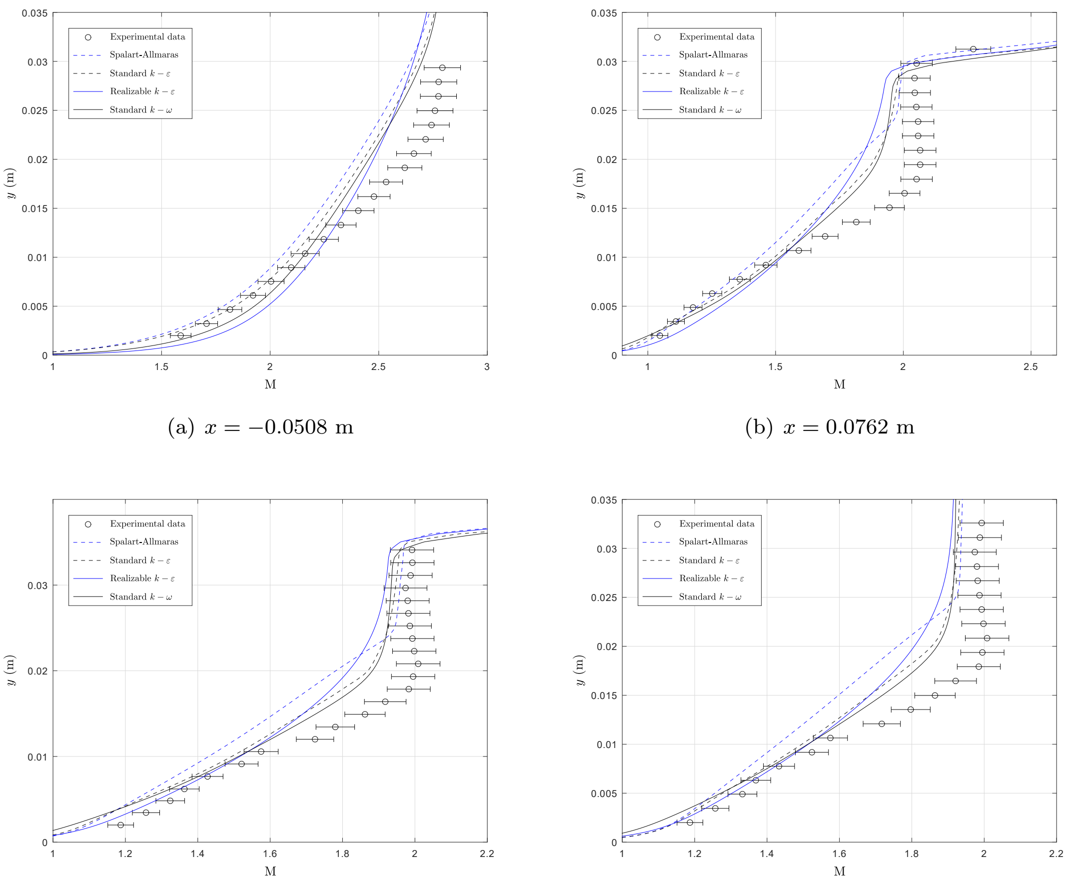

(a) $x = -0.0508$ m

(b) $x = 0.0762$ m

(c) $x = 0.0952$ m

(d) $x = 0.1143$ m

Figure 42: Comparison between mean Mach number profiles at different locations (turbulence model assessment (I)). 20° compression corner, for an incoming airflow with M= 2.85. Experimental data extracted from Settles et al. [6, 7].

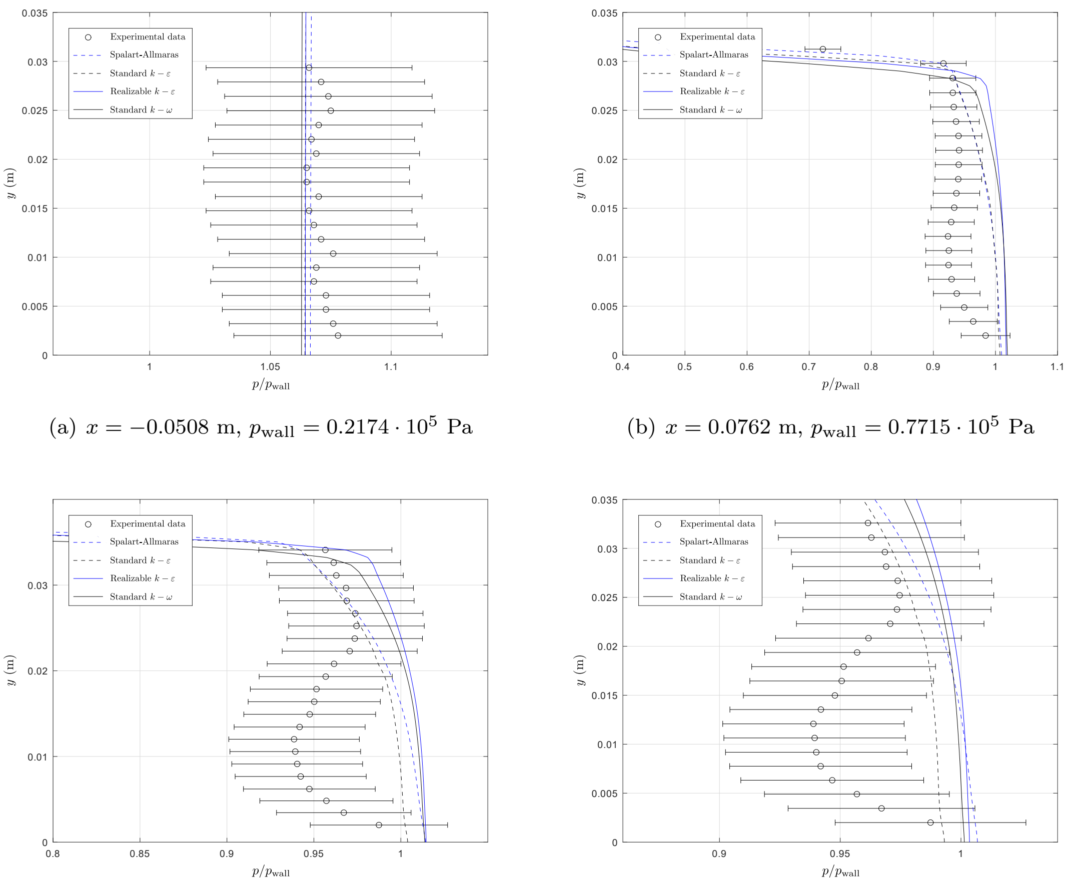

(a) $x = -0.0508$ m, $p_{\mathrm{wall}} = 0.2174 \cdot 10^5$ Pa

(b) $x = 0.0762$ m, $p_{\mathrm{wall}} = 0.7715 \cdot 10^5$ Pa

(c) $x = 0.0952$ m, $p_{\mathrm{wall}} = 0.7874 \cdot 10^5$ Pa

(d) $x = 0.1143$ m, $p_{\mathrm{wall}} = 0.8032 \cdot 10^5$ Pa

Figure 43: Comparison between mean pressure profiles at different locations (turbulence model assessment (I)). 20° compression corner, for an incoming airflow with M= 2.85. Experimental data extracted from Settles et al. [6, 7].

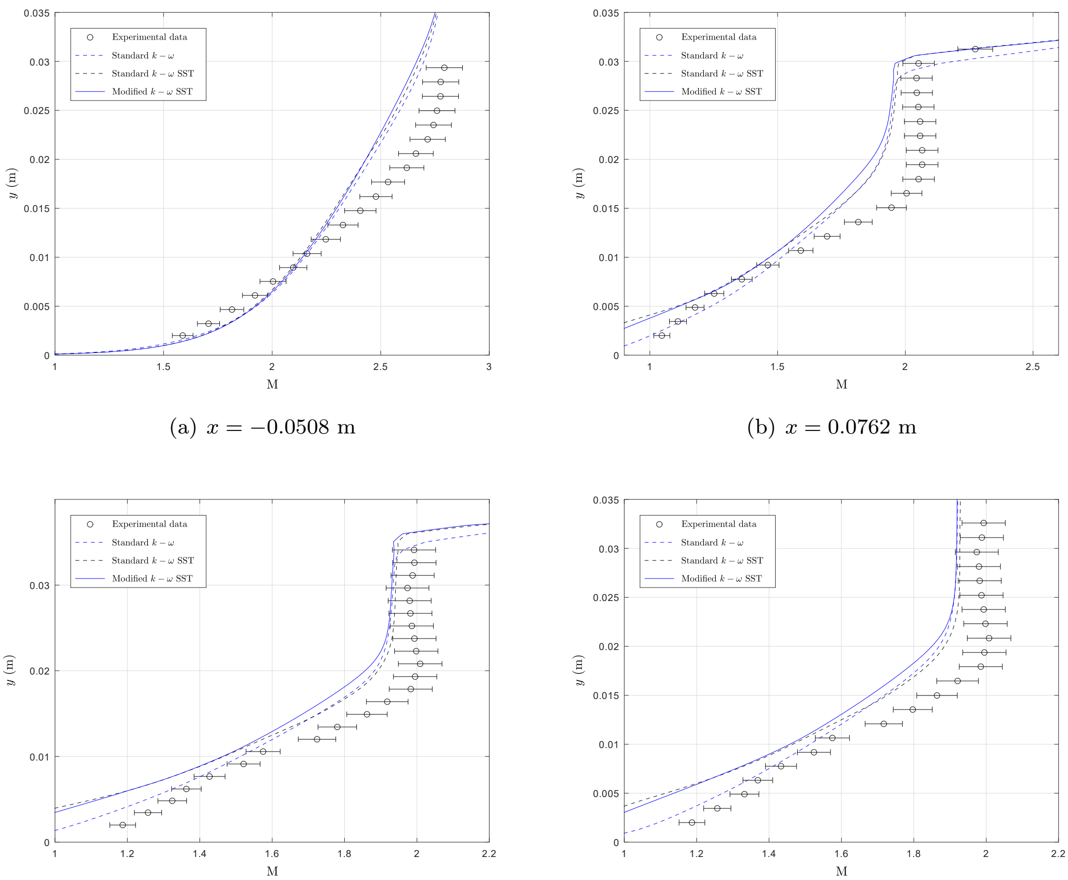

(a) $x = -0.0508$ m

(b) $x = 0.0762$ m

(c) $x = 0.0952$ m

(d) $x = 0.1143$ m

Figure 44: Comparison between mean Mach number profiles at different locations (turbulence model assessment (II)). 20° compression corner, for an incoming airflow with M= 2.85. Experimental data extracted from Settles et al. [6, 7].

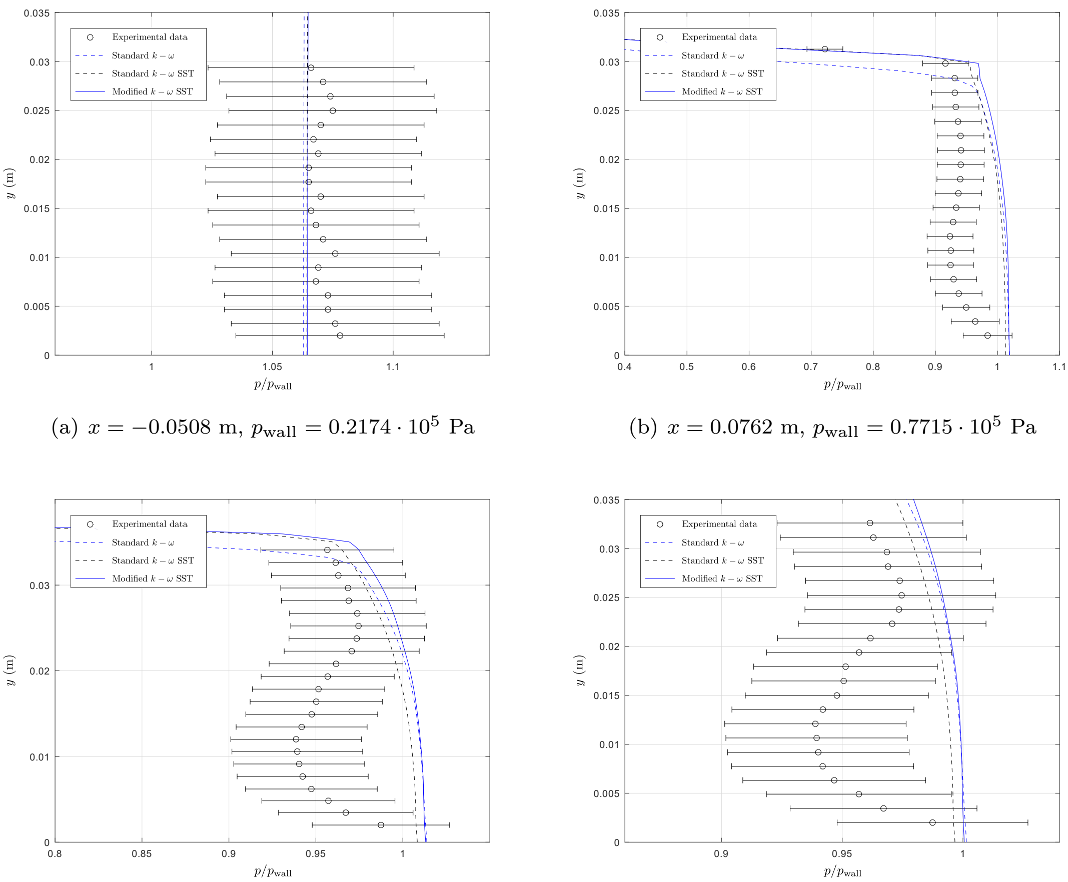

(a) $x = -0.0508$ m, $p_{\mathrm{wall}} = 0.2174 \cdot 10^5$ Pa

(b) $x = 0.0762$ m, $p_{\mathrm{wall}} = 0.7715 \cdot 10^5$ Pa

(c) $x = 0.0952$ m, $p_{\mathrm{wall}} = 0.7874 \cdot 10^5$ Pa

(d) $x = 0.1143$ m, $p_{\mathrm{wall}} = 0.8032 \cdot 10^5$ Pa

Figure 45: Comparison between mean pressure profiles at different locations (turbulence model assessment (II)). 20° compression corner, for an incoming airflow with M= 2.85. Experimental data extracted from Settles et al. [6, 7].

4.3 Adaptive mesh refinement

To finish with the numerical analysis, an adaptive mesh refinement study will be carried out using the facilities implemented in Ansys Fluent. In particular, the standard AMR procedure presented in Section 3.5 will be used, starting from the coarse grid solution calculated using the modified $k-\omega$ SST model (which was identified as the one that better performed for the studied case in the former section). Moreover, the AMR steps will evaluate the numerical error through several gradients of properties (e.g. temperature or Mach number) using the scale normalisation option recommended by Fluent, previously establishing some refinement criteria.

Thus, in each of these steps, once the refinement algorithm has been executed and the solution has been mapped into the subsequent mesh, the solver will be run until the solution is again converged (under the same criteria used in the rest of the numerical study). Once this convergence is reached, the obtained solution will be compared against the fine grid flow field[11] in order to assess whether the solution could be accepted as sufficiently accurate.

Hence, the subsequent solutions will be compared using the three presented error parameters (l_{sep}, e_1 and e_2), and the AMR solution will be considered sufficiently accurate if all these parameters are within a 5% from the ones associated to the fine grid solution, finishing in that case the AMR procedure. Finally, it should be outlined that this methodology will be carried out in three different cases, studying the suitability of the refinement criteria based on pressure gradients, velocity gradients and the combination of the former; which have been identified as the ones which better characterise the errors within the flow field, allowing at the same time larger reductions in the computational requirements.

4.3.1 AMR based on pressure gradients

To start with, in the first case that has been studied, the adaptive mesh refinement procedure was based on the pressure gradients within the domain. That is, at each step, the cells to be refined has been selected through a criterion based on this magnitude, where a threshold value has been specified, above which all the cells has been marked to be refined.

In particular, after a number of attempts, it has been identified that the most appropriate refinement criterion was to mark all the cells with a pressure gradient above 1.5 (given the scale normalisation option selected, which divides the threshold values by the mean value of the gradient throughout the entire domain). Additionally, it has been imposed that only the cells with a minimum area of $5 \cdot 10^{-8}$ m^2 could be marked to be refined, so that the lower part of the boundary layer remains without changes, since the modification of the topology of this region may lead to disturbances in the subsequent solution.

Table 10: Error parameters throughout the different stages of refinement (AMR based on pressure gradients).

Case	CPU time (s)	Cell Count (-)	l_{sep} (mm)	e_1 (-)	$e_2 \cdot 10^3$ (-)
Coarse	440.0	21452	12.58	1.794	1.823
AMR 1	544.4	24644	15.32	1.599	1.799
AMR 2	640.2	27641	16.56	1.475	1.717
AMR 3	801.1	30710	20.43	1.232	1.588
Fine	4064.0	90387	20.42	1.255	1.557

These criteria have been maintained throughout all the AMR steps, evaluating the accumulated CPU time, the cell count and the error estimators at the end of each of them (Table 10). The criteria imposed in each of the performed AMR steps could be found at Table 11, in order to clarify the procedure that has been carried out.

[11] The AMR solutions will be compared against the one obtained from simulating the flow field in the fine grid, since it has been proved through the grid convergence study to be a grid independent solution.

Hence, this procedure has been repeated for three times until a solution with the desired level of accuracy (differences of 5% or less from the error parameters of the fine grid solution) has been reached. As it could be observed, the AMR 3 solution nearly matches the extent of the separation bubble predicted by the fine grid solution, whereas the mean wall pressure and skin friction coefficient error estimators are very close to the latter, with an overall CPU time reduction of a 80.3%. To support the suitability of the obtained solution, the mean pressure distribution over the wall of the computational domain of several AMR steps has been plotted against the same distribution on the coarse and fine grid solutions (Figure 46).

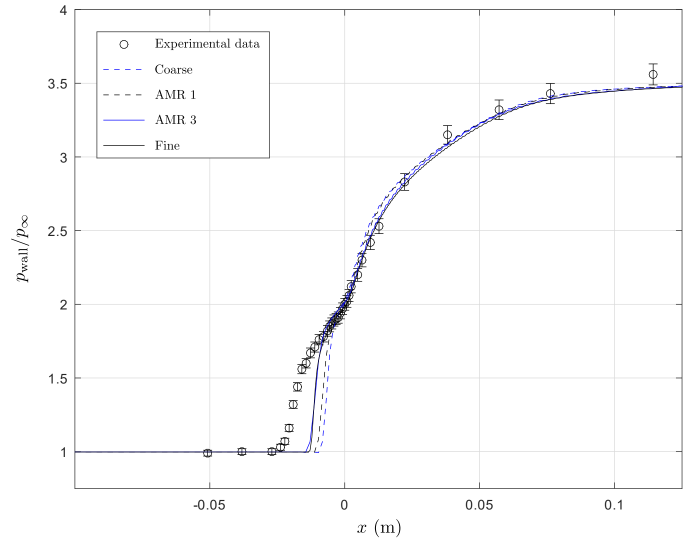

Figure 46: Mean pressure distribution over the wall of the computational domain (AMR based on pressure gradients). Experimental data extracted from Settles et al. [6, 7].

As it could be noted, as the mesh is refined, the mean pressure distribution falls closer to the fine grid solution, finally obtaining a nearly identical data set at the third step of the AMR procedure. As a result, it could be stated that the accuracy criteria based on the three error estimators that has been used could be accepted as reasonable.

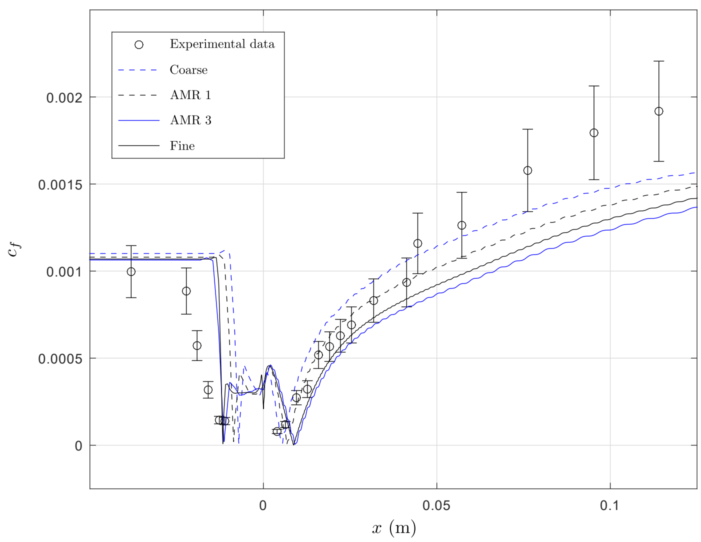

Figure 47: Mean skin friction coefficient (module) distribution over the wall of the computational domain (AMR based on pressure gradients). Experimental data extracted from Settles et al. [6, 7].

To support this conclusion, the mean skin friction coefficient distribution over the wall of the computational domain has been plotted comparing AMR 1 and AMR 3 solutions against the ones from computing the flow field with the coarse and fine grids (Figure 47).

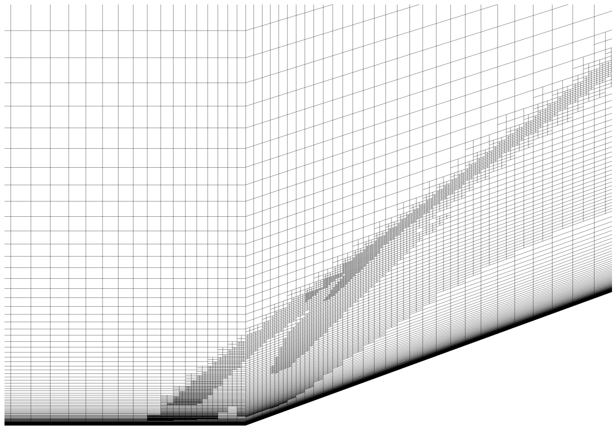

Figure 48: Detail of the vicinity of the ramp junction on the resulting mesh (AMR based on pressure gradients).

Thus, the same tendency previously outlined is again found, with an expansion of the separation bubble as the grid is refined until reaching a nearly identical solution to the one from the fine grid (this behaviour could be also observed in the l_{sep} evolution of Table 10). Moreover, this convergence to the fine grid solution could be noticed regarding the profiles presented in Figures 49 and 50.

Finally, by observing the mesh obtained after the third step of the AMR procedure (Figure 48), it could be stated that the refinement criteria based on pressure gradients have imposed a significant amount of cells in both the vicinity of the main and the secondary shock waves (according to the schematic of Figure 16), as well as a series of additional cells around the separation region and immediately downstream of the shock system.

With all the presented data, it seems clear that the AMR procedure carried out has moved the shock system upstream where it was located in the coarse grid solution, extending the length of the separation region until a solution very close to the fine grid flow field has been obtained, with a very significant reduction in the overall computational time.

Table 11: Refinement criteria throughout the different stages of refinement (AMR based on pressure gradients).

Case	Evaluated magnitude	Type of normalization	Refinement criterion	Minimum area (m^2)
AMR 1	Pressure gradient	Scale	1.5	$5 \cdot 10^{-8}$
AMR 2	Pressure gradient	Scale	1.5	$5 \cdot 10^{-8}$
AMR 3	Pressure gradient	Scale	1.5	$5 \cdot 10^{-8}$

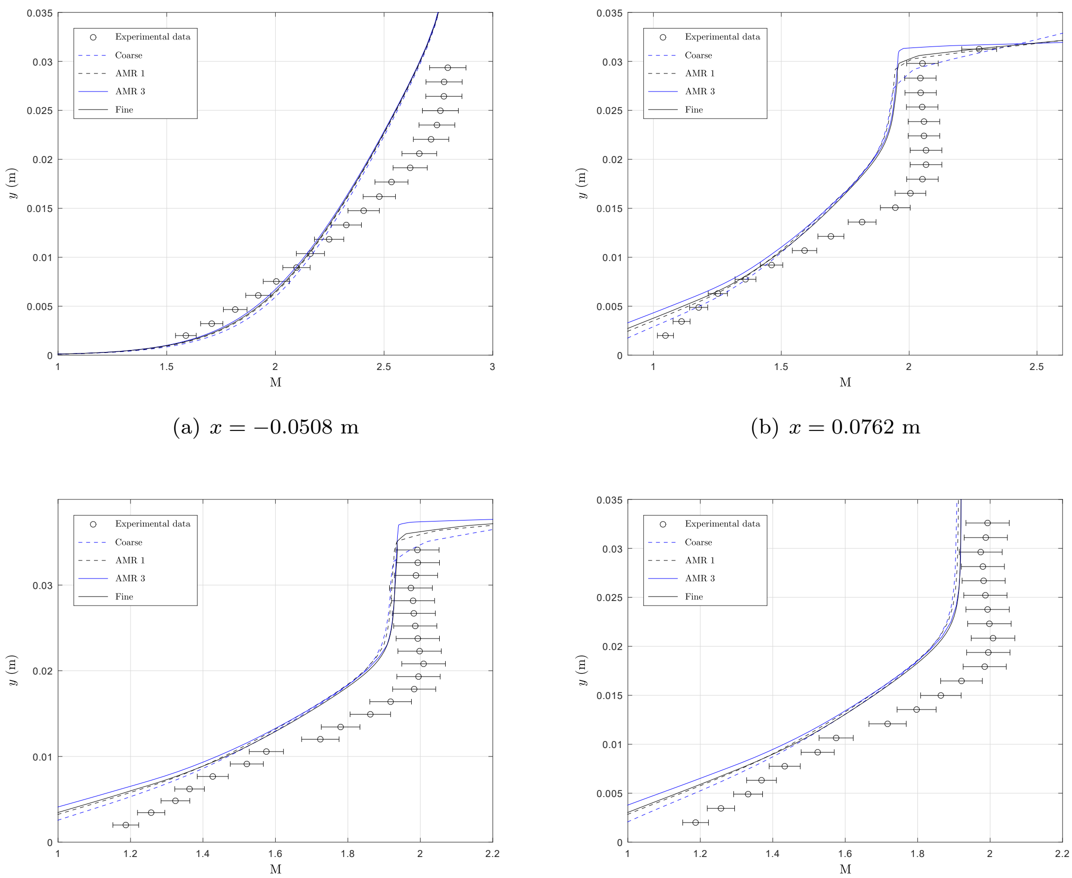

(a) $x = -0.0508$ m

(b) $x = 0.0762$ m

(c) $x = 0.0952$ m

(d) $x = 0.1143$ m

Figure 49: Comparison between mean Mach number profiles at different locations (AMR based on pressure gradients). 20° compression corner, for an incoming airflow with M= 2.85. Experimental data extracted from Settles et al. [6, 7].

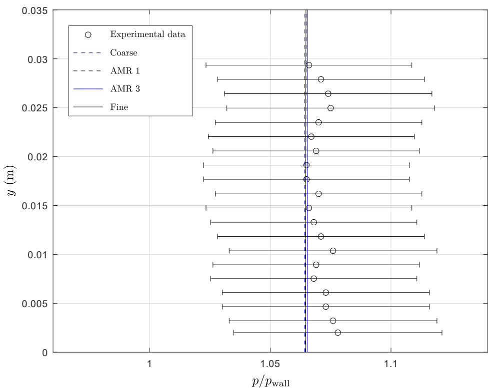

(a) $x = -0.0508$ m, $p_{\text{wall}} = 0.2174 \cdot 10^5$ Pa

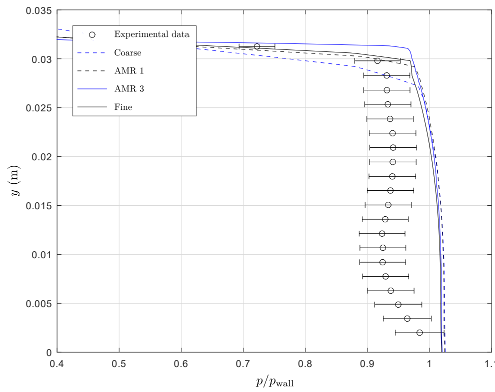

(b) $x = 0.0762$ m, $p_{\text{wall}} = 0.7715 \cdot 10^5$ Pa

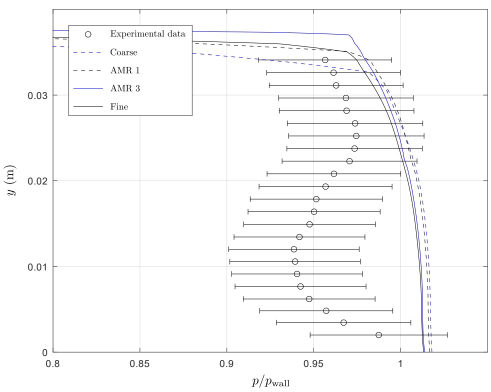

(c) $x = 0.0952$ m, $p_{\text{wall}} = 0.7874 \cdot 10^5$ Pa

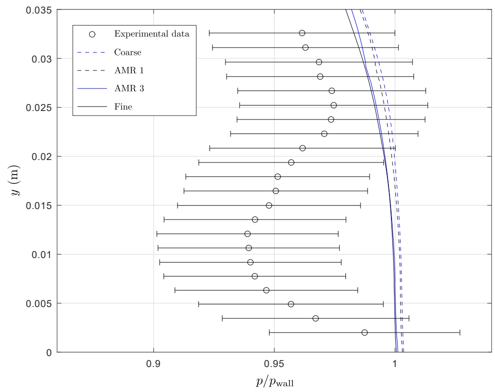

(d) $x = 0.1143$ m, $p_{\text{wall}} = 0.8032 \cdot 10^5$ Pa

Figure 50: Comparison between mean pressure profiles at different locations (AMR based on pressure gradients). 20° compression corner, for an incoming airflow with M= 2.85. Experimental data extracted from Settles et al. [6, 7].

4.3.2 AMR based on velocity gradients

To follow with the analysis, the same AMR procedure has been carried out, but taking into account the usage of refinement criteria based on velocity gradients instead of the previously analyzed pressure gradients. Thus, after a number of attempts, it has been identified that the most profitable criterion is based on refining the cells with a velocity gradient above 0.35 (given the scale normalisation option), if their area is greater than $5 \cdot 10^{-8}$ m^2 (due to the same reasons presented in the previous case). As in the latter section, the criteria used in each of the AMR steps could be found at Table 13, in order to clarify the procedure that has been carried out.

Table 12: Error parameters throughout the different stages of refinement (AMR based on velocity gradients).

Case	CPU time (s)	Cell Count (-)	l_{sep} (mm)	e_1 (-)	$e_2 \cdot 10^3$ (-)
Coarse	440.0	21452	12.58	1.794	1.823
AMR 1	489.5	34484	13.56	1.697	1.797
AMR 2	522.2	49199	14.53	1.652	1.791
AMR 3	667.4	59918	16.82	1.493	1.703
AMR 4	1004.3	69944	20.15	1.245	1.542
Fine	4064.0	90387	20.42	1.255	1.557

In this case, as it could be observed in Table 12, four AMR steps have been necessary to obtain a solution with the desired accuracy level. Hence, a solution where all the error parameters are within a 5% from the fine grid's error estimators is obtained after the AMR procedure, with an overall CPU time reduction of a 75.3% (partly inferior to the one obtained from the AMR based on pressure gradients). This last issue could be justified appealing to the larger amount of cells introduced by this criteria, as it could be noticed by comparing the data from Tables 10 and 12.

To assess the suitability of the obtained solution, the mean wall pressure distribution on the AMR 2 and AMR 4 steps has been plotted against the coarse and fine grid distributions (Figure 51). Here, the same tendency presented in the former case is found. That is, as the grid is refined, the mean pressure distribution falls closer to both the experimental data and the fine grid solution.

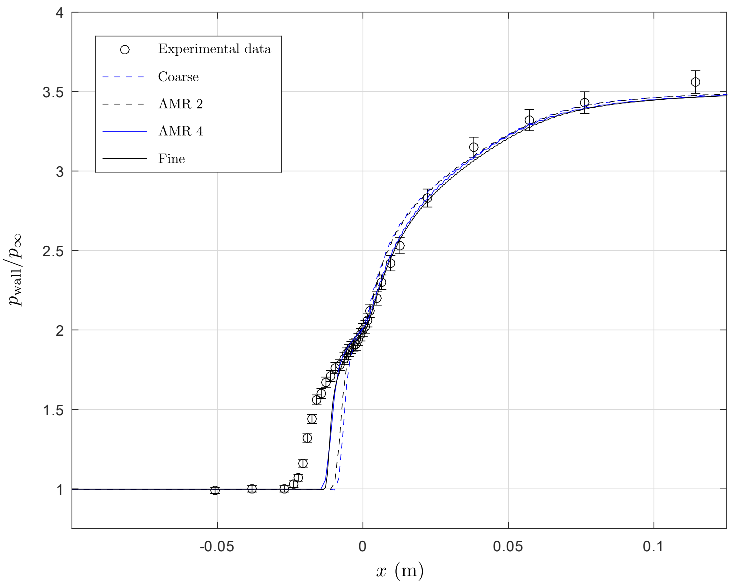

Figure 51: Mean pressure distribution over the wall of the computational domain (AMR based on velocity gradients). Experimental data extracted from Settles et al. [6, 7].

Hence, the AMR procedure increases the upstream influence of the shock system producing solutions closer to both the experimental values and the fine grid flow field. Additionally, it should be noted that this refinement criterion seems to impose a less steeper gradient at the beginning of the shock influence in comparison with the fine and coarse grids' solutions. To follow with the comparison between solutions, the mean skin friction coefficient distribution over the wall in the obtained AMR solutions has been plotted in order to compare them with the coarse and fine grid estimations (Figure 52).

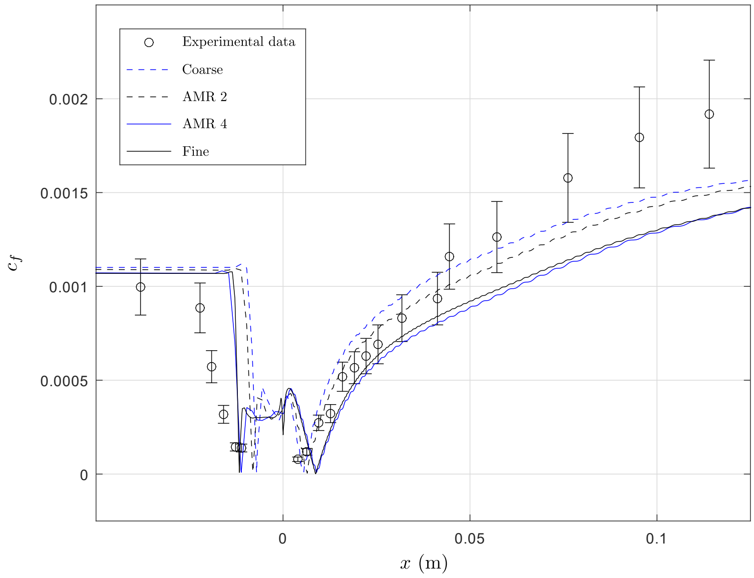

Figure 52: Mean skin friction coefficient (module) distribution over the wall of the computational domain (AMR based on velocity gradients). Experimental data extracted from Settles et al. [6,7].

As the grid is refined, the extent of the separation region increases, finally obtaining a distribution nearly identical to the fine solution (following the same tendency previously identified in the AMR based on pressure gradients' case). As in the latter section, this convergence could be also justified appealing to the profiles presented in Figures 54 and 55. To finish with this case, the resulting mesh after the AMR procedure is presented in the next figure (Figure 53).

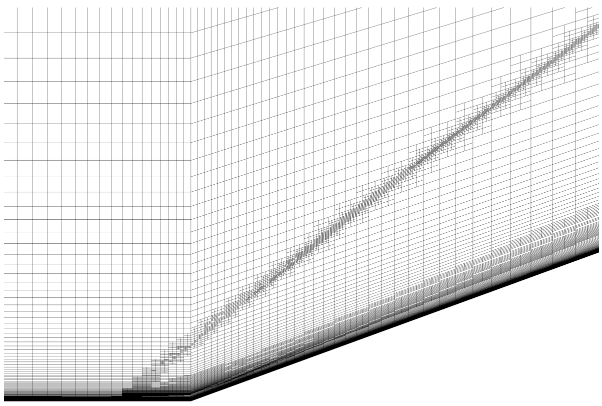

Figure 53: Detail of the vicinity of the ramp junction on the resulting mesh (AMR based on velocity gradients).

Hence, the topology of the resulting mesh could be used for justifying the lower reduction of the CPU time obtained in this case. As it could be observed, these criteria introduce fewer amount of cells in the shock wave system area in comparison with the AMR based on pressure gradients' case; whereas a significant amount of refined cells are introduced in the vicinity of the ramp junction at the upper part of the boundary layer. These latter extra cells may not contribute very significantly to the convergence to the fine grid solution, which may have lead to the need of an extra AMR step, at the same time of increasing the cell count and consequently the CPU time.

Nonetheless, it should be outlined that this option has also allowed to obtain an important reduction in the overall computational time in comparison with the fine grid solution, and the observed behaviour of introducing a bigger amount of cells at the upper boundary layer in the vicinity of the ramp junction will be used in the next case to assess whether it could lead to a more significant CPU time reduction in combination with the pressure gradient criteria.

Table 13: Refinement criteria throughout the different stages of refinement (AMR based on velocity gradients).

Case	Evaluated magnitude	Type of normalization	Refinement criterion	Minimum area (m^2)
AMR 1	Velocity gradient	Scale	0.35	$5 \cdot 10^{-8}$
AMR 2	Velocity gradient	Scale	0.35	$5 \cdot 10^{-8}$
AMR 3	Velocity gradient	Scale	0.35	$5 \cdot 10^{-8}$
AMR 4	Velocity gradient	Scale	0.35	$5 \cdot 10^{-8}$

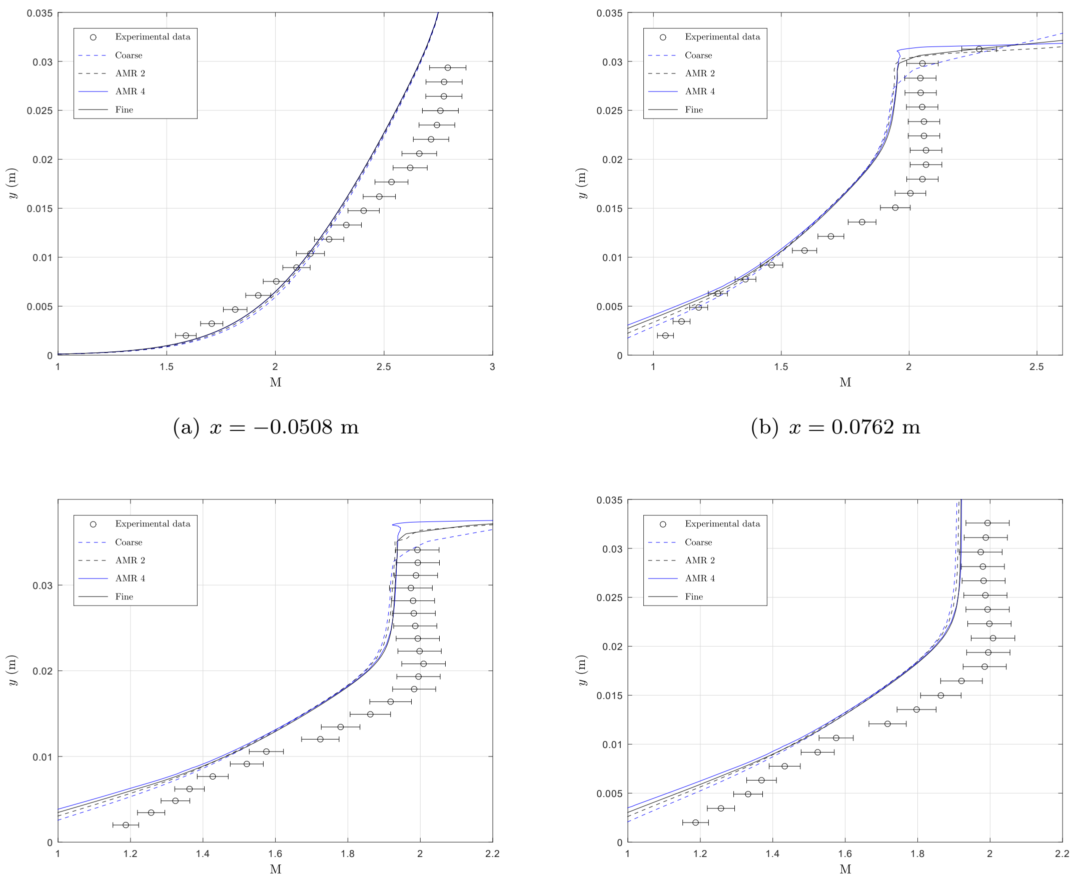

(a) $x = -0.0508$ m

(b) $x = 0.0762$ m

(c) $x = 0.0952$ m

(d) $x = 0.1143$ m

Figure 54: Comparison between mean Mach number profiles at different locations (AMR based on velocity gradients). 20° compression corner, for an incoming airflow with M= 2.85. Experimental data extracted from Settles et al. [6, 7].

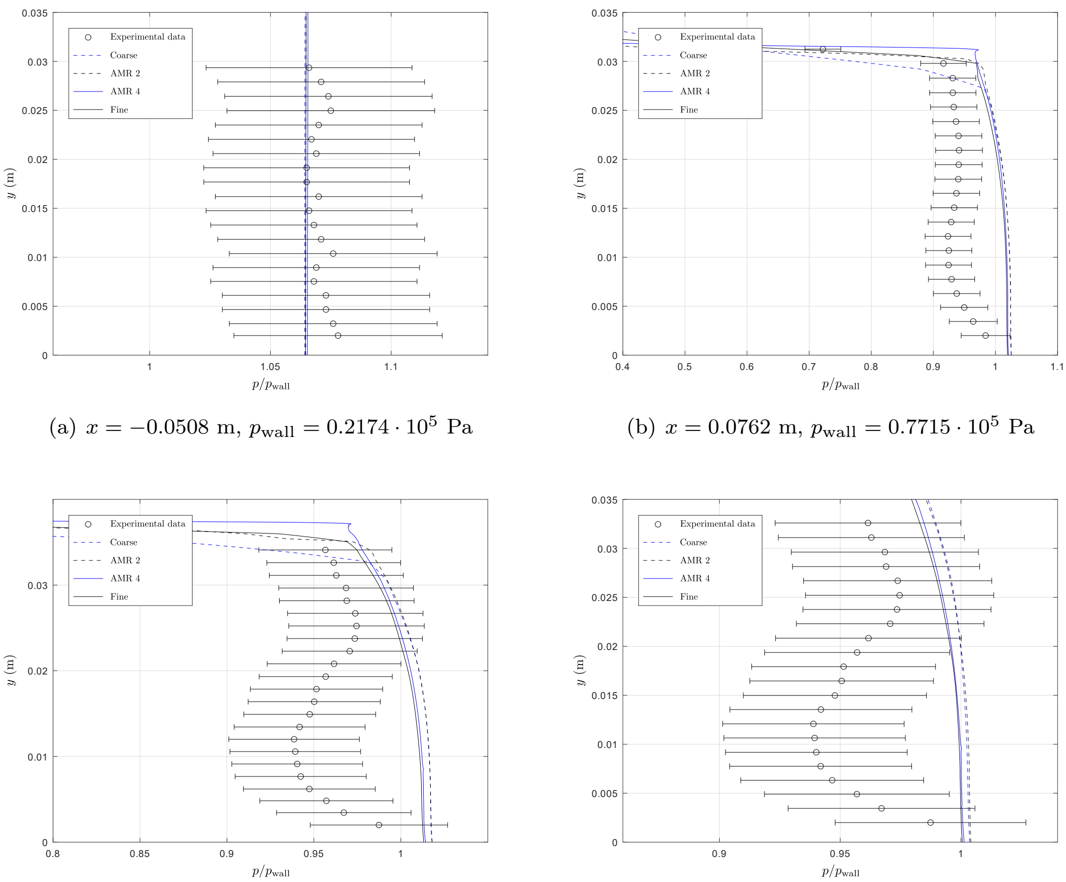

(a) $x = -0.0508$ m, $p_{\text{wall}} = 0.2174 \cdot 10^5$ Pa

(b) $x = 0.0762$ m, $p_{\text{wall}} = 0.7715 \cdot 10^5$ Pa

(c) $x = 0.0952$ m, $p_{\text{wall}} = 0.7874 \cdot 10^5$ Pa

(d) $x = 0.1143$ m, $p_{\text{wall}} = 0.8032 \cdot 10^5$ Pa

Figure 55: Comparison between mean pressure profiles at different locations (AMR based on velocity gradients). 20° compression corner, for an incoming airflow with M= 2.85. Experimental data extracted from Settles et al. [6, 7].

4.3.3 AMR based on combined criteria

In this section, the objective is to assess whether the combination of the larger amount of cells introduced in the vicinity of the shock wave system by the AMR based on pressure gradients' case; and the greater amount of cells introduced in the upper part of the boundary layer introduced by the AMR based on velocity gradients' case; could achieve greater reductions in the overall CPU time. Hence, many different refinement criteria have been analyzed following this philosophy, finally identifying the case presented in this section as the one which provides the better performance.

Thus, in order to firstly characterise the vicinity of the shock wave system, a first AMR step will be carried out by refining the cells with a a pressure gradient above 1.5 (given the scale normalisation criteria), and an area higher than $5 \cdot 10^{-8}$ m^2. After completing this AMR step, the cells where the velocity gradient is above 0.3 (given the scale normalisation criteria) and the area is higher than $5 \cdot 10^{-8}$ m^2 will be refined, so that all the benefits from the velocity gradients' option could be achieved in a single step of refinement, introducing a slightly less restrictive criterion than in the former section. Finally, the first refinement criteria based on pressure gradients will be again used until the convergence to the fine grid solution (given that it introduces a fewer amount of cells, in order to obtain a solution with fewer CPU requirements).

Table 14: Error parameters throughout the different stages of refinement (AMR based on combined criteria).

Case	CPU time (s)	Cell Count (-)	l_{sep} (mm)	e_1 (-)	$e_2 \cdot 10^3$ (-)
Coarse	440.0	21452	12.58	1.794	1.823
AMR 1	544.4	24644	15.32	1.599	1.799
AMR 2	591.0	41480	16.03	1.540	1.757
AMR 3	791.0	45824	20.34	1.258	1.565
Fine	4064.0	90387	20.42	1.255	1.557

After following the presented procedure, a sufficiently accurate solution has been obtained after three AMR steps (being all the error estimators within a 5% from the ones associated to the fine grid solution), with an overall CPU time reduction of a 80.5% (which is slightly higher than the benefits from the purely pressure gradient's AMR). For clarifying reasons, the criteria used in each of the performed AMR steps could be found at Table 15.

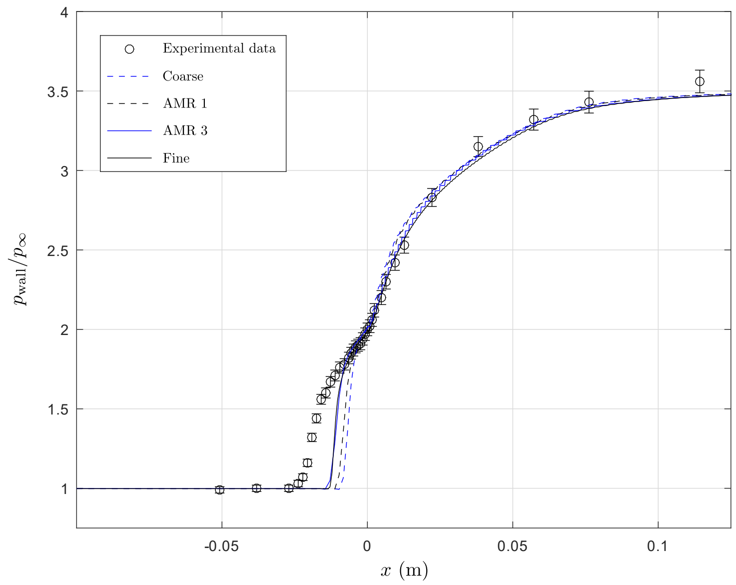

Figure 56: Mean pressure distribution over the wall of the computational domain (AMR based on combined criteria). Experimental data extracted from Settles et al. [6, 7].

To assess the suitability of the obtained solution, again the obtained mean pressure distributions over the wall throughout the AMR steps have been plotted against the coarse and fine grid solutions (Figure 56). Apparently, the same tendency predicted in the former sections is again found with a solution that falls closer to both the experimental data and the fine grid solution as the grid is refined.

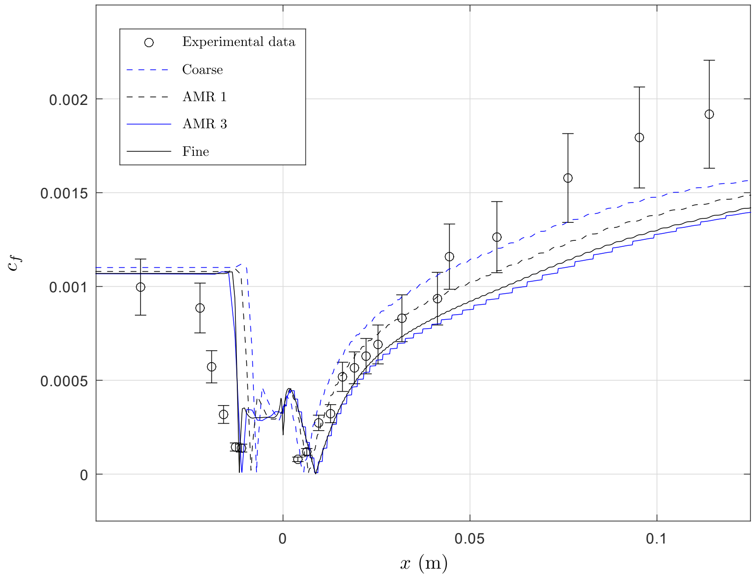

Figure 57: Mean skin friction coefficient (module) distribution over the wall of the computational domain (AMR based on combined criteria). Experimental data extracted from Settles et al. [6,7].

On the other hand, the mean skin friction coefficient distributions (Figure 57) show the same convergence to the fine grid solution as the AMR steps are accounted, producing an extension of the separation bubble until reaching a solution very close to the fine grid flow field. This convergence could be also observed through the profiles presented in Figures 59 and 60. Finally, the topology of vicinity of the ramp junction in the mesh generated after this AMR procedure could be found in Figure 58.

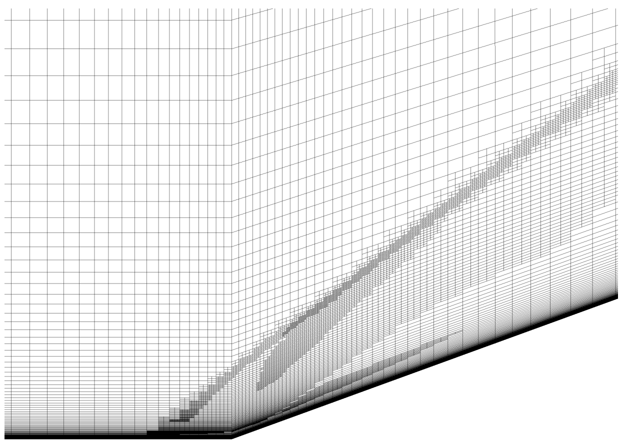

Figure 58: Detail of the vicinity of the ramp junction on the resulting mesh (AMR based on combined criteria).

As it could be observed, the resulting grid includes the benefits from the two used approaches. On one hand, the region containing the shock wave system is refined by the pressure gradient criterion imposed in the first and third AMR steps; whereas additional cells are included at the upper part of the boundary layer in the vicinity of the ramp junction from the velocity gradient criterion used in the second AMR step.

Hence, the benefits from using this kind of refinement (and consequently this kind of mesh) have lead to a slight reduction in the overall computational requirements in comparison with the AMR based on pressure gradients' case, although the total cell count in this case is greater than in the latter.

Table 15: Refinement criteria throughout the different stages of refinement (AMR based on combined criteria).

Case	Evaluated magnitude	Type of normalization	Refinement criterion	Minimum area (m^2)
AMR 1	Pressure gradient	Scale	1.5	$5 \cdot 10^{-8}$
AMR 2	Velocity gradient	Scale	0.3	$5 \cdot 10^{-8}$
AMR 3	Pressure gradient	Scale	1.5	$5 \cdot 10^{-8}$

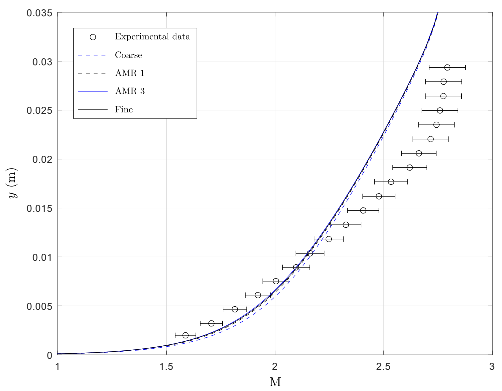

(a) $x = -0.0508$ m

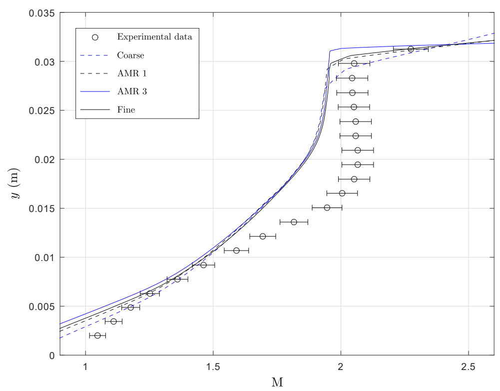

(b) $x = 0.0762$ m

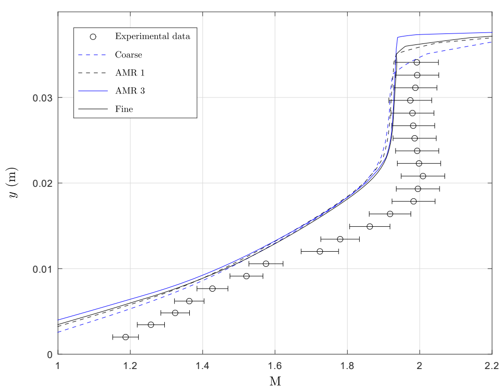

(c) $x = 0.0952$ m

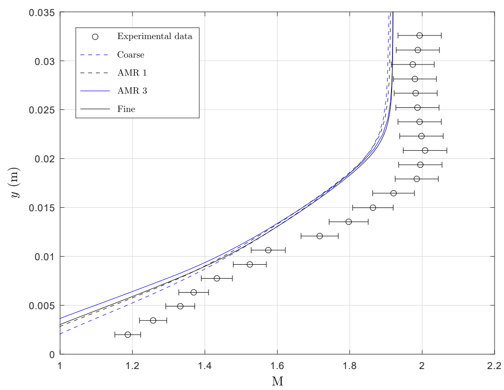

(d) $x = 0.1143$ m

Figure 59: Comparison between mean Mach number profiles at different locations (AMR based on combined criteria). 20° compression corner, for an incoming airflow with M= 2.85. Experimental data extracted from Settles et al. [6, 7].

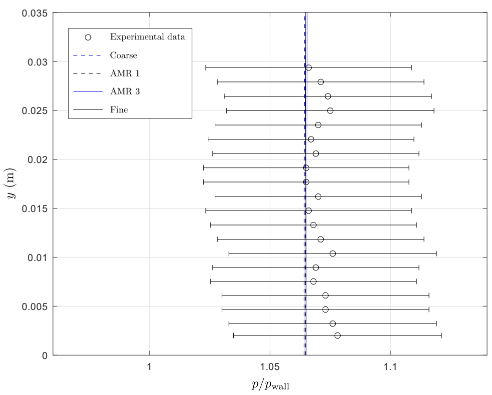

(a) $x = -0.0508$ m, $p_{\text{wall}} = 0.2174 \cdot 10^5$ Pa

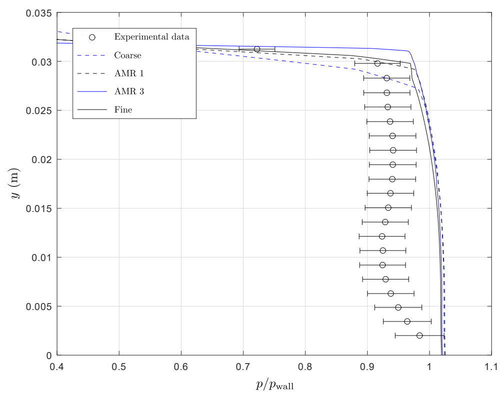

(b) $x = 0.0762$ m, $p_{\text{wall}} = 0.7715 \cdot 10^5$ Pa

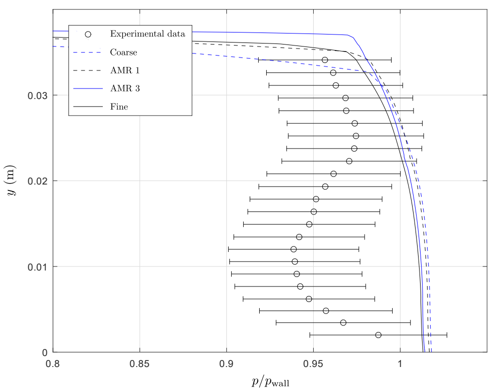

(c) $x = 0.0952$ m, $p_{\text{wall}} = 0.7874 \cdot 10^5$ Pa

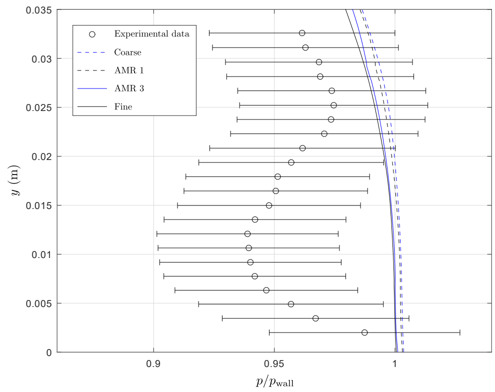

(d) $x = 0.1143$ m, $p_{\text{wall}} = 0.8032 \cdot 10^5$ Pa

Figure 60: Comparison between mean pressure profiles at different locations (AMR based on combined criteria). 20° compression corner, for an incoming airflow with M= 2.85. Experimental data extracted from Settles et al. [6, 7].

4.3.4 Concluding remarks

Through the development of the current section, several configurations of refinement criteria have been tested in order to assess whether they could lead to significant computational benefits in comparison with the classical refinement techniques used during Section 4.1. Thus, a comparison between the outcome of this attempts could be found in Table 16.

On one hand, the refinement criteria based on pressure gradients have proved to provide significant computational benefits, leading to a relatively fast convergence to the 'grid independent' solution, being the option which includes the fewer amount of additional refinement cells. Moreover, it has been observed that the majority of these cells are included in the vicinity of the shock system, properly characterising the gradients of fluid properties throughout these regions.

Table 16: Comparison between the various AMR approaches considered in the numerical study.

Case	CPU time reduction (%)[12]	Cell Count (-)
AMR based on pressure gradients	80.3	30710
AMR based on velocity gradients	75.3	69944
AMR based on combined criteria	80.5	45824
Fine	-	90387

On the other side, the refinement criteria based on velocity gradients have also proved to provide significant reductions in the overall CPU time. However, this method has required more computational resources than in the former case to converge to the 'sufficiently accurate' solution, resulting in a poorer CPU time reduction. This could be justified appealing to the larger number of additional cells introduced in this latter procedure, mostly in the upper part of the boundary layer, which may have lead to bigger computational efforts, at the same time of not including the same proportion of cells into the region of the shock wave system.

Finally, in order to assess whether or not the combination of the two former approaches could lead to greater computational benefits, a procedure based on the usage of both pressure and velocity gradients has been carried out. Thus, a slight increase in the CPU time reduction in comparison with the pressure gradient case has been achieved, with a growth in the overall cell count. This last issue is somehow contradictory since generally a bigger amount of cells requires larger computational resources.

Nonetheless, it could be justified appealing to the importance of where (e.g. regions that do not represent big difficulties for the calculation algorithm), and at what AMR step the extra cells are included. At the same time, the benefits from both the used approaches are found within the resulting grid, with an inclusion of additional refinement cells at both the shock wave system region and the upper part of the boundary layer in the vicinity of the ramp junction.

However, it should be outlined that for producing this last result, many test were needed to be performed in order to obtain the most adequate parameters that produced a CPU reduction closer to the one from the AMR based on pressure gradients' case. Thus, as a result of the iterative nature of this last alternative and the high level of user knowledge required for the obtention of the results, the AMR based on pressure gradients' case has been considered to be the one that better performs for the intended flow.

[12] In comparison with the computational requirements needed for the fine grid solution under the same conditions.

5 Conclusions

The supersonic flow over a nominally two-dimensional 20° compression corner where a strong shock wave/turbulent boundary layer interaction is produced has been simulated using the Reynolds Averaged Navier-Stokes (RANS) approach[13] in order to conduct a numerical study to assess the suitability of adaptive mesh refinement methods. Thus, this study has been performed using a structured grid and the Georgiadis and Yoder version of the $k-\omega$ SST turbulence model, which was previously identified as the one which better performs for the studied flow, having compared several one and two-equation turbulence models.

The flow simulation with this latter model has proved to match the experimental extent of the separation bubble, at the same time of presenting a mean wall pressure distribution which falls very close to the experimental one. Nonetheless, it should be noted that the solution obtained using the standard $k-\omega$ SST model was the one that better agreed with the experimental mean wall pressure distribution, whereas the extent of the separation region on this latter case was significantly overpredicted.

On the other side, the solution obtained using the standard $k-\omega$ model had a very similar prediction of the location of the separation bubble in comparison with the Georgiadis and Yoder version of the $k-\omega$ SST model (being even closer to the experimental values in the overall skin friction distribution); however, the poorer agreement with the experimental mean wall pressure distribution that this model presented in the vicinity of the ramp junction caused the selection of the Georgiadis and Yoder version of the $k-\omega$ SST model to be used to perform the AMR study.

Thus, the numerical study carried out has proved the suitability of AMR methods within the simulation of flows involving shock wave/turbulent boundary interactions using the RANS approach, obtaining computational time reductions of more than a 80% in comparison with the fine grid solution. In particular, the analysis has been focused on the comparison between several refinement criteria based on both pressure and velocity gradients, which were previously identified as the ones that better characterised the errors within the flow field.

Hence, due to its simplicity and the lower level of user knowledge required for its usage, the AMR procedure based on purely pressure gradients refinement criteria has been selected as the one that better performs for the intended flow. Finally, as a result of the presented conclusions, it has been considered that the main objectives of the project has been achieved through the development of the current study.

Nonetheless, the author wants to emphasize at this point the major difficulties that were found during the development of the presented numerical study, where a large number of 'trial and error' cases were needed in order to obtain the presented results. As an example, many problems were found during the selection of the boundary conditions (where some of the considered alternatives leaded to either non-physical solutions or instabilities), the selection of y^+ (where many tests were needed to characterize the optimum element size near the wall given the high-speed nature of the studied flow), the set up for the initial conditions and control parameters of the simulations (which were needed to be selected very precisely, given that many tested configurations leaded to instabilities of the numerical method)...

Therefore, it seems clear that the simulation of a turbulent compressible high-speed flow, where a complex shock wave/boundary interaction occurs, is not an easy issue, given that the viscous effects cannot be disregarded and the boundary layer needed to be entirely characterized (without the usage of any wall function). This complexity can be illustrated by the dissimilarities found through the presented comparisons between numerical and experimental profiles of fluid magnitudes (e.g. Figures 34 and 35).

[13] In fact, the physics of the resolved problem are given by the Favre averaging equations (instead of the classical RANS equations). Nonetheless, following the nomenclature used by the authors of the field, the used approach has been denoted as RANS. This issue has been discussed with more detail during Section 3.1.

These differences may be justified appealing to either the RANS approach used for the characterization of the flow (given that the used turbulence models are the result of the generalization of experimental observations); or to the characterization of the inlet boundary condition (since the available experimental magnitudes of the profile at the beginning of the test section do not contain error bounds to assess the precision of the presented values).

5.1 Future lines of research

One of the biggest struggles that has been found during the development of the current study was the scarcity of public experimental data to be used to validate the simulations. In particular, not a major proportion of the available data sets had the amount and quality of measurements that were needed to perform such a numerical study (specially for the definition of the inlet boundary condition). Moreover, it should be outlined that future experimental studies may consider to perform heat flux measurements at the wall, which can be then used in order to evaluate the suitability of RANS simulations for its prediction.

Moreover, the current study has been only focused on the simulation of two dimensional shock wave/boundary layer interactions using the RANS approach, as a result of the available computational resources. Nonetheless, it would be interesting to conduct the same study in a three dimensional interaction in order to assess the performance of RANS calculations and AMR in these cases. On the other hand, the same analysis could be also performed using more complex approaches to simulate the flow such as DES, LES or DNS; but at the moment of writing the current document, the computational resources needed for taking into account the former simulations are far from being available to a student.

Finally, it should be outlined that another branch of study could comprise the usage of more sophisticated turbulence models which do not assume the Boussinesq approximation (such as the Reynold Stress Model), so that the benefits from using this more complex approach (as well as its coupling with AMR) could be assessed.

References

[1] L. He and X. Lu. *Visualization of the shock wave/boundary layer interaction using polarization imaging.* Journal of Visualization, Vol. 23, pp. 839-850, 2020.

[2] M. Van Dyke. *An Album of Fluid Motion.* The Parabolic Press, 4^{th} Edition, 1988.

[3] Z. Qinghu, Z. Zhiwei, L. Jingzhou, X. Futian, and Z. Jun. *Visualization of hypersonic incident shock wave boundary layer interaction.* Journal of Visualization, Vol. 23, pp. 207-214, 2020.

[4] E.R. Van Driest. *Turbulent Boundary Layer in Compressible Fluids.* Journal of the Aeronautical Sciences, Vol. 40, No. 6, pp. 1012-1028, 2003.

[5] R.D. Moser, J. Kim, and N.N. Mansour. *Direct numerical simulation of turbulent channel flow up to $Re_\tau = 590$.* Physics of Fluids, Vol. 11, pp. 943-945, 1998.

[6] G.S. Settles and L.G. Dodson. *Hypersonic Shock/Boundary-Layer Interaction Database.* NASA Contractor Report 177577, 1991.

[7] G.S. Settles and L.G. Dodson. *Hypersonic Shock/Boundary-Layer Interaction Database: New and Corrected Data.* NASA Contractor Report 177638, 1994.

[8] L. He, S. Yi, Z. Chen, and Y. Zhu. *Visualization of the structure of an incident shock wave/-turbulent boundary layer interaction.* Shock Waves, Vol. 24, pp. 583-592, 2014.

[9] J.R. Viegas and C.C. Hortsman. *Comparison of multiequation turbulence models for several shock separated boundary-layer interaction flows.* AIAA Journal, Vol. 17, No. 8, pp. 811-820, 1979.

[10] D. Wilcox. *Formulation of the $k - \omega$ turbulence model revised.* AIAA Journal, Vol. 46, No. 11, pp. 2823-2838, 2008.

[11] D.V. Gaitonde. *Progress in shock wave/boundary layer interactions.* Progress in Aeroespace Sciences, Vol. 72, pp. 80-99, 2015.

[12] D.S. Dolling. *Fifty years of shock-wave boundary layer interaction research: What's Next?* AIAA Journal, Vol. 39, No. 8, pp. 1517-1531, 2001.

[13] A.J. Smits and K.C. Muck. *Experimental Study of Three Shock Wave/Turbulent Boundary Layer Interactions.* Journal of Fluid Mechanics, Vol. 182, pp. 291-314, 1987.

[14] E. Schülein, P. Krogmann, and E. Stanewsky. *Documentation of two-dimensional impinging shock/turbulent boundary layer interaction flow.* 1996.

[15] D. Rettenmaier, D. Deising, Y. Ouedraogo, E. Gjonaj, H. De Gersem, D. Bothe, C. Tropea, and H. Marschall. *Load balanced 2D and 3D adaptive mesh refinement in OpenFOAM.* SoftwareX, Vol. 10, 2019.

[16] J. Yao, T. Lin, G.R. Liu, and C.L. Chen. *An adaptive GSM-CFD solver and its application to shock-wave boundary layer interaction.* International Journal of Numerical Methods for Heat Fluid Flow, Vol. 25, No. 6, pp. 1282-1310, 2015.

[17] X. Li, D. Fu, Y. Ma, and X. Liang. *Direct numerical simulation of shock/turbulent boundary layer interaction in a supersonic compression ramp.* Science China Physics, Mechanics and Astronomy, Vol. 53, pp. 1651-1658, 2010.

[18] M. Grilli, S. Hickel, and N.A. Adams. *Large-eddy simulation of a supersonic turbulent boundary layer over a compression–expansion ramp.* International Journal of Heat and Fluid Flow, Vol. 42, pp. 79-93, 2013.

[19] F. Tong, C. Yu, Z. Tang, and X. Li. *Numerical studies of shock wave interactions with a supersonic turbulent boundary layer in compression corner: turning angle effects.* Computers and Fluids, Vol. 149, pp. 56-69, 2017.

[20] B. John, V.N. Kulkarni, and G. Natarajan. *Shock wave boundary layer interactions in hypersonic flows.* International Journal of Heat and Mass Transfer, Vol. 70, pp. 81-90, 2014.

[21] B. John and V.N. Kulkarni. *Effect of leading edge bluntness on the interaction of ramp induced shock wave with laminar boundary layer at hypersonic speeds.* Computers and Fluids, Vol. 96, pp. 177-190, 2014.

[22] B. Yang, G. Li, and C. Zhang. *Numerical simulation on supersonic shock wave/boundary layer interaction.* Advances in Engineering Research, Vol. 113, pp. 870-874, 2017.

[23] A.V. Struchkov, A.S. Kozelkov, K.N. Volkov, A.A. Kurbin, R.N. Zhuckov, and A.V. Sarazov. *Numerical simulation of aerodynamic problems based on adaptive mesh refinement method.* Acta Astronautica, Vol. 172, pp. 7-15, 2020.

[24] R.C. Ripley, F.S. Lien, and M.M. Yovanovich. *Adaptive Unstructured Mesh Refinement of Supersonic Channel Flows.* International Journal of Computational Fluid Dynamics, Vol. 18, pp. 189-198, 2004.

[25] M. Forster. *Assessment of Adaptive Mesh Refinement Methods for Shock Boundary Layer Interaction.* MSc. Thesis. Cranfield University, 2013.

[26] J. Anderson. *Fundamentals of Aerodynamics.* McGraw-Hill, 5th Edition, 2011.

[27] G. Ben-Dov, O. Igra, and T. Elperin. *Handbook of shock waves, Volume 1.* Elsevier, 1st Edition, 2001.

[28] A. Barrero and M. Pérez-Saborid. *Fundamentos y Aplicaciones de la Mecánica de Fluidos.* McGraw-Hill, 1st Edition, 2005.

[29] H. Schlichting and K. Gersten. *Boundary-layer theory.* Springer, 9th edition, 2016.

[30] J. Meseguer and A. Sanz. *Aerodinámica básica.* Garceta, 2nd Edition, 2011.

[31] H. Babinsky and J.K. Harvey. *Shock Wave-Boundary-Layer Interactions.* Cambridge University Press, 1st Edition, 2011.

[32] B. Edney. *Anomalous heat transfer and pressure distributions on blunt bodies at hypersonic speeds in the presence of an impinging shock.* Aeronautical Reseach Institute of Sweden, FAA Report 115, 1968.

[33] M. Holden. *Shock wave/turbulent boundary layer interaction in hypersonic flow.* 15th Aerospace Sciences Meeting, 1977.

[34] J.E. Lewis, T. Kubota, and L. Lees. *Experimental investigation of supersonic two-dimensional boundary layer separation in a compression corner with and without cooling.* AIAA Journal, Vol. 6, No. 1, pp. 7-14, 1967.

[35] F.W. Spaid and J.C. Frishett. *Incipient separation of a supersonic, turbulent boundary layer, including effects of heat transfer.* AIAA Journal, Vol. 10, No. 7, pp. 915-922, 1972.

[36] T.B. Gatski and J.P. Bonnet. *Compressibility, Turbulence and High Speed Flow.* Elsevier, 2nd Edition, 2013.

[37] D.C. Wilcox. *Turbulence Modelling for CFD.* DCW Industries, 3rd Edition, 2006.

[38] P.R. Spalart and S.R. Allmaras. *A One-Equation Turbulence Model for Aerodynamic Flows.* La Recherche Aérospatiale, No. 1, pp. 5-21, 1994.

[39] B.E. Launder and D.B. Spalding. *The numerical computation of turbulent flows.* Computer Methods in Applied Mechanics and Engineering, Vol. 3, No. 2, pp. 269-289, 1974.

[40] F.R. Menter. *Two-Equation Eddy-Viscosity Turbulence Models for Engineering Applications.* AIAA Journal, Vol. 32, No. 8, pp. 1598-1605, 1994.

[41] N.J. Georgiadis and D.A. Yoder. *Recalibration of the Shear Stress Transport Model to Improve Calculation of Shock Separated Flows.* NASA Technical Report 217851, 2013.

[42] J.H. Morrison, T.B. Gatski, T.P. Sommer, H.S. Zhang, and R.M.C. So. *Evaluation of a near-wall turbulent closure model in predicting compressible ramp flows*, pages 239–250. 1993.

[43] *Ansys Fluent User's Guide.* 2021.

[44] R. Löhner. *Applied Computational Fluid Dynamics Techniques: An Introduction Based on Finite Element Methods.* Wiley, 2nd edition, 2008.

[45] H. Jasak. *Error Analysis and Estimation for the Finite Volume Method with Applications to Fluid Flows.* PhD Thesis. Imperial College, 1996.

Appendix A. Estimation of boundary layer thicknesses

In order to define the inlet boundary condition of the test section, a flat plate has been simulated so that the fluid magnitudes profiles which match with the experimental observations could be specified. For this purpose, certain parameters of the boundary layer need to be calculated via a numerical software. In particular, the available experimental data of the upstream profile consist of measures of the boundary layer thickness (δ), the displacement thickness (δ^*) and the momentum thickness (θ). To characterize these parameters, their standard definitions for a compressible flow have been used:

- Boundary layer thickness (δ) will be defined as the y coordinate (normal to the wall), where the tangential velocity has a value of:

$$u(\delta) = 0.99\ u_\infty \tag{42}$$

  Where u is the tangential velocity at a given location and u_∞ is the freestream external velocity.

- Displacement thickness (δ^*) will be defined as:

$$\delta^* = \int_0^\infty \left(1 - \frac{\rho u}{\rho_\infty u_\infty}\right)\ dy \tag{43}$$

  Where ρ is the density at a given location and ρ_∞ is the freestream external density. However, as a result of the spatial discretization of the computational, only discrete values of the fluid properties are known. For this reason, the integral will be approximated through a sum using first-order schemes:

$$\delta^* \simeq \sum_{i=1}^{n-1} \left(1 - \frac{(\rho_{i+1} + \rho_i)\ (u_{i+1} + u_i)}{4\rho_\infty u_\infty}\right)\ (y_{i+1} - y_i) \tag{44}$$

  Where n is the number of available measures within the normal-to-wall profiles and the subscript i represents the index of each of the available values.

- Displacement thickness (δ^*) will be defined as:

$$\theta = \int_0^\infty \frac{\rho u}{\rho_\infty u_\infty} \left(1 - \frac{u}{u_\infty}\right)\ dy \tag{45}$$

  Again, this expression needs to be approximated through a sum due to the spatial discretization of the domain. Thus, the momentum thickness will be estimated using first-order schemes as:

$$\theta \simeq \sum_{i=1}^{n-1} \frac{(\rho_{i+1} + \rho_i)(u_{i+1} + u_i)}{4\rho_\infty u_\infty} \left(1 - \frac{u_{i+1} + u_i}{2u_\infty}\right)\ (y_{i+1} - y_i) \tag{46}$$

These expressions have been implemented into an Octave code in order to obtain an estimation of δ, δ^* and θ throughout the simulated flat plate. Additionally, the code initially includes a data treatment algorithm to directly obtain the velocity and density profiles from the .dat files generated by Ansys Fluent[14]. For more details about the employed code, the reader is encouraged to consult the comments within the script (see Code 1).

[14] To allow Octave to properly manage the data exported from Ansys, the file headers of the generated .dat files should be deleted.

Code 1: Octave routine used for the estimation of δ, δ^* and θ.

```
close all
clear all
clc

% Loads from the exported Ansys profiles
vprofile=load("velcityprofile.dat");
dprofile=load("densityprofile.dat");
y=1000*vprofile(:,2);
u=vprofile(:,1);
rho=dprofile(:,1);

delta=0;
deltastar=0;
theta=0;
n=length(y);
% Boundary layer thickness estimation
for i=1:1:n
  if (u(i)>=0.99*u(n))
    delta=y(i);
    break;
  endif
endfor

% Displacement and momentum thicknesses estimation
for i=1:1:n-1
  deltastar=deltastar+(1-((rho(i)+rho(i+1))*(u(i)+u(i+1)))/(4*u(n)*rho(n)))*(y(i+1)-y(i));
  theta=theta+(1-(u(i)+u(i+1))/(2*u(n)))*(y(i+1)-y(i))*((rho(i)+rho(i+1))*(u(i)+u(i+1)))/(4*u(n)*rho(n));
endfor

delta
deltastar
theta
```

Appendix B. Error estimation within the numerical solution

In order to compare the subsequent computed solutions against the available experimental data, two errors parameters have been defined through the Equations 40 and 41. Thus, an Octave code with the aim of estimating these two magnitudes has been created (Code 2).

This routine starts with the importation of the computed distributions of both the wall pressure and wall shear stress module. After this, the computed data is processed (through a change in the axis system and a nondimensionalization) so that it could be compared against the experimental data, which has also been imported to the work environment. Once the two data sets to be compared have been defined, the algorithm continues with the calculation of the two errors parameters, following a nearly identical procedure.

Figure 61: Auxiliary schematic for the explanation of the interpolation algorithm.

Thus, the procedure comprises the iterative sum of each of the squared terms from the error vector of the studied magnitude. To perform this sum, the computed value associated to each of the discrete experimental data should be previously estimated. For this purpose, a standard linear interpolation algorithm based on the inverse distance has been implemented in the code.

To illustrate the interpolation algorithm, the schematic of Figure 61 will be used, which represents two points where computational data are available and a third point between the two former, whose associated experimental values are aimed to be compared. Thus, to calculate the computed value to be compared against this experimental data, two coefficients α_1 and α_2 will be defined as:

$$\alpha_1 = \frac{x_2 - x_{\mathrm{exp}}}{x_2 - x_1} \tag{47}$$

Where x_2 and x_1 are the x coordinate of the two available computed points, and x_{exp} is the x coordinate of the experimental point. On the other hand:

$$\alpha_2 = \frac{x_{\mathrm{exp}} - x_1}{x_2 - x_1} \tag{48}$$

Once these two coefficients have been calculated and considering a generic fluid property ϕ, the interpolated value of this generic fluid property (ϕ_{interp}) is given by:

$$\phi_{\mathrm{interp}} = \alpha_1\ \phi_1 + \alpha_2\ \phi_2 \tag{49}$$

Where ϕ_1 and ϕ_2 are the computed values of ϕ at points 1 and 2 respectively. Hence, once this interpolated value is estimated, the local error could be obtained and consequently if the procedure is repeated iteratively, the defined error parameters could be calculated. In particular, e_1 and e_2 could be calculated if the generic fluid property ϕ is substituted with the pressure and the skin friction coefficient respectively. Finally, it should be outlined that an additional index k has been introduced on the algorithm to accelerate the calculation reducing the number of iterations within the implemented secondary loop.

Code 2: Octave routine used for the estimation of e_1 and e_2.

```
close all
clear all
clc

% Loading from exported Ansys data
p1=load('pressureplate.dat');
p2=load('pressureramp.dat');
tauwall1=load('tauwallplate.dat');
tauwall2=load('tauwallramp.dat');

% Freestream values
pinf=2.32e4; % Pa
uinf=562; % m/s
rhoinf=0.8223; % kg/m3

% Loading of experimental data
pexp=load('experimentalPressureDistribution.dat');
cfexp=load('experimentalcfDistribution.dat');
xpd=pexp(:,1);
pd=pexp(:,2);
xcf=cfexp(:,1);
cf=cfexp(:,2);

% Processing of imported computed data and axis system change
xpdcomputed=vertcat(p1(:,1)-1.2, (p2(:,1)-1.2)/cosd(20));
pdcomputed=vertcat(p1(:,2), p2(:,2))/pinf;
xcfcomputed=vertcat(tauwall1(:,1)-1.2, (tauwall2(:,1)-1.2)/cosd(20));
cfcomputed=vertcat(tauwall1(:,2), tauwall2(:,2))/(0.5*rhoinf*uinf^2);



% Interpolation and error calculation
e1=0;
e2=0;
% Auxiliary parameter introduced to accelerate the calculations
k=1;
for i=1:length(xpd)
  for j=k:length(xpdcomputed)
    if (xpdcomputed(j)>=xpd(i))
      % Introduction of weight functions and calculation of e1
      alfa2 = (xpd(i) - xpdcomputed(j-1)) / (xpdcomputed(j) - xpdcomputed(j-1));
      alfa1=(xpdcomputed(j)-xpd(i))/(xpdcomputed(j)-xpdcomputed(j-1));
      pinterp=alfa2*pdcomputed(j)+alfa1*pdcomputed(j-1);
      e1=e1+(pd(i)-pinterp)^2;
      k=j;
      break;
    endif
  endfor
endfor
```

```
% Auxiliary parameter introduced to accelerate the calculations
k=1;
for i=1:length(xcf)
  for j=k:length(xcfcomputed)
    if (xcfcomputed(j)>=xcf(i))
      % Introduction of weight functions and calculation of e2
      alfa2 = (xcf(i) - xcfcomputed(j-1)) / (xcfcomputed(j) - xcfcomputed(j-1));
      alfa1=(xcfcomputed(j)-xcf(i))/(xcfcomputed(j)-xcfcomputed(j-1));
      cfinterp=alfa2*cfcomputed(j)+alfa1*cfcomputed(j-1);
      e2=e2+(cf(i)-cfinterp)^2;
      k=j;
      break;
    endif
  endfor
endfor

% Square root of the accumulated errors and final results
e1=sqrt(e1)
e2=sqrt(e2)
```